Improving the mechanical, thermal and optical properties of biaxial and polyaxial Germanium suspended bridges towards a CMOS compatible light source

by

Daniel Burt

A thesis submitted in partial fulfillment for the
degree of Doctor of Philosophy

in the
Faculty of Engineering, Science and Mathematics
School of Electronics and Computer Science

May 2020

ABSTRACT

Doctor of Philosophy

by Daniel Burt

Germanium (Ge) is a promising candidate for a CMOS compatible laser diode. This is due to its compatibility with Silicon (Si) and its ability to be converted into a direct band gap material by applying tensile strain. In particular uniaxial suspended Ge bridges have been extensively explored due to their ability to introduce high tensile strain. There have been two recent demonstrations of low-temperature optically-pumped lasing in these bridges but no room temperature operation accredit to insufficient strain and poor thermal management. In this thesis the merits of using biaxial and polyaxial suspended Ge bridges to move towards room temperature operation were outlined. Uniaxial bridges were compared with polyaxial bridges in terms of mechanical stress and thermal management using Finite Element Modelling (FEM). The stress simulations revealed that polyaxial bridges suffer from extremely large corner stresses which prevent larger strain from being introduced compared with uniaxial bridges. Thermal simulations however reveal that they are much less thermally sensitive than uniaxial bridges which may indicate lower optical losses. Bridges were fabricated and micro-Raman (μ-Raman) spectroscopy was used to validate the results of the simulations. We postulate that polyaxial bridges could offer many advantages over their uniaxial counterparts as potential laser devices. Using a novel geometric approach and finite element modelling (FEM) structures with improved strain homogeneity were designed and fabricated. μ-Raman spectroscopy was used to determine central strain values. Micro-PhotoLuminescence (μ-PL) was used to study the effects of the strain profiles on light emission; we report a PL enhancement of up to 3x by optimizing curvature at a strain value of 0.5% biaxial strain. This geometric approach offers opportunity for enhancing the light emission in Ge towards developing a practical on chip light source. Finally the thesis concludes with a novel simple elliptical design for polyaxial bridges. This design further reduced the corner stresses in polyaxial bridges by 20%, even without optimization. A large 1.11% strain was achieved in a Ge on Si stack as confirmed by μ-Raman and FEM. Furthermore an optical cavity was introduced in this deign with no extra complex fabrication, this was confirmed using μ-PL and Finite Difference Time Domain (FDTD) simulations.

Contents

List of Figures

Acknowledgements

To . . .

Declaration of Authorship

I, Daniel Burt, declare that the thesis entitled: Improving the mechanical, thermal andoptical properties of biaxial andpolyaxial Germanium suspended bridges towards a CMOS compatible light source' and the work presented in the thesis are both my own, and have been generated by me as the result of my own original research.

I confirm that:

1. This work was done wholly or mainly while in candidature for a research degree at this University;

2. Where any part of this thesis has previously been submitted for a degree or any other qualification at this University or any other institution, this has been clearly stated;

3. Where I have consulted the published work of others, this is always clearly attributed;

4. Where I have quoted from the work of others, the source is always given. With the exception of such quotations, this thesis is entirely my own work;

5. I have acknowledged all main sources of help;

6. Where the thesis is based on work done by myself jointly with others, I have made clear exactly what was done by others and what I have contributed myself;

7. Parts of this work have been published as [1] [2]

Signed ....

Date ....

Chapter 1

Introduction

This chapter outlines the motivation behind the thesis, which begins by highlighting a major problem in modern micro / nano electronics: the interconnect bottleneck. An overview on Silicon (Si) photonics will be provided, which offers an elegant solution to the interconnect bottleneck. The main obstacle that is preventing Si photonics solving the interconnect bottleneck will be defined: the need for a Si compatible light source. Ge (Ge) light sources and why they are one of the best candidates for a Si compatible light source are then discussed. An overview on the various techniques and methodologies utilized to achieve Ge light sources are outlined. A wide variety of novel potential applications will then be presented. The chapter will conclude with the structure of this thesis.

1.1 The interconnect bottleneck

With the advent of the semiconductor and the invention of the transistor the human species experienced an extreme technological revolution: the heralding of the digital age. The particle responsible for this revolution was the electron, the material responsible was Si and the component responsible was the transistor [3]. The transistor allowed the development of Integrated Circuits (ICs), Computer Processing Units (CPUs) and subsequently the personal computer. To improve the computing power of these devices the semiconductor industry has mainly employed a simple yet effective tactic: increase the transistor density by reducing transistor size. Gordon Moore one of the co-founders of Fairchild semiconductors (now famously known as Intel) outlined a pseudo empircal law that predicted the number of transistors in a CPU will double and the cost of the CPU will half every year and a half [4]. Historically, increasing the transistor density by reducing transistor size is referred to as the 'More Moore' approach to improving CPU performance. However, the end of Moore's law is inevitable as transistors

reach a fundamental size limit, the recent Intel architecture possess 14 nm Metal-Oxide-Semiconductor Field Effect Transistors (MOSFETS) [5]. Scaling the gate and the active region has become an extreme engineering challenge. There are even demonstrations of transistors with feature sizes down to 7 nm[6], however we are rapidly approaching a hard limit due to current leakage, heating and geometric considerations.

New approaches are also being extensively explored and are referred to as the 'More than Moore' approach which also promises extra functionality on-chip. Examples of this extra functionality include: Radio Frequency (RF) devices, power/high voltage devices, passive components, sensors and actuators, bio-chips/bio-systems, micro-fluidics and solid-state lighting[7].

Introduction of Ge in the form of SiGe alloys or its pure elemental form could offer improved transistor performance. Ge was the original transistor [3] and possesses a higher electron mobility allowing faster transistor operation. Si prevailed over Ge as the choice of the Complementary Metal-Oxide Semiconductor (CMOS) industry, the two main reasons Ge was not used was a lack of stable native oxide (for the formation of gates) and also the cost of the devices as Si is one of the most abundant materials on the planet which can be sourced from Silicon Dioxide (SiO_2). However, as the limit of Moore's law are approached Ge and its alloy with Si become attractive, there is a large research focus into finding good passivation materials for Ge and in developing transistors from SiGe. SiGe transistors possess higher electron and hole mobilites than Si allowing faster operation with the same geometric footprint.

One key approach is to not focus on the transistors themselves but by replacing the metallic interconnects, of which performance wise have not scaled with the improved transistor density, this is often referred to as the interconnect bottleneck. To overcome this bottleneck one approach is to integrate novel materials such as Carbon Nano Tubes (CNTs) to replace the metallic interconnects [8]. However the most promising approach is to develop the convergence of photonics and electronics to produce optical interconnects. Photons unlike electrons and holes posses negligible mass and no charge, this drastically reduces signal loss, delay and heating effects assuming strict device requirements can be achieved [9].

1.2   Silicon photonics

Photonics can be defined as the science and engineering of photons (the particle responsible for light), usually involving the generation, manipulation and detection of photons [10]. Two key developments revolutionized and sculpted modern photonics: the development of semiconductor lasers in the 1960s [11] and the development of optical fibre technology [12], which underpins the technology behind the modern internet. The first

solid state semiconductor lasers were developed in the 1960s from III-V compound semi-conductors (such as GaAs) which possess a direct band-gap which allowing for efficient light generation. Due to their great success in photonics, researchers are keen to explore heterogeneous integration of III-V materials with Si to enable active on-chip optical interconnects [13] (which is highly desirable as discussed later in this section) . However heterogeneous integration faces many challenges including cost, material incompatibility and contamination of current CMOS foundries. Considering these vast challenges, there is a great motivation to explore photonic components made from Si or Si compatible (CMOS compatible) materials.
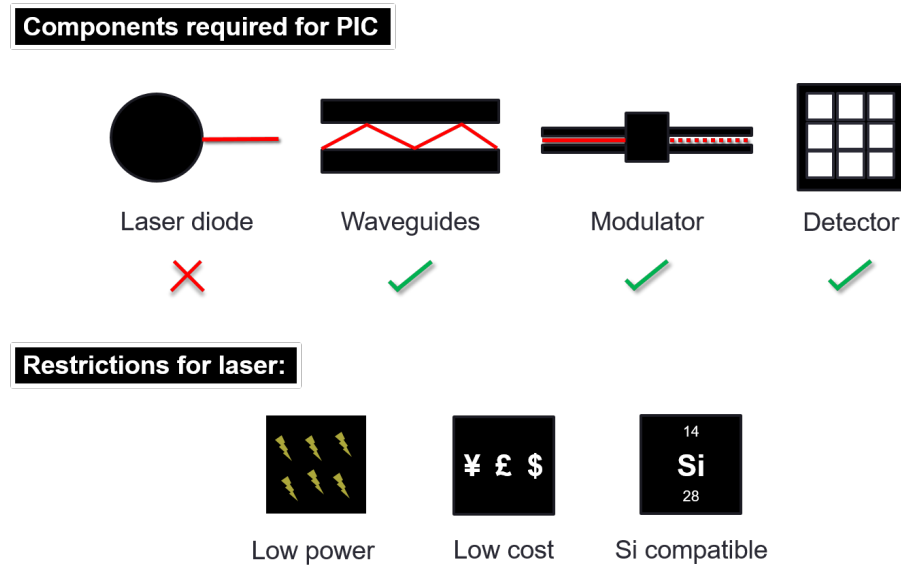
FIGURE 1.1: A schematic showing the main components required for a complete active Si photonics platform to enable PICs indicating that a laser diode is missing. Further restrictions for the laser diode are shown.

Si photonics is the study and application of photonic systems which utilize Si or Si compatible materials as the active medium [14]. As Si is the dominant material of ICs and CMOS technology it would be cheaper and more practical to develop optical interconnects in a CMOS compatible platform, which in turn would allow the full convergence of photonics and electronics. Si photonics usually operates at a wavelength of 1.55 μm, however wavelengths covering the visible, near infrared (NIR) and mid infrared (MIR) are increasingly more common thus expanding potential functionality [15].

Waveguides, modulators and detectors have been extensively developed [16]. Intel showcased a proof of concept integrated Si photonics platform featuring an optically pumped Raman laser, modulators, wave-guides and detectors [17]. Intel and Rockley photonics have already had commercial success developing passive optical interconnects for Local Area Networks (LANs) and Wide Area Networks (WANs) [18] [19]. However as Si is an indirect band-gap material, light emission occurs mainly through inefficient phonon mediated transitions[20]. Therefore Si is not suitable to make an on-chip light source which has resulted in intra and inter chip active interconnects being elusive.

A CMOS compatible on-chip light source has been referred to as the 'Holy Grail' of Si photonics [21]. With this light source, Si based active Photonic Integrated Circuits (PICs) can be developed. Figure 1.1 shows the main components required for an active Si photonics platform, with the laser diode missing and the further restrictions required for the laser diode. There has been attempts (with demonstrations of optical gain) to make Si a better light emitter for example by employing quantum structures [22, 23, 24]. However, for a practical on-chip light source electrical pumping becomes difficult with quantum structures [25]. Despite this quantum confinement in Si may offer a potential route to overcome the indirect band-gap nature of Si, there have been theoretical predictions of gain [22] and demonstrations of electrically pumped stimulated emission in Si Quantum Wells (QWs) using lateral carrier injection[23, 24]. Thus the search is on to find a CMOS compatible light source and this is the focus of this thesis.

1.3 Ge light sources

Ge is a promising material for a CMOS compatible light source despite also being an indirect band-gap material [20]. This is due to the fact the energy difference between the direct and indirect valley in Ge is relatively small (roughly 140 meV). Tensile strain engineering can be utilised to convert Ge into a direct band-gap material. Furthermore n-type doping allows the indirect L-valley to be occupied, resulting in injected carriers populating the direct Γ-valley and undergoing radiative recombination[26, 27].

MIT demonstrated a proof of concept laser [28] combining 0.24% biaxial tensile strain and 4 x 10^{19} cm^{-3} n-type doping exhibiting an injection current of 35 kW cm^{-2}. An electrically pumped laser was then demonstrated by the same group [29] with 0.25% biaxial strain and 4 x 10^{19} cm^{-3} n-type doping with a an injection current of 280 kA cm^{-2}. Despite this amazing achievement the injection currents were way too high for any practical device, thus the focus of the research was to achieve a practical devices.

Ge light sources have great potential to unlock a Si compatible light source, in the next chapter a comprehensive analysis of Ge light sources will be conducted. The goal of this thesis is to explore novel structures to move towards the practical implementation of Ge light sources.

1.4 Applications

We end this chapter with a brief discussion on the potential applications of a Si compatible light source [30, 31]. The main motivation discussed was the interconnect bottleneck which offers performance improvements for data centres, cloud computing, Fibre To The Home (FTTH) as well an intra and inter chip interconnects[23, 24]. However there are

a host of other other exciting and potentially disruptive technologies. The Internet of Things (IoTs) will require a massive transfer of data which can be achieved by optical interconnects. The red-shifting of the emission from 1.55 μm into the MIR is still acceptable for interconnects as the detectors also red-shift and could open up applications in chemical and bio-sensing on chip and be integrated with micro-fluidics technology for lab on a chip applications. Recently driver-less cars have been a hot topic, the technology of choice to enable this has been Light Detection and Ranging (LIDAR) technology. However current LIDAR units rely on III-V lasers, which are not only far too expensive for the mass market but also offer poor spatial resolution. Ge laser diodes could offer drastic price reductions, furthermore hundreds of lasers and detectors could be integrated with a high density on chip potentially offering much higher resolution. Ge light sources could also be utilised in cables such as High-Definition Multimedia Interface (HDMI)[23, 24] or Universal Serial Bus (USB), this could manifest as an array of detectors and lasers to offer more efficient data transfer. Quantum computing offers huge advantages over conventional computing not only in raw computational power, but also in novel computational abilities. As many of the technologies being developed for quantum computing are being built utilizing photonics, with an Si compatible light source it may be possible to miniturize these devices and place them on-chip for mass market applications. This section has demonstrated the vast potential for a Ge light source, it is not unreasonable to say that if an efficient CMOS compatible light source could be developed, it would be a truly disruptive technology. However strict requirements in terms of power and cost are required to truly yield the promised applications.

1.5   Project goals

Most of the research since the proof of concept studies, has been focused on improving the optical gain of Ge by employing strain engineering and/or n-type doping. Furthermore integrating the high strain into an optical cavity must also be developed. Recent demonstrations of low temperature lasing were accredited to improved thermal management or higher strain. Two of the recent demonstrations of lasing used uniaxial Ge suspended bridges[32, 33]. Biaxial / polyaxial suspended Ge bridges have not been explored as extensively as their uniaxial counterparts due to large corner stresses which limit the amount of tensile biaxial strain achievable[34]. However the author of this thesis postulated that due to more lateral thermal conduction paths, the thermal management in biaxial and polyaxial bridges is superior to their uniaxial counterparts. Furthermore recent theoretical and experimental studies have shown that around 3 times less biaxial strain is required to convert Ge into a direct band-gap material, this is attractive due to the technical challenges of achieving high strain.

With this in mind, the goals of this project were as follows:

1. Explore in detail the mechanical stress and thermal management in polyaxial and uniaxial suspended Ge bridges to identify any opportunities for improved devices.

2. Study the role of curvature on the strain profile in biaxial suspended Ge bridges. the corner stresses on the optical emission of biaxial bridges.

3. Develop novel designs for polyaxial and biaxial suspended Ge bridges to improve the thermal, mechanical and optical properties of the bridges.

Chapter 2

Background and Literature review

2.1 Introduction

This chapter begins with an introduction to the concept of the Germanium (Ge) laser and a description of the original proof of concept studies. The theory of Ge lasers is briefly discussed with analysis on tactics for moving towards more efficient and ultimately room temperature lasing. A comprehensive summary on the various material choices is then provided with their various advantages and disadvantages discussed. A critical analysis of the various high tensile strain platforms is conducted, comparing and contrasting various methodologies. Recent demonstrations of lasing are also reported and discussed providing an insight into future tactics for increasing the efficiency of Ge lasers. Finally a summary and and outlook is provided, setting the tone for the following results chapters.

2.2 Ge light sources

2.2.1 Concept and proof

As stated in the introduction, two popular routes to converting Ge into a direct band-gap material are tensile strain engineering and n-type doping. Figure 2.1 shows the influence of n-type doping and tensile strain on the band-structure of Ge. Utilising strain to engineer semiconductor band-structures was first proposed by Van De Walle *et al* [35].

Ge and Silicon (Si) have a a lattice mismatch of 4.2% this results in a large amount of defects at the interface [36] and results in degraded optical and mechanical properties

(e.g. non-radiative recombination). Furthermore if the lattice mismatch is only considered, Ge should posses a compressive strain which would increase the size of the indirect band-gap reducing light emission. However it was shown by Ishikwa *et al* [37] that when Ge was grown on Si epitaxially, a tensile strain was actually introduced into the layer. The reason for this is due to Ge having a larger Thermal Expansion Coefficient (TEC) than Si, therefore during the thermal annealing and subsequent cooling the decrease in lattice constant is suppressed by the thicker Si substrate resulting in a tensile strain within the Ge layer. The value of this strain was found to vary between 0.15% and 0.25%. It was also noted that the Light Hole (LH) and Heavy Hole (HH) valence sub-bands split under this tensile strain. This discovery sparked the interest in developing a Ge laser utilising tensile strain engineering.

The use of tensile strain to shrink the direct band-gap was initially explored for Ge photodetector applications, to extend the absorption edge [37]. Utilising Ge on Si as a lasing material was first proposed by Liu *et al* combining the small tensile strain in Ge with high n-type doping (to fill the indirect L-valley and force injected carriers into the direct valley) [26]. It was suggested that a combination of 0.25% biaxial tensile strain and around 7 x 10^{19} cm^{-3} n-type doping would be sufficient to provide a net gain of 400 cm^{-1}.

This was followed by demonstrations of enhanced micro-Photo-Luminescence (μ-PL) [38] and Electro-Luminescence (EL) [39] culminating in a demonstration of optical gain [27]. A proof of concept optically pumped laser was demonstrated by Liu *et al* [28] with 0.24% biaxial strain and 4 x 10^{19} cm^{-3} n-type doping, with a threshold injection power of 35 kW cm^{-2}. This was shortly followed by a demonstration of an electrically pumped laser [29] with 0.25% biaxial strain and 4 x 10^{19} cm^{-3} n-type doping with a threshold injection current of 280 kA cm^{-2}
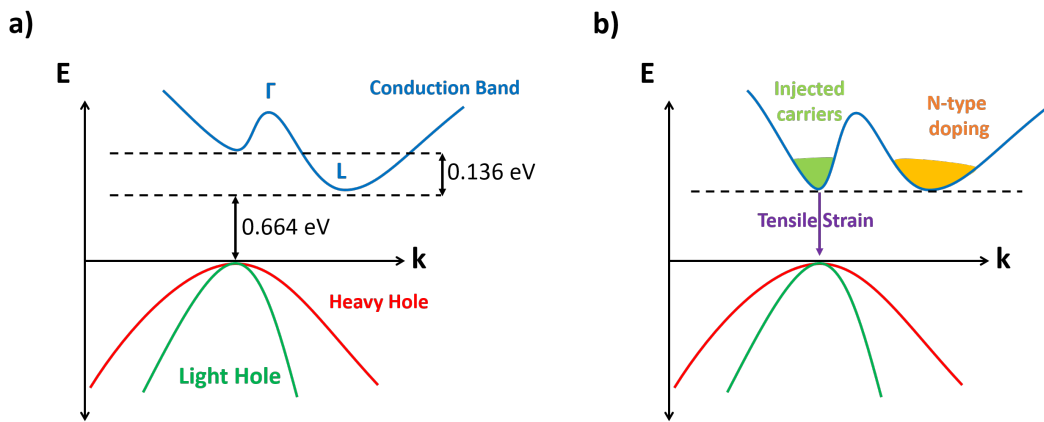
FIGURE 2.1: A schematic comparison showing the a) intrinsic Ge band-structure and b) the influence of tensile strain and n-type doping on the Ge band-structure.

These achievements were remarkable however the threshold current was phenomenally high and nowhere near the realms of a practical device (in the order of A cm^{-3}) [40],

from this however an entire research area dedicated to achieving an efficient Ge light source was born. The initial focus of the community was simple: combine n-type doping, tensile strain and an optical cavity to enable an efficient initially optically pumped but electrically pumped laser. Another group validated the initial lasing results with a demonstration of a Ge laser diode in 2015 using 0.25% biaxial tensile strain and 4 x 10^{19} cm^{-3}, under pulsed operation the threshold current density was 500 kA cm^{-2} [41].

2.2.2 Theory

With the basic principles of n-type doping and tensile strain engineering outlined and the proof of concept studies conducted, guidelines for whether researchers should focus on n-type doping or strain engineering and too what degree needed to be established. Towards this goal theoretical models were extensively developed which will be discussed in this section.

Band structure calculations are vital to understand the behaviour of Ge under tensile strain and high n-type doping. Many methods have been utilized including k ● p [42], tight binding, Density Functional Theory (DFT) [43] and Deformation Potential Theory (DPT)[37, 42]. Studies suggest that the optimum crystallographic direction to apply the strain for converting Ge into a direct band-gap material is along the ⟨100⟩ direction. Tensile strain reduces both the direct and indirect band-gaps however the direct band-gap energy is reduced faster and at a certain threshold value a cross over occurs and Ge becomes a direct band-gap. This value was initially though to be around 1.7% - 1.9% for biaxial and 4.4% - 4.6% uniaxial according to k ● p calculations and DPT [42] when the strain is applied along the ⟨100⟩ crystallographic orientation. From a theoretical standpoint, biaxial strain converts Ge to a direct band-gap material faster. Tensile strain also causes splitting of the LH and HH valence bands as demonstrated experimentally by Ishikawa *et al* [37].

Increasing the strain or n-type doping indefinitely does not guarantee improved lasing characteristics. Sukhdeo *et al* explored the ultimate limits of biaixial strain and n-type doping [44] using theoretical calculations. According to their calculations the minimum threshold current is achieved at 3.7% biaxial strain and 1 x 10^{18} cm^{-3} and for the lowest slope efficiency 2.3% strain and 1 x 10^{19} cm^{-3} n-type doping [44]. It was suggested that increasing the strain or n-type doping past these limits would degrade the threshold and slope efficiency respectively due to increased optical losses. Furthermore compared to the low strain and high n-type doping approach in the original proof of concept studies, they postulate he threshold current can be reduced by up to 4 orders of magnitude, by **adopting a high tensile strain and relatively low n-type doping approach**.

Gupta *et al* [45] argued that the main loss mechanism in Ge laser devices, Inter Valence Band Absoprtion (IVBA), was not modelled sufficiently in previous studies as no strain

dependence was considered. By modelling the IVBA more accurately, it was suggested that there was a certain resonance between the loss and gain mechanisms between 4-5% uniaxial strain where lasing is most efficient [45].

Guilloy *et al* [46] deduced experimentally that under high tensile stress, there is a nonlinear dependence of the direct band-gap and strain. This study showed that DPT, which is commonly used to study the influence of strain on the Ge band structure, underestimates the value of the band-gaps at higher strain values. Escalante [47] conducted a vigorous computational study to provide further details on this discovery, calculations suggested the indirect to direct cross over point for Ge was around 6% uniaxial strain and 2% biaxial tensile strain. This non-linear relationship means that around 3x less biaxial strain is required to convert Ge into a direct band-gap material compared to uniaxial strain. The non-linear dependency means that many previous studies underestimated the cross over point to direct band-gap.

There is still a lot of work to be conducted for studying the band structure and lasing dynamics under high tensile strain and n-type doping. Further theoretical work supported by vigorous experimental evidence at higher strain is required. From this section we can outline two key approaches for Ge lasers: 1) high n-type doping with moderate tensile strain and 2) high tensile strain with low n-type doping. This thesis will be focused on the later as it theoretically offers the greatest reduction in threshold current.

2.3   Sn-alloying

Alloying Ge with the element Tin (Sn) has a similar effect to tensile strain engineering (although there is no valence band splitting), and therefore is another promising approach towards a CMOS compatible laser. In relaxed GeSn systems, the material becomes a direct band-gap at around 6-8% Sn-content [48]. Proof of concept GeSn lasing was demonstrated by Wirths *et al* [48], under pulsed optical operation at 90 K, however, the threshold power density (1000 kW cm^{-2}) was extremely high, and beyond the realms of practical usage.

The tactic adopted to reduce the threshold and increase the operating temperature by increasing the Sn-content of the active gain medium. At higher Sn-contents, more electrons occupy the direct Γ valley where they can contribute to optical gain. Furthermore, larger increases in the energy offset between the Γ and L valley prevent electrons from scattering into the L valley, where they can only contribute to optical loss mechanisms.

Despite many successful lasing demonstrations with increasing Sn-content GeSn [48, 49, 50, 51, 52], the reported thresholds have been extremely high (above 100 kW cm^{-2}) and only under continuous-wave operation, and therefore beyond any practical use.

The reason for these drawbacks is that as the Sn-content has increased, the lattice mismatch between the Ge buffer layer and the GeSn layer increases, which causes an increased number of dislocations and, therefore, non-radiative recombination. Higher optical pump powers are required to overcome the non-radiative losses, which in turn results in a higher threshold being required. Furthermore, during continuous-wave operation, self-heating effects are more severe when compared to pulsed operation as the system cannot thermally relax between pulses; therefore, all reported lasing was quenched under continuous-wave operation.

Recently, a hybrid approach combining moderate tensile strain with low Sn-content alloying was suggested to overcome these issues [53]. By using a lower Sn-content GeSn alloy, a lower dislocation density is achieved, which reduces the non-radiative recombination substantially. Applying tensile strain allows for a similar band-structure as the higher Sn-content alloys. The first demonstration of continuous-wave lasing was demonstrated using this hybrid approach in tensile strained GeSn microdisks [54]. This microdisk also exhibited remarkable threshold reductions of 2 orders of magnitude with a record low threshold power density of 0.8 kW cm^{-2}.

Sn-alloying is mostly out of the scope of this thesis; however the results presented in the following chapter have exciting implications for the hybrid approach (low Sn-content with tensile strain) and will be discussed in the final chapter.

2.4 Material considerations

With the theoretical principles of band-gap engineering Ge via tensile strain outlined in the previous section, the practical implementation of a Ge laser device will now be discussed. This sub section will compare and contrast the various material forms of Ge and their suitability for practical devices. As the ultimate motivation of this research is to develop mass production of Si compatible lasers, CMOS compatibility will be assessed. Material quality is of extreme importance for the successful operation of any potential Ge light emitting device. Poor material quality in the form of defects can degrade the mechanical, optical, electronic and thermal properties of Ge reducing the threshold current, or even inhibiting lasing action in Ge [55].

The previous section highlighted how a large amount of tensile strain is required to convert Ge into a direct band-gap material. Material defects in the Ge degrade the fracture toughness[55], this in turn inhibits high elastic tensile strain and therefore a direct band-gap material configuration. Furthermore defects in the Ge lattice act as non-radiative recombination sites decreasing the excess carrier lifetime, thus limiting the internal quantum efficiency[56, 30, 31]. This is observed experimentally by degradation of the direct band-gap luminescence.

Bulk Ge wafers provide high crystal quality with Etch Pit Densities (EPD)[55] (a method used to characterize the density of dislocations) in the range of 10^2 to 10^3. However Ge wafers are not useful for practical devices due to difficulty in confining an optical mode owing to a lack of refractive index contrast. Furthermore they are substantially more expensive than Si wafers inhibiting low cost applications (however are still cheaper than III-V compound semiconductors). Ge also has a lower thermal conductivity than Si resulting in more strict thermal management being required to prevent degradation of device performance due to heating[57].

To overcome these issues, most of the focus of practically implementing Ge photonic devices is to grow thin layers of Ge epitaxially onto Si. Firstly, Si wafers are extremely cheap and abundant, as only a small amount of Ge is required so the cost is kept low. Secondly Si has a lower refractive index then Ge allowing optical modes to be confined in Ge. Finally as Si has a large thermal conductivity, thermal management in any devices will be excellent. The potential laser device is also integrated with Si allowing for the convergence of CMOS photonics and electronics, the original motivation behind the research.

However due to the large lattice mismatch of 4.2% between Ge and Si, many defects are introduced growth preventing thick high quality Ge layers being grown. The most common defects are threading or misfit dislocations, the misfit dislocations tend to be highly concentrated at the Ge/Si interface [36]. Substantial effort has been directed in to improving the quality of the Ge on Si. Many epitaxial growth techniques have been explored including Low Energy Plasma Enhanced Chemical Vapor Deposition (LEP-ECVD) [58] and Ultra High Vacuum Chemical Vapour Deposition (UHVCVD) [59]. A two step process is usually employed to improve the quality and thickness uniformity of the Ge layer. First a Low Temperature (LT) buffer layer is deposited ($400°$C) resulting in a film with poor quality [30][31]. Next a High Temperature (HT) layer is deposited ($700°$C) with an active layer possessing higher crystal quality[30, 31, 26, 29, 27]. Even with the two step deposition, the defect density is still large in Ge on Si ranging between 10^6 - 10^8 with a large amount of misfit dislocations concentrated at the Ge/Si interface significantly degrading the carrier lifetime[36].

Virtual substrates use a series of graded SiGe alloy buffer layers with increasing Ge content, however they result in poor thickness uniformity across the wafer and still result in a relatively large amount of dislocations [30].

Ge on Si on Insulator (Ge on SOI) has also been explored. Ge can be epitaxially grown onto commercially available SOI wafers. However if the Ge is still epitaxially grown onto the SOI, the defect density is still large and comparable to Ge on Si. To improve the material quality wafer bonding can be employed. A Germanium On Insulator (GOI) stack can also be created by bonding Ge directly to SiO_2 thermally grown onto Si [56, 60]. For GOI fabrication a Ge on Si donor wafer is bonded to an oxidised Si layer, this is

followed by back grinding to remove the donor Si layer followed by a Chemical Mechanical Planarisation (CMP) step to remove the high concentration of misfit dislocations where the Ge/Si previously was located. Both the Ge on SOI and GOI stacks possess a Buried Oxide (BOX) layer which provides excellent confinement of the optical mode in Ge due to a much larger refractive index contrast compared with Ge on Si stacks. However the thermal conductivity of the BOX layer is extremely low (two orders of magnitude lower than Si) which can result in severe heating of devices, this will be discussed in more detail later on. Some of the most common Ge material forms used for Ge light sources are shown and compared in Figure 2.1.

	Bulk Ge	Ge on Si	Ge on SOI	GOI
Cross section	Bulk Ge	Ge / Si	Ge / Si / SiO$_2$ / Si	Ge / SiO$_2$ / Si
Refractive index contrast	None	Moderate	Excellent	Excellent
Cost	$$	$	$$$	$$$$
Thermal management	Good	Good	Poor	Poor
EPD (cm^{-2})	10^1-10^3	10^5-10^7	10^5-10^7	10^5-10^7

FIGURE 2.2: A schematic comparison showing the common material forms used for Ge light sources.

Ge has also been grown on Si on quartz, this enhanced the amount of intrinsic tensile strain in Ge to up to 0.36% which is nearly double the value when grown on a bulk Si wafer. However, as the material is grown on Si the dislocation density should be high and the thermal conductivity of quartz is relatively low compared to Si making practical device integration difficult [61].

2.5 Tensile strain engineering

This sub-section is focused on the practical techniques employed to achieve high tensile strain in Ge. The focus is on methods that introduce a large amount of either uniaxial or biaxial tensile strain. Furthermore any attempt for integration of an optical cavity with the high tensile stain is also reviewed here. Two main approaches will be described: stressor layers and Micro Electro Mechanical Systems (MEMS) like structures.

2.5.1   Stressor layers

Stressor layers have been utilized in CMOS technology to enhance the mobility of both electrons and holes in transistors. Most commonly Silicon Nitride (Si_3N_4) is deposited directly and locally onto the transistor devices [62, 63]. SiGe alloy can also utilized as a stressor layer and has found success in CMOS manufacturing[64]. The concept of the stressor layer is to deposit a film with an intrinsic stress and utilize this stress to impart strain into the underlying Ge layer. Deposition parameters can be tuned to tune the nature of the stress, for example in PECVD Si_3N_4. Parameters such as the H_2 and N_2 percentages in the deposition gas or the Radio-Frequency (RF) to Low Frequency (LF) power ratio. This allows for both tensile or compressive stress to be introduced as well as the ability to tune the value of the stress.

The stress from the stressor layer is transferred onto the Ge utilizing one of two methods:

1. Local patterning of the stressor layer [65, 66, 67, 68, 69, 70]

2. Deposition of a stressed film on a 3D patterned structure. [71, 72, 73, 74, 75, 76, 77, 78, 79]

Both these methods have been extensively explored for enhancing the light emission in Ge and both methods tend to use an initially compressive Si_3N_4 stressor layer to impart tensile strain into Ge.

2.5.1.1   Local patterning of the stressor layer

Local patterning of the stressor layer involves a film with an intrinsic compressive stress being deposited over the Ge substrate followed by subsequent patterning. Upon patterning, the stressed film is free to relax at the patterned interface, thus expanding and imparting a tensile strain on the underlying Ge in the regions underneath the remaining stressor layers [65, 66, 67, 78, 68, 69]. This is the more common approach and earliest use of stressor layers to introduce strain into Ge. This has been used to apply strain into Ge wave guides [65, 68, 69, 78] and micro-cavities[66, 67, 70]. Preliminary studied showed around 1% biaxial strain was introduced, which is a decent amount but not enough to convert Ge into a direct band-gap material.

A big challenge facing these Si_3N_4 stressor layers is the laterally non-uniform strain distributions, which in turn results in lateral band-gap variations[65, 66]. For example in micro-disks with locally patterned stressor layers, the strain is maximum in the central region whereas the optical mode is located at the circumference, this means the strain and the optical mode do not overlap.

In addition to this, the Si_3N_4 stressor layers cause a strain non-uniformity across the transverse thickness of the Ge. The strain accumulates at the interface between the Ge and Si_3N_4[65, 66, 67]. This can increase losses, as carriers can be confined at the surface where non-radiative recombination acts as a loss mechanism. This can be partially mitigated by good surface passivization.

2.5.1.2 Deposition of stressed film on patterned structures

To overcome the strain non-uniformity issues the deposition of a stressed film on patterned structures was developed. If a patterned surface of a Ge structure is coated by an intrinsically compressively stressed film, a tensile strain is imparted into the Ge structure providing higher values of strain and improved strain homogeneity. The first attempts focused on coating the top and sides of Ge patterned structures, using both initially tensile and initially compressive Si_3N_4. Tani *et al* [71, 72] applied Si_3N_4 around a Ge waveguide structure, the top of the waveguide possessed a compressive strain where the sides possessed a small tensile strain.

Velha *et al.* [74, 75] showed tuneable stress in Ge nanopillars using Si_3N_4, the intrinsic stress could be altered from 3 GPa compressive to 2 GPa tensile resulting in a maximum tensile strain of 2.5%, enough to convert Ge into a direct band-gap material. Millar *et al* [76] reproduced these results with emission up to 2.25 μm, however no optical cavity was integrated and therefore no lasing could be demonstrated.

Millar *et al* [77] applied the all around stressor approach to Ge micro ring resonators, using 2.45 GPa compressively stressed Si_3N_4 resulting in 2% biaxial strain. This value of strain is theoretically supposed to make Ge a direct band-gap material, however despite whispering gallery modes being present, no lasing was reported.

Ghrib *et al* [78] used an all-around stressor layer approach to coat a Ge micro-disk with Si_3N_4. Initial work achieved strain values up to 1.45% with improved strain uniformity in both the transverse and lateral direction. Further publications from the same group [73] demonstrated increased strain values up to 1.75%, for which they claimed a direct band-gap material. However despite these amazing achievements lasing was still unattainable, strangely the lower strain values possessed higher Q factors.

Al-Attili *et al* [80] utilized PECVD SiO_2 as an all-around stressor layer in conjunction with the BOX layer in a Ge on SOI substrate, to impart tensile strain into Ge. Ge micro-disks with added gratings around the circumference (referred to as microgears) were fabricated. The goal of this study was to introduce enhanced Orbital Angular Momentum (OAM), opening up a path for CMOS compatible vertically emitting lasers and OAM lasers. However no lasing has been demonstrated on this platform yet as the tensile strain is relatively low, however the strain can easily be increased using Si_3N_4.

2.5.2   MEMS like structures

MEMS like structures were first proposed by Lim *et al* [81] to introduce moderate tensile strain values in Ge by utilizing a cantilever like structure. Nam *et al* demonstrated 1% biaxial strain combining tungsten stressors, with high intrinsic compressive stress using Si vias. Boztug *et al* [82] used an Ge nanomembrane on suspended platinum, they introduced the strain into the Ge by applying a high pressure gas causing bending of the nanomembrane. More recently it has been theoretically proposed by Ayan *et al* [83] that strain can be applied to Ge by electrostatic actuation with preliminary simulations, to develop this concept further an optical cavity must be integrated, strain inhomogeneities addressed and a practical device fabricated.

The majority of the research for MEMS like structures has focused on suspended bridge structures. Jain *et al* [84] used initially tensile Si_3N_4 pads on a GOI substrate with a patterned bridge, upon suspending the entire structure the Si_3N_4 pads relaxed imparting tensile strain into the central bridges. Both uniaxial and biaxial structures were fabricated achieving 0.96% uniaxial strain and 0.82% biaxial strain. As the strain is applied from the top, the strain is largerly inhomogenous through the transverse thickness of Ge, with the larger strain concentrated predominantly at the surface.

Al-Attili *et al* [85, 86] used a Ge on SOI substrate to pattern micro-disk resonators. Bridges were subsequently defined in the BOX layer underneath the Ge micro-disk, followed by suspension of the entire structure, by etching the underlying Si substrate. This resulted in both uniaxial and biaxial tensile strain within the Ge micro-disks depending on the bridge design.

The most popular and successful MEMS like structures for Ge light sources, and the structures which are the focus of this thesis, have involved suspending the Ge bridges directly. Originally this method was developed for Si nano-wire bridges [87] but has since found success for Ge light sources. The basic principle of this method relies on amplifying the small amount of biaxial tensile strain locked into the Ge layer, introduced during the epitaxial growth of Ge on Si. The first step is to pattern the Ge layer into a central smaller bridge region connected to larger pad regions. The second step is to selectively etch the sacrificial layer underneath the Ge layer thus suspending the bridges. As the bonds between the Ge and the sacrificial layer are broken, the Ge is now free to relax. As the pads relax they constrict, causing the smaller bridge region to be pulled by the larger pads and imparting a tensile strain into the bridge. Figure 2.2 presents a schematic illustrating the main steps of the strain amplification process in suspended Ge bridges.

The sacrificial layer depends on the substrate used: Si for Ge on Si and BOX for GOI/Ge on SOI. The size of the strain can simply be controlled lithographically by increasing / decreasing the size of the pads and the bridge. Furthermore by controlling the geometry
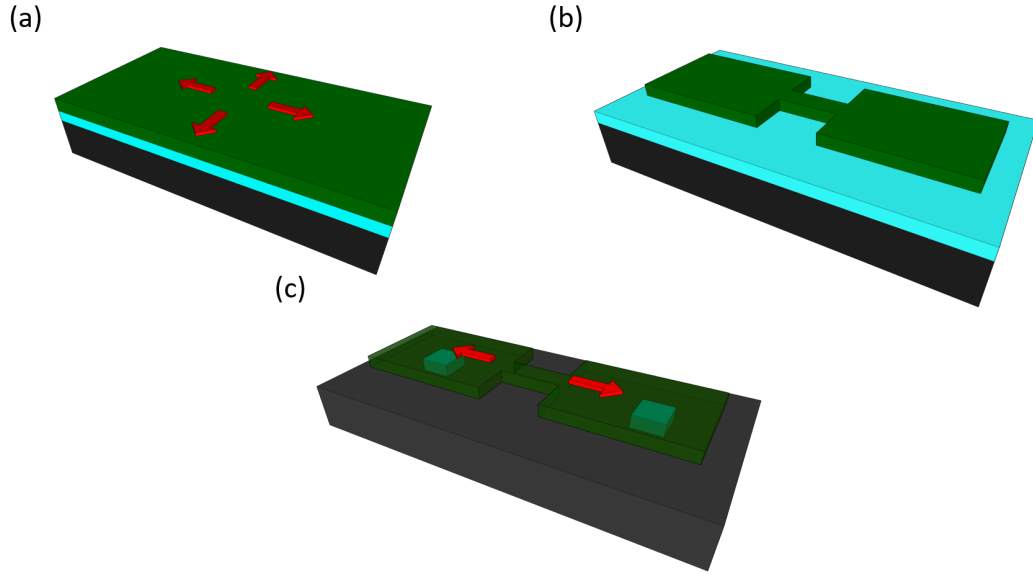
FIGURE 2.3: A schematic showing the basic concept of strain amplification in Ge suspended bridges, with a uniaxial bridge as an example in a GOI stack. a) The starting GOI stack with the layers shown, Ge in green, SiO_2 in cyan and Si in black. b) The patterning to form the bridge, usually achieved by dry etching. c) The suspension of the bridge and pads with the strain amplification in the bridge.

of the bridge and pads both uniaxial (using a uniaxial design) and biaxial strain (using a biaxial or polyaxial designs) can be introduced into the central bridge region.

2.5.2.1   Uniaxial suspended bridges

Süess *et al* [88] first demonstrated strain enhancement in Ge uniaxial suspended bridges, both Ge on Si and Ge on SOI substrates were studied. It was discovered that the Ge on SOI substrates possessed an enhanced strain relative to Ge on Si, this was due to the presence of the SOI layer which caused bending after removing the sacrificial BOX layer underneath. The maximum strain achieved in this study was 3.1% uniaxial strain measured using micro-Raman (μ-Raman) spectroscopy. Furthermore enhanced light emission was demonstrated from these uniaxial bridges using PL measurements.

By improving the design and using higher quality GOI wafers uniaxial strain values of up to 5.7% were demonstrated [89, 90, 60]. However this is actually not the highest value, as it was experimentally shown that the μ-Raman measurement of the strain, has a second order term at higher strain values [91, 92] therefore using a linear relationship overestimated the strain value for high strain ($>4\%$). Therefore the maximum strain value for uniaxial suspended bridges in reality was around 4.9%[89, 90, 60] not 5.7%. Despite the amazing engineering achievements of achieving such high strain, further tensile strain is required to convert Ge into a direct band-gap material and allow efficient steady-state room temperature lasing.

In conventional laser devices, double heterostructures are employed to reduce the threshold to practical levels. The double heterostructure is comprised of a material with a smaller band-gap sandwiched between a material with a larger band-gap. The carriers are confined in the smaller band-gap active region resulting in enhanced recombination. Nam *et al* [93] demonstrated heterojunction like effects in uniaxial suspended bridges referred to as 'Pseudo-heterostructures'. As the pads have a larger band-gap than the narrow active region, the carriers are confined in the narrow bridge. This allows hesterostructure like effects to occur in a single material by using strain gradients, confining carriers in the higher strain regions. Psuedo-heterostructures are advantageous over conventional heterostructures as they circumvent the need for complex epitaxy and can be controlled lithographically.

Attempts to integrate an optical cavity into uniaxial suspended Ge bridges were also carried out. Petykiewicz *et al* fabricated Distributed Bragg Reflectors (DBRs) in-between a suspended Ge nanowires[94]. The DBR mirrors were dry etched into the pads providing an optical cavity with Q factors of up to 2000 and uniaxial tensile strain values between 1.95% to 2.37%. Despite the combination of the Pseudo-heterostructure, a high Q optical cavity and moderate tensile strain the room temperature μ-PL measurements did not reveal lasing.

A Distributed Feedback (DFB) cavity was proposed with high simulated Q factors up to 17,000 [95]. However unfavourable corner stresses reduce the achievable amount of tensile strain within the bridge and a large sensitivity to fabrication variations made this optical cavity difficult to implement experimentally. A more simple parabolic shaped corner cube mirror was adopted at the cost of a lower Q factor, this was demonstrated to exhibit emission up to 5 μm, however no lasing was demonstrated. Jiang *et al* demonstrated room temperature electroluminesence from a suspended Ge bridge with 1.76% strain, despite no lasing this demonstrates the feasibility of electrical pumping in suspended bridges [96].

One major issue with suspended bridges as a method for introducing strain in Ge is thermal management. As the Ge is suspended in air, any heat generated during device operation or characterisation can only escape laterally. To partially mitigate this issue a novel Ge on Dual Insulator (GODI) substrate was proposed [97]. The GODI has an extra Al_2O_3 layer on top of the standard SiO_2 BOX. After the selective wet etching of the sacrificial Al_2O_3 layer with Potassium Hydroxide (KOH), capillary forces introduced during the drying step were utilised to bring the Ge layer in contact with the SiO_2 BOX. This provided a solid thermal conduction path to the underlying Si drastically improving thermal management whilst maintaining confinement for any potential optical modes due to the large refractive index contrast between Ge and SiO_2. However SiO_2 still has a fairly low thermal conductivity compared to Ge or Si, around 2-3 orders of magnitude, therefore heating is still quite severe in these bridges compared with conventional III-V laser diodes.

2.5.2.2 Biaxial / Polyaxial bridges

Soon after uniaxial suspended Ge bridges were demonstrated, interest was shown in biaxial and polyaxial bridges, both of which introduce biaxial strain into Ge. The motivation for these bridges is the fact that in theory, lower biaxial strain is required to convert Ge into a direct band-gap material. The first design was presented in the thesis of Martin Süess [98], a Maltese cross structure. FEM was used to study this structure and it showed that high corner stress was introduced which in turn reduces the amount of achievable biaxial strain.

Sukhdeo *et al* [34] demonstrated up to 1.11% biaxial strain in a central Ge disk in which the strain could be tuned lithographically. In contrast to the Maltese cross structure proposed by Süess *et al*[98], multiple etch slits were used to create a more homogeneous strain. However the achievable strain was still relatively low compared to uniaxial bridges from the same group, furthermore the enhancement in μ-PL was only 2.3 times compared to a predicted 20 times. Sukhdeo *et al* [99] further extended on this work by creating a micro-disk resonator from their structure. They deposited a compressively stressed Si_3N_4 layer to prevent strain relaxation, followed by etching their structure into micro-disk resonators. Low Q factors were reported likely due to strain relaxation at the circumference of the micro-disk where the first order WGM are located combined with the heating due to the lateral thermal paths being disconnected during the dry etching to form the micro-disk.

Gassenq *et al* [100] demonstrated a record high 1.9% biaxial strain, nearly enough to convert Ge into a direct band-gap configuration, using high quality GOI and a structure similar to the Maltese cross proposed by Süess *et al*. The high value of strain was attributed to the high quality GOI used opposed to any improved design. Ishida *et al* [101] demonstrated up to 0.8% biaxial strain in suspended Ge bridges from a Ge on SOI stack, the lower achieved strain was due to larger corner stresses.

2.6 Lasing from highly strained Ge

The previous two sections summarised the two main approaches used to increase the tensile strain in Ge to reduce the lasing threshold, towards efficient steady state room temperature operation. Despite excellent achievements of combining high strain with high Q optical cavities, lasing was not reproducible let alone more efficient. However more recently there have been three demonstrations of low temperature optically pumped pulsed operation lasing. Elbaz *et al* [102] demonstrated lasing using an Si_3N_4 all around stressor on micro-disks. Bao *et al* [32] and Pilon *et al* [33] demonstrated lasing in uniaxial suspended bridges. In this section an discussion of the lasing demonstrations are provided.

Bao *et al* [32] demonstrated lasing in a uniaxial suspended nano-wire bridge. The uniaxial strain value was 1.6% combined with 1×10^{19} cm^{-3} n-type doping. The optical cavity was created by DBR mirrors on each side of the pad resulting in multi-mode operation between 1500 nm and 1600 nm and experimental Q factors of up to 850. The threshold power density for lasing was 3.0 kW cm^{-2} under pulsed operation, with lasing occurring up to around 80K. The nano-wire bridge was adhered to the SiO$_2$ BOX layer underneath the Ge after suspension using the GODI platform, which has an order of magnitude larger thermal conductivity than air. This significantly improved the thermal management therefore allowing lasing by suppressing the largest loss mechanism: IVBA.

Elbaz *et al* [102] demonstrated lasing in all around Si$_3$N$_4$ stressed micro-disks. Unlike previous versions of this structure, in which the micro-disk was on an SiO$_2$ pedestal, this version had a metallic pedestal drastically improving the thermal management [79]. This was illustrated using FEM with a micro-disk under 8 mW continuous-wave optical pumping at 15K ambient temperature. The micro-disk with an SiO$_2$ pedestal rose 310K whereas the micro-disk with a metallic pedestal only rose 40K. The all around Si$_3$N$_4$ stressor resulted in tensile strain values up to 1.7% biaxial strain, with the higher strain concentrated at the circumference of the micro-disk where the WGMs are located. Weak mode competition was observed which was accredited to large in-homogeneous broadening due to the strain distribution within the disk. The authors claim a direct band-gap configuration at this value of biaxial strain, however according to theoretical studies the value is higher at 2%. Continuous-wave lasing was demonstrated with a threshold power density of 18 kW cm^{-2} at 15K. It was noted that no lasing was observed in micro-disks with smaller strain values. Lasing was again demonstrated up until 80K at around 2 μm emission, at higher temperatures the lasing was quenched, this was accredited due to a small offset between Γ and L valleys as well as heating, despite the improved thermal management.

Pilon *et al* [33] performed a detailed study on the lasing dynamics in highly strained uniaxial suspended bridges. Room temperature intrinsic Ge suspended uniaxial bridges with room temperature strain values of around 3% were cooled down to below 100K. When the bridges were cooled down the strain was enhanced due to the TEC mismatch, the largest studied strain was 5.9% uniaxial strain. The authors state that this is just below the transition from an indirect to direct band-gap material according to their tight binding calculations. Temperature and strain dependant studies revealed that again the lasing was quenched at around 80K. The authors postulated that the quenching was due to the blocking of phonon mediated scattering from Γ to L valley during pulsed operation at low temperatures. This only occurs at lower temperatures allowing for efficient lasing. They suggest moving towards higher temperature and/or steady state operation requires a larger band offset between Γ and L valley. According to tight binding calculations, 6.8% uniaxial strain will result in 20 meV offset resulting in a gain of 1000 cm^{-1}. The theoretical limit for strain along the $\langle 100 \rangle$ direction is 16% strain,

therefore it is a technical challenge to increase the strain by improving material quality and the fabrication process. To move to higher operation temperature, strain higher than 2% biaxial and 6% uniaxial are required. Furthermore good thermal management is crucial to prevent optical losses, in particular IVBA.

2.7   Summary and outlook

This chapter began by describing the proof of concept studies which demonstrated lasing using moderate tensile strain and high n-type doping, the need to drastically reduce the threshold power for operation was highlighted. The theoretical models and simulations were then discussed, it was revealed that this reduction could be best be achieved by a high tensile strain and low n-type doping approach to provide the best lasing efficiency. They also revealed that much less biaxial strain is required to convert Ge into an efficient lasing material. The various material platforms of Ge were then compared and contrasted in terms of CMOS compatibility, material quality and optical confinement. The two main methods for introducing high tensile strain into Ge were then vigorously discussed: stressor layers and MEMS like structures. Despite the successes of these platforms in combining high strain with an optical cavity lasing was not reproducible until recently in which low temperature pulsed operation lasing was demonstrated by multiple groups.

The next steps for Ge lasers is now to move to higher temperature operation with the ultimate goal of room temperature lasing. Optical lasing must first be demonstrated under steady state operation, after this the the ultimate goal of room temperature electrically pumped lasers can be targeted. The greatest success for high strain lasing has come from suspended Ge bridges [32, 33]. Both of these bridges introduced uniaxial strain into the Ge to allow low temperature pulsed lasing. However theoretical studies combined with preliminary experimental evidence, show that a much larger amount of strain is required to enable higher temperature / steady state operation than has currently been achieved (above 6% uniaxial). This is difficult to practically achieve with maximum room temperature value of 4.9% in extremely thin wires, these wires however are not very suited for practical devices as they suffer from extreme heating and poor optical mode confinement. The limit of increasing the strain is mainly due to the poor crystal quality (i.e. high number of dislocations) in the Ge which cause mechanical fracture at high strain. Furthermore these structures suffer from poor thermal management due to the bridge being in contact with low thermal conductivity materials such as air or glass. In addition to this the uniaxial bridges are extremely narrow and asymmetric likely restricting efficient lateral heat dissipation. This in turn increases the losses (in particular IVBA and FCA) inhibiting higher temperature operation.

Biaxial / Polyaxial bridges that introduce biaxial strain have not been studied as extensively as uniaxial bridges and have been somewhat overlooked. The reason for this is two fold: large corner stresses preventing high strain and also difficulty integrating an optical cavity. However the argument of this thesis is that biaxial / polyaxial bridges can offer advantages in terms of strain engineering and thermal management. As highlighted many times in this chapter, a much lower (around 3 times) amount of biaxial strain is required to convert Ge into a direct band-gap material compared to uniaxial strain. This is much larger than first thought, therefore there is opportunity to increase the biaxial strain by improved design opposed to material limitations in uniaxial. Furthermore the thesis conjects that biaxial / polyaxial bridges offer advantages in terms of thermal management due to greater lateral thermal conduction paths. The thermal and mechanical properties of uniaxial and biaxial bridges are studied extensively. With this in mind this thesis has two primary goals:

1. Study and compare the mechanical stress and thermal management in uniaxial and biaxial/polyaxial bridges to reveal how to improve these features towards higher temperature lasing

2. Offer improved biaxial/polyaxial designs to enhance strain homogeneity, reduce corner stress, improve thermal management and if possible integrate an optical cavity.

Chapter 3

A comparison of uniaxial and polyaxial suspended germanium bridges in terms of mechanical stress and thermal management

3.1 Introduction

In this chapter, we study and compare uniaxial and polyaxial suspended Germanium (Ge) bridges along with their respective geometric parameters in terms of mechanical stress and thermal management to understand which configurations could potentially be better for lasing. Finite Element Modelling (FEM) was used to study the influence of various design parameters on the thermal management and mechanical stress. Uniaxial and polyaxial bridges were successfully fabricated on a Ge on Silicon-on-Insulator (SOI) platform to provide experimental verification of the simulation data. This is done in the form of device survival analysis and Raman spectroscopy. The advantages and disadvantages of using uniaxial or polyaxial bridges will be then discussed in detail.

Published in [2]

3.2 Bridge designs

Figure 3.1 provides a top view of the uniaxial design used in this study. The blue regions show the Ge whereas the black regions show the patterned etching windows. In the etching windows, material is removed by dry etching to expose the sacrificial layer underneath. This is followed by an etchant entering these windows and selectively

etching the sacrificial layer under etching the Ge resulting in suspension. The maximum distance for the etchant to undercut the Ge was fixed at 10.0 μm in this study as shown in Figure 3.1. The basic principle of tensile strain engineering in suspended bridges relies on reorganizing the initial tensile biaxial strain of 0.2% introduced during the epitaxial growth of Ge on Silicon (Si) (caused by a mismatch in the Thermal Expansion Coefficients (TECs))[37]. The larger regions (the pads) compress resulting in the smaller active region being pulled. The geometry of the etching windows is extremely important as it determines the nature (uniaxial/biaxial), magnitude and the distribution of the tensile strain within the bridge.
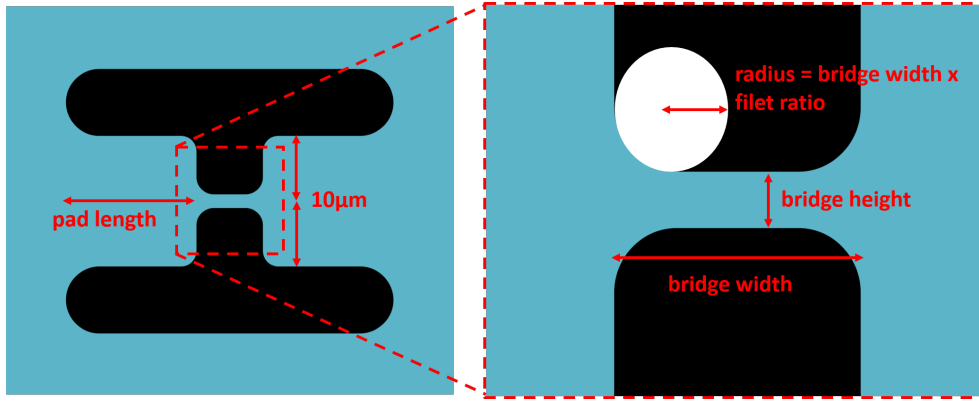
FIGURE 3.1: Exemplar uniaxial design showing the pad length. The central region is shown under zoom and the parameters bridge height, bridge width and filet ratio are defined. The fixed under etch distance of 10.0 μm is also shown.

The design for the uniaxial bridges used in this study is shown in Figure 3.1. There are four important parameters which are: bridge height, bridge width, filet ratio and pad length. The values of bridge height used in this study were 0.75 μm, 1.5 μm, 2.25 μm and 3.0 μm. The values of bridge width used in this study were 2.5 μm, 5.0 μm, 7.5 μm and 10.0 μm. Filet ratio is a ratio which defines the radius at the edges of the bridge by multiplying this ratio by bridge width, the value was fixed in this study to be 0.25. The pad length used in this study was 30.0 μm.

The design for the polyaxial bridges used in this study is shown in Figure 3.2. Etch window thickness defines the size of the etch windows and is fixed at 0.3 μm in this study. There are three important parameters which are varied: bridge diameter, the number of arms and the pad length. The values of bridge diameter chosen for this study were 3.0 μm, 4.0 μm, 5.0 μm and 6.0 μm. In this study the number of arms studied was 4, 8, 12, 16 and 20. Pad length is kept at the same value as the uniaxial bridges to allow for a direct comparison.
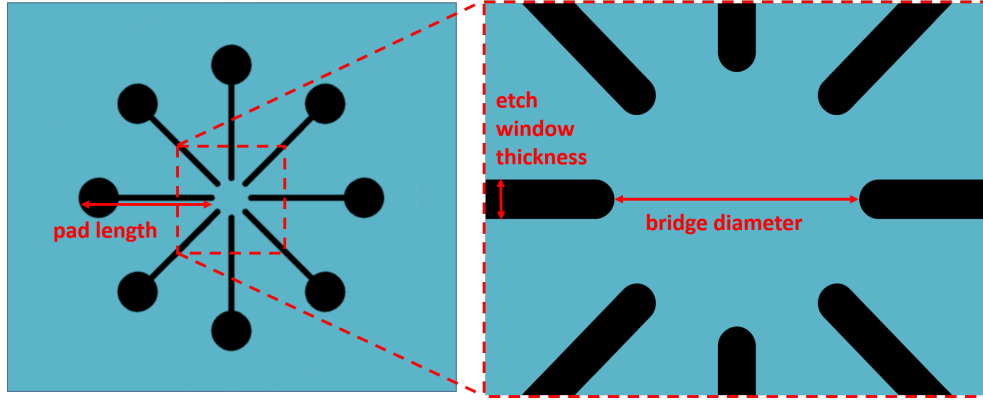
FIGURE 3.2: Exemplar polyaxial bridge design with 8 arms/etch windows. The central region is shown and the parameters etch window thickness and bridge diameter are shown.

3.3 Simulations

In this section FEM was employed using the software package COMSOL Multiphysics 5.3a to study and compare the mechanical stress and thermal sensitivity of uniaxial and polyaxial bridges.

3.3.1 Stress simulations

A common issue in mechanical design is stress concentration in which stress concentrates at specific points. Usually stress concentration occurs around air holes, this occurs in suspended bridges due to the etch windows. This stress concentration in the suspended bridges can result in mechanical failure, usually in the form of cracking. Stress concentration is is more severe for sharp corners and less severe for curves (and larger radius holes), this is why good suspended bridge designs employ curved etch windows. In this section we use the ' Structural Mechanics ' module to study corner stresses in uniaxial and polyaxial bridges. A 2D model was created with the bridge geometries. A fixed boundary was applied along the undercut boundary (i.e. where the suspension ends) assuming a 10 μm maximum under etch distance. The initial tensile strain in the system (from the epitaxial growth of Ge on to Si) was set to be 0.2%.

The Von Mises stress was plotted for each bridge, this stress was chosen as it factors in the shear components of the stress at which mechanical failure occurs at lower values, compared to equivalent pure symmetric stresses due to a higher distortion of the Ge crystal.In 2D, the Von Mises stress (σ_{VM}) is defined as:

$$\sigma_{VM} = \sqrt{\sigma_{xx}^2 + \sigma_{yy}^2 - \sigma_{xx}\sigma_{yy} + 3\tau_{xy}^2}$$

Where σ_{xx} and σ_{yy} are the x and y uniaxial stress components and τ_{xy} is the shear stress [103].

The bridge will undergo mechanical failure when the Von Mises stress anywhere in the bridge exceeds a critical value, this value depends on the material quality of the Ge. The central part of the bridge is designed to possess pure uniaxial / biaxial stress (and therefore strain) useful for potential devices. An important ratio is defined between the maximum Von Mises stress in the system (which results from the stress concentration around the etch windows) and the stress in the central region of the bridge. This ratio is labelled the Von Mises Ratio (VMR). The VMR is extremely important as it provides an idea of how much strain can be achieved in the central region of the bridge before mechanical failure occurs due to the maximum Von Mises stress in the bridge exceeding the critical value, therefore lower VMR values are more favourable.

The VMR values were plotted as a function of the relevant geometric parameters for each bridge. This is shown for the uniaxial bridges in Figure 3.3(a) and for the polyaxial bridges in Figure 3.4(a).

Polyaxial bridges have higher VMR values reaching a maximum value of 11.3 compared with the uniaxial bridges which reach a maximum value of of 3.4. The reason that polyaxial bridges posses larger VMR values is due to the presence of shear stresses (assymetric x and y components) at the stress concentrations which results in larger Von Mises stress. This explains why much lower strain values are achieved in polyaxial bridges.

Figure 3.3(a) shows the VMR for the uniaxial bridges as a function of bridge width for various values of bridge height. As bridge width increases the VMR drops and saturates at a value of 6.5 μm. As bridge height decreases the VMR also decreases and at a bridge height of 0.75 μm approaches unity. The Von Mises stress distributions for the two extreme geometries are shown in Figure 3.3(b) and Figure 3.3(c). In Figure 3.3(b). the bridge height is 0.75 μm and the bridge width is 10 μm corresponding to a VMR of 1.05. In Figure 3.3(c) the bridge height is 3.0 μm and the bridge width is 2.5 μm corresponding to a VMR of 3.5. Smaller bridge widths and larger bridge heights result in corners with smaller radii (i.e. are more sharp) resulting in greater stress concentration and therefore a higher VMR, this can be visualised in Figure 3.3(c). As the bridge height is decreased and the bridge width increased these corner radii are increased therefore reducing the stress concentration, as seen in Figure 3.3(b), resulting in a lower VMR. This suggests that the highest strain values should be achieved with lower bridge heights and larger bridge widths.

Figure 3.4(a) shows the VMR in polyaxial bridges as a function of bridge diameter and for various numbers of arms. Stress is inversely proportional to volume and the force is constant due to the fixed pad length used in this study. As the bridge diameter increases the stress therefore decreases, however the stress concentration does not scale

FIGURE 3.3: Results from the uniaxial stress simulations. (a) The influence of bridge width at different bridge heights on the VMR for uniaxial bridges. (b) Von Mises stress distribution of a uniaxial bridge with a bridge width of 10.0 μm and a bridge height of 0.75 μm. (c) Von Mises stress distribution of a uniaxial bridge with a bridge width of 2.5 μm and a bridge height of 3.0 μm.

proportionally resulting in a net increase in the VMR. As the number of arms increases the VMR decreases with 4 armed structures possessing extremely high VMR values (>8) as shown in Figure 3.4(b). The lowest values for the VMR occurs for bridges with 20 arms. The reason for this is the stress is concentrated over more points resulting in a lower stress concentration at each point and an overall lower VMR. However if the number of arms is to high and/or the bridge diameter is too small, the etch windows

FIGURE 3.4: Results from the polyaxial stress simulations. (a) The influence of bridge diameter at different numbers of arms on the VMR for polyaxial bridges. (b) Von Mises stress distribution of a polyaxial bridge with a bridge diameter of 6.0 μm and 4 arms. (c) Von Mises stress distribution of a polyaxial bridge with a bridge diameter of 3.0 μm and 20 arms.

become too close in proximity and high stress builds between them increasing the VMR. This explains why for 20 arms the 3.0 μm bridge diameter has a higher VMR for the 3.5 μm diameter, as visualized in Figure 3.4(c). It should be noted that if a large etch window was used for lower arm numbers the VMR would drop to a value comparable to the higher arm numbers, as the stress would be concentrated over a larger radius. However a larger number of arms are more favourable as they introduce more homogeneous strain [99].

3.3.2 Thermal simulations

For the thermal simulations the 'Heat Transfer In Solids' module was used in conjunction with a 3D geometry. The thickness of the Ge layer was fixed at 200 nm with an air gap underneath to simulate the suspension. The laser beam spot was defined in the center of each bridge. For all simulations, the pump wavelength was fixed at 532 nm and the spot diameter at 0.75 μm so the beam spot fit within all the designs allowing for a fair comparison. To accurately model the heating under optical pumping, the optical power was first calculated. The Fresnel equations were first used to calculate the reflectance and transmission of the incident light into the Ge layer, the beam profile was modelled as a 2D Gaussian function at the surface therefore accounting for lateral non-uniformity. The transverse non-uniformity was considered by implementing the Beer-Lambert law. The optical power distribution was subsequently used as a heat source under the assumption that all the optical power was converted to heat. The bottom of the silicon substrate underneath the air gap was set to be 20ºC as a fixed boundary condition.

The temperature increase (i.e. compared to an ambient of 20ºC) at the central point of the bridges was plotted as a function of the relevant geometric parameters to give an indication of the thermal sensitivity of the bridge (i.e. more thermally sensitive bridges result in higher temperature rises at equivalent pump power). This is shown for the uniaxial bridges in Figure 3.5(a) for different bridge widths and bridge heights and for the polyaxial bridges in Figure 3.6(a) for different bridge diameters and numbers of arms.

Due to the air gap underneath the bridges inhibiting efficient transverse thermal dissipation, the suspended bridges rely on lateral thermal dissipation from the central bridge region to the pads. The lateral thermal dissipation in turn relies on solid (i.e. Ge) thermal conduction paths and therefore will be inhibited by an increased area of the etchant window (i.e. air gaps) resulting in higher temperatures.

Figure 3.5(a) shows that for the uniaxial bridges, larger bridge widths and smaller bridge heights cause more heating and vice versa. The temperature profiles for the two extreme cases are shown in Figure 3.5(b) and Figure 3.5(c). In Figure 3.5(b) the bridge height is 3.0 μm and bridge width is 2.5 μm which corresponds to the smallest temperature rise of 125ºC. At larger bridge widths the heat from the center of the bridge has a further distance to travel to dissipate at the pads. In Figure 3.5(c) the bridge height is 0.75 μm and bridge width is 10.0 μm which corresponds to the highest temperature rise of 375ºC. At smaller bridge heights lateral thermal dissipation is reduced resulting in more heating, this results in severe heating at the lowest bridge height value of 0.75 μm.

Figure 3.6(a) shows that for the polyaxial bridges, smaller bridge diameters and a higher number of arms result in more heating and vice versa. The temperature profiles for the two extreme cases of the geometry are shown in Figure 3.6(b) and Figure 3.6(c). In
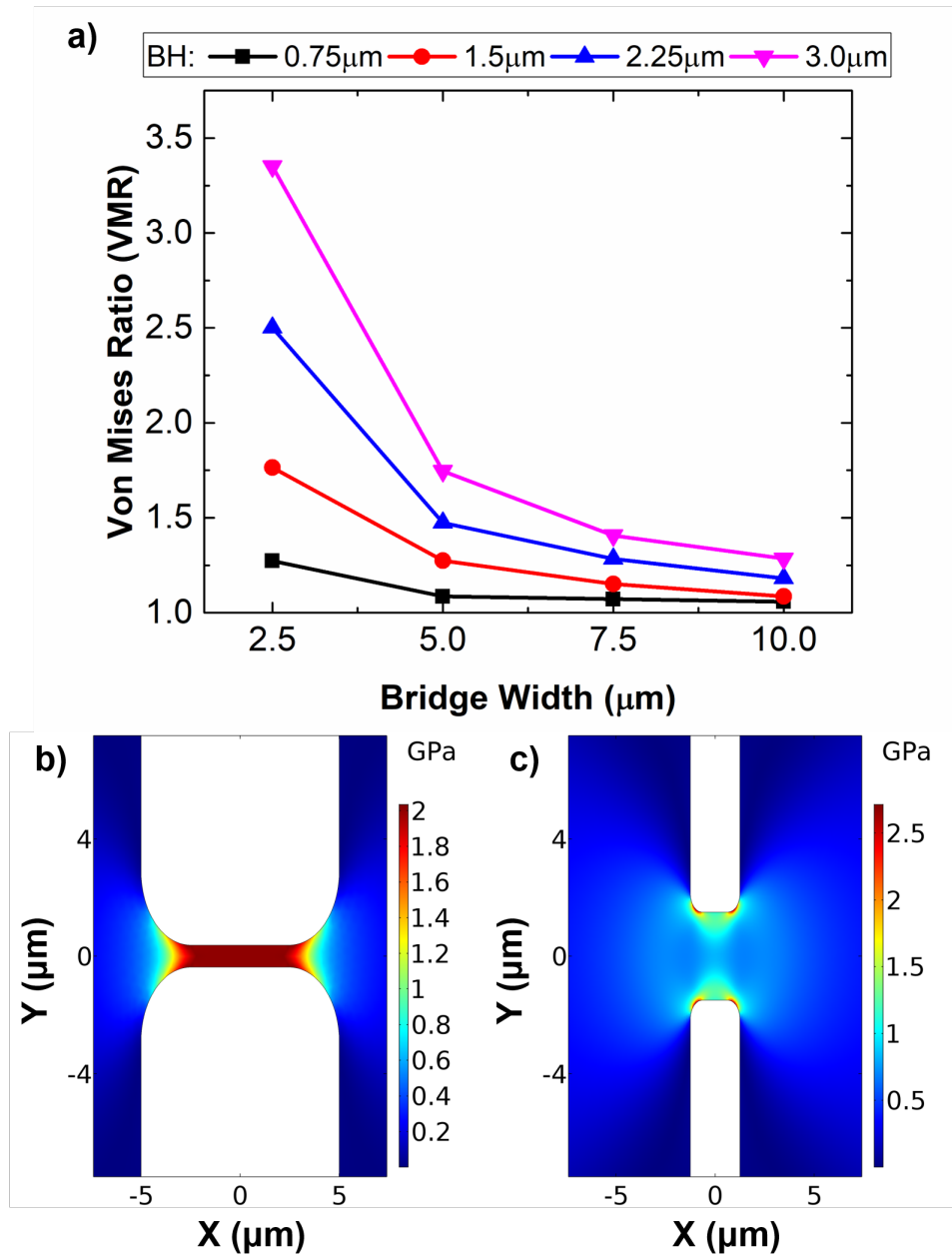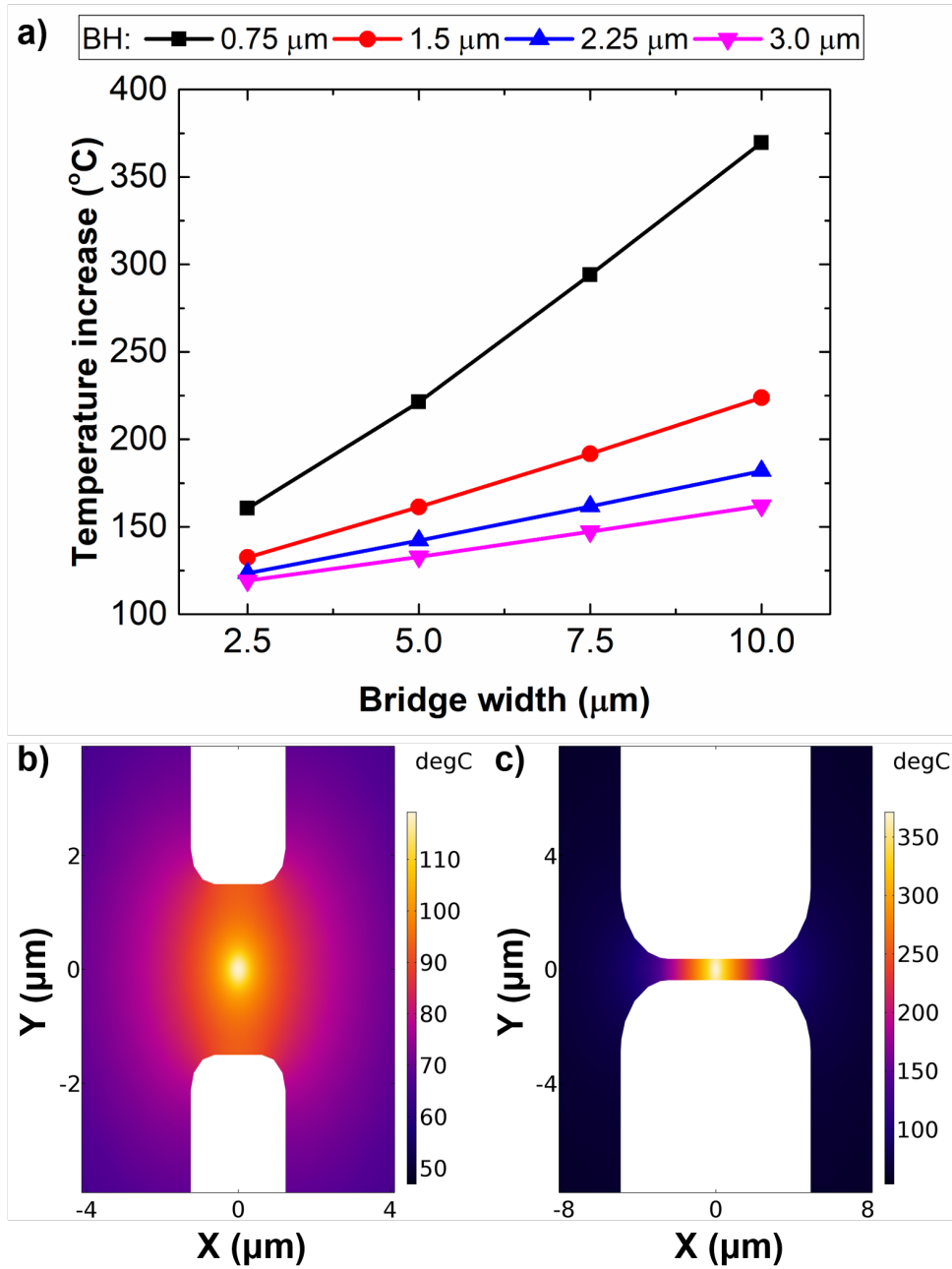
FIGURE 3.5: Results from the uniaxial thermal simulations. (a) The influence of bridge width at different bridge heights on the central temperature increase for uniaxial bridges. (b) The temperature distribution of a uniaxial bridge with a bridge width of 2.5 μm and a bridge height of 3.0 μm under 1 mW pump power. (c) The temperature distribution of a uniaxial bridge with a bridge width of 10.0 μm and a bridge height of 0.75 μm under 1mW pump power.

Figure 3.6(b) the inner diameter is 6.0 μm and the number of arms is 4 corresponding to the lowest temperature rise of 83°C. In Figure 3.6(c) the inner diameter is 3.0 μm and the number of arms is 20 corresponding to the highest temperature rise of 93°C. At smaller bridge diameters and higher number of arms the distance between etch windows is reduced restricting thermal dissipation from the bridge into the pads.
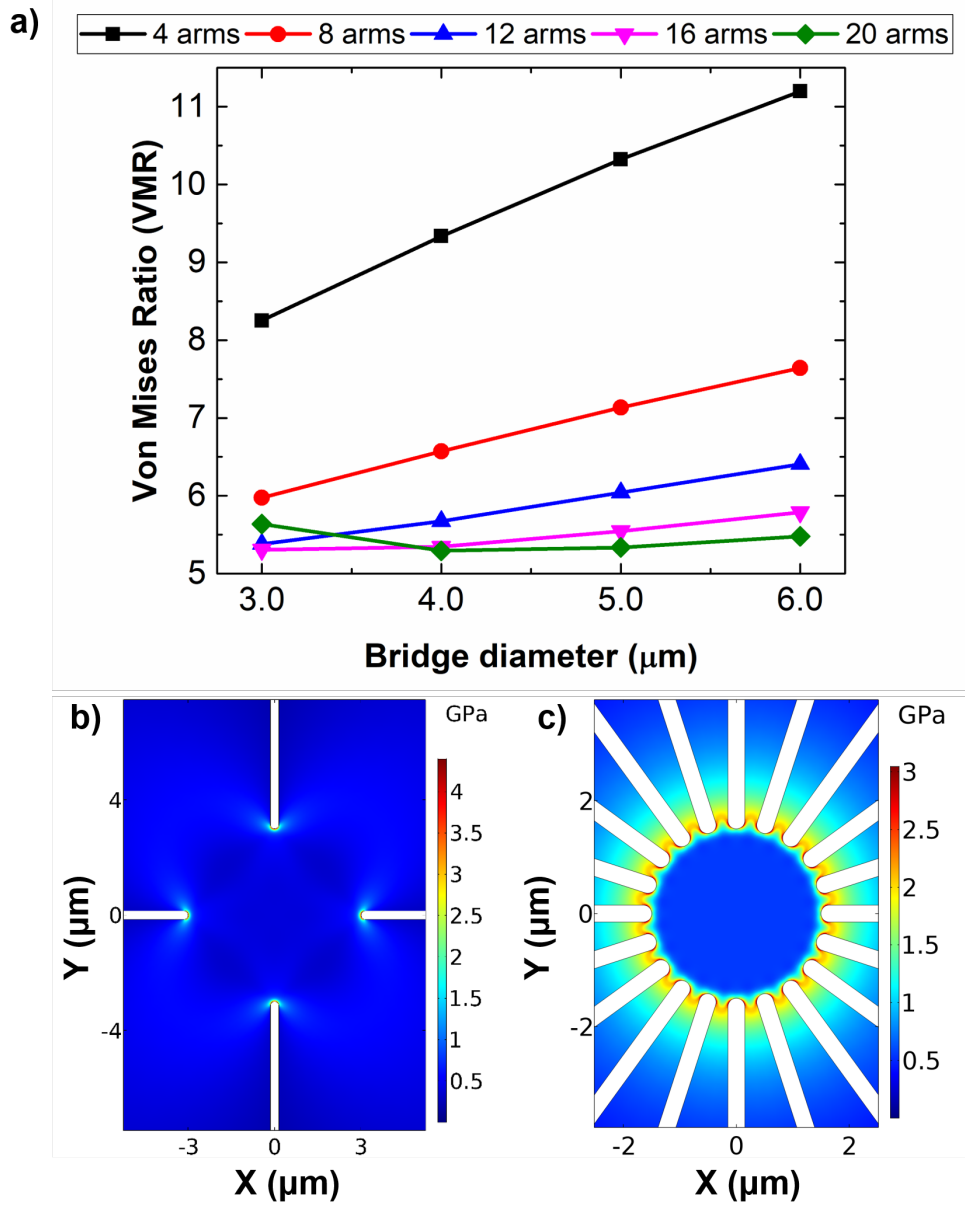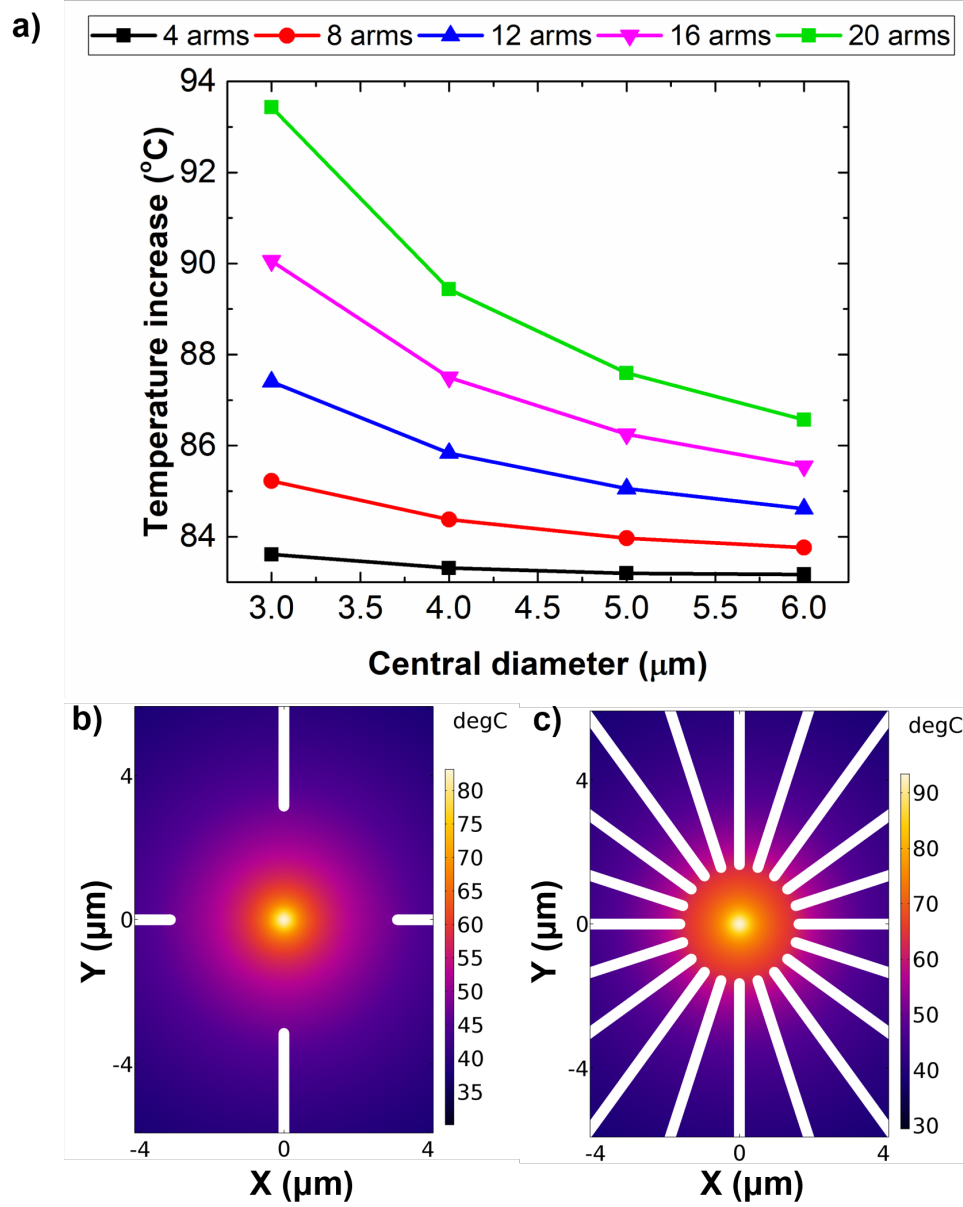
FIGURE 3.6: Results from the polyaxial thermal simulations. (a) The influence of bridge diameter at different numbers of arms on the central temperature increase for polyaxial bridges. (b) The temperature distribution of a polyaxial bridge with a bridge diameter of 6.0 μm and 4 arms under 1 mW pump power. (c) The temperature distribution of a polyaxial bridge with a bridge diameter of 3.0 μm and 20 arms under 1 mW pump power.

It should be noted that the range of temperature increase is larger for the uniaxial bridges (125 °C to 375°C) compared with polyaxial bridges (83°C to 94°C) meaning that the heating in uniaxial bridges are more sensitive to design parameters than the polyaxial bridges.

3.4   Experimental validation

3.4.1   Fabrication process

Figure 3.7 shows the main fabrication steps to produce the suspended bridges on two 1 cm by 1 cm chips taken from a Ge on SOI wafer. The chips were first cleaned to remove any organic contaminants from the surface using N-Methyl-2-pyrrolidone (NMP) under sonication followed by rinsing with Iso-Propyl Alcohol (IPA). This was followed by the spin-coating of the electronic resist ZEP520A. Electron beam lithography (EBL) was then used to define the etching windows (and therefore the bridges). After development the chips underwent Inductively Coupled Plasma (ICP) dry etching using CHF_3 and SF_6 chemistry removing the Ge and SOI and exposing the Buried Oxide (BOX) thus forming the etch windows. The remaining resist was then removed using elevated temperature NMP followed by IPA. Both chips underwent liquid HydroFluoric (HF) acid etching to remove the sacrificial BOX underneath the bridges and suspend the bridges. Due to the small Ge layer thickness of 200 nm and also the small BOX thickness of 145 nm stiction was a concern. A simple tuning of the gap underneath the Ge was developed to prevent stiction, one chip was placed into TetraMethylAmmonium Hydroxide (TMAH) after the HF suspension and rinsing with De-Ionised (DI) water with no drying step in between to tune etching of the Si handle layer increasing the gap underneath the bridges. After all the etching steps both chips were rinsed in DI water and dried using a nitrogen gun. This tuning resulted in a gap of around 10 μm underneath the Ge and used to reduce capillary forces during the subsequent drying step to prevent stiction. The structures that underwent the additional TMAH etching to make the gap underneath the bridge larger will be referred to as "tuned". Conversely the structures that just underwent HF etching will be referred to as "not tuned".

3.4.2   Optical micro-graphs and yield analysis

Figure 3.8 shows exemplar optical micro-graphs of the successfully fabricated Ge bridges with the uniaxial bridges on the top row and polyaxial bridges on the bottom row. Furthermore bridges with identical designs which were not tuned are shown on the left hand side with bridges that were tuned shown on the right hand side. The etchant windows in the uniaxial and polyaxial bridges can be seen to be visibly darker in the tuned bridges indicating a much deeper gap suggesting the tuning process was successful.

Figure 3.9 shows the percentage survival rate of the 60 uniaxial and 60 polyaxial bridges (i.e. the percentage of bridges that had not undergone mechanical failure) for both the tuned and not tuned bridges. The uniaxial bridges had a much higher survival rate compared with the polyaxial designs. The polyaxial bridges that were not tuned have a survival rate of 8.1% whereas the uniaxial bridges have a much higher 45.0% survival
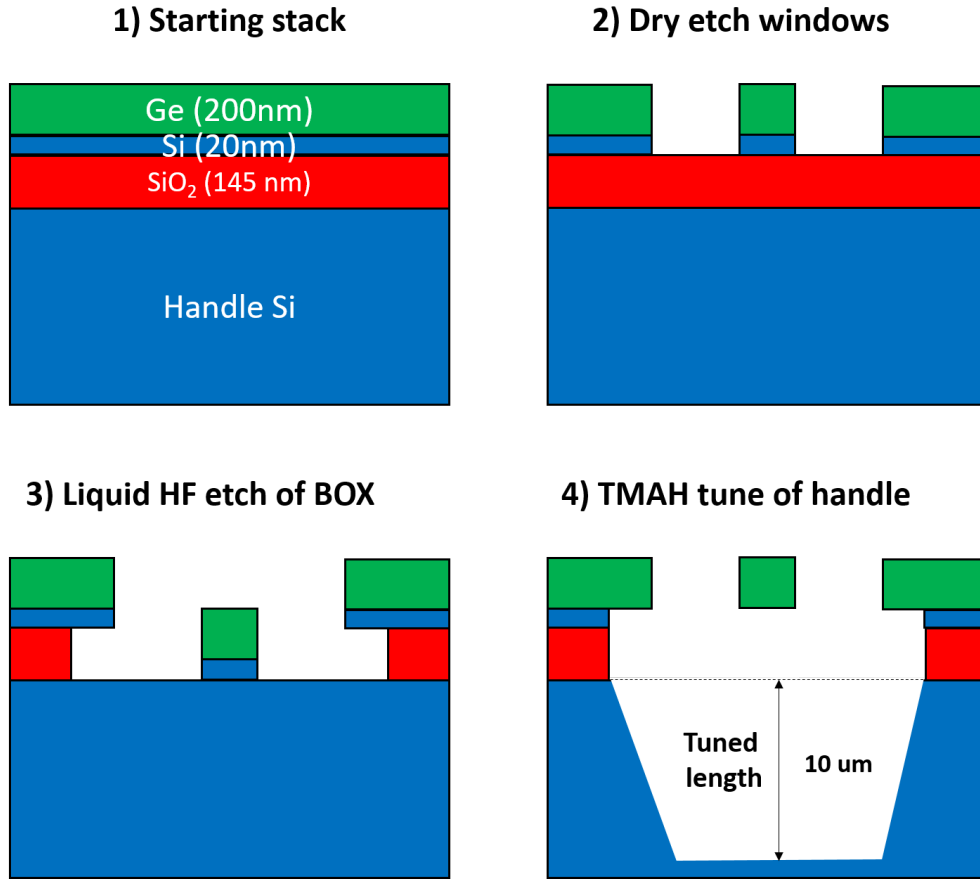
FIGURE 3.7: A schematic showing the starting wafer stack of the Ge on SOI platform and the main stages of fabrication.

rate. The polyaxial bridges that were tuned had a survival rate of 15.0% whereas the uniaxial bridges that were tuned again had a much larger 75.0% survival rate. This agrees with the results of the stress simulation as the polyaxial bridges have a much lower survival rate due to higher corner stresses and thus higher VMR values. The fact that the tuned bridges have a larger survival rate than the bridges that were not tuned, is likely due to the larger capillary forces introduced during drying in the not tuned bridges. The capillary forces act on the fragile highly stressed bridges causing mechanical failure. This reduction of bridge survival due to larger capillary forces is supported by the fact that the highest strained structures reported in literature utilized a dry release thus eliminating the need for a drying step and thus drastically reducing the capillary forces [104, 89, 105]. This simple tuning technique can be applied not only to prevent stiction, which was the original goal, but also to improve the yield of bridges and achieve higher strain values. The aim of this study was to focus on fully suspended bridges and not bridges that had undergone stiction to the underlying Si (which would cause optical leakage in actual laser diode devices (Appendix B)).
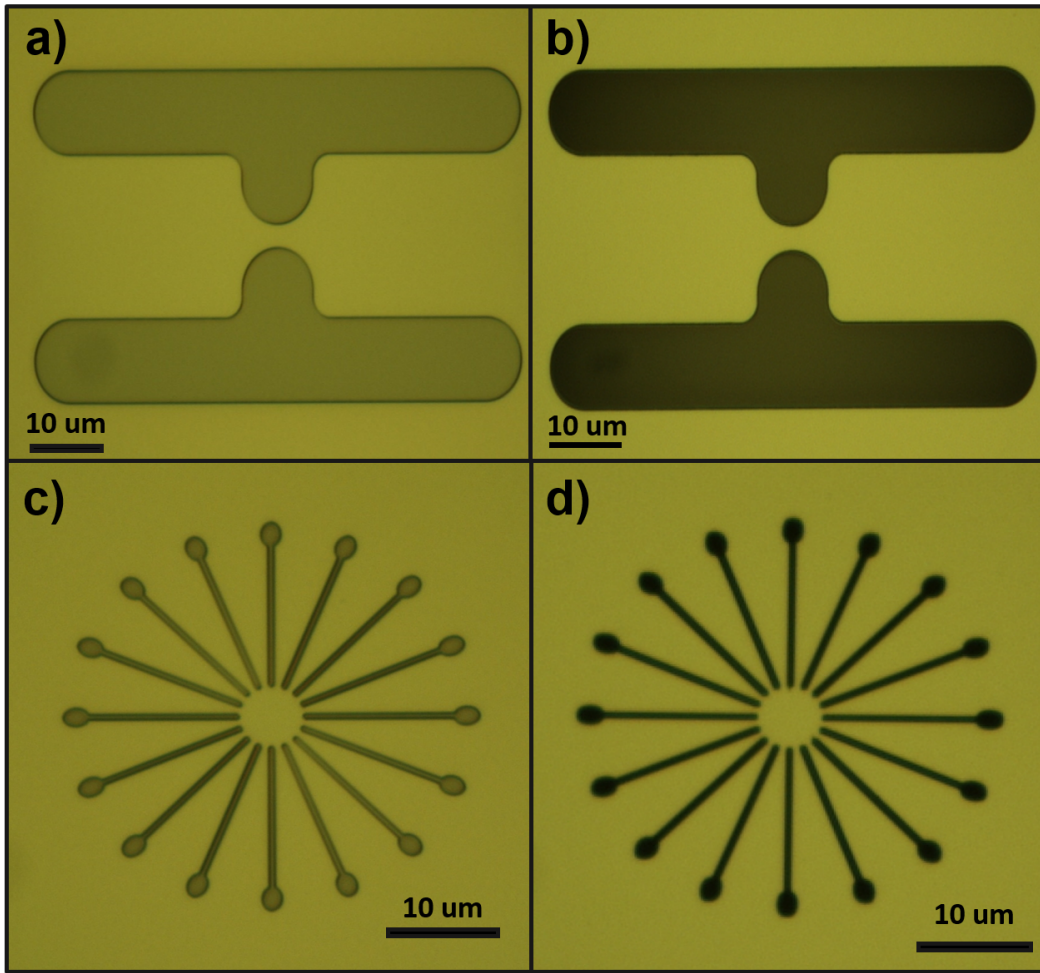
FIGURE 3.8: Surviving uniaxial (top row) and polyaxial (bottom row) for the not tuned (left column) and tuned (right column) bridges.

3.4.3   Raman spectroscopy

Raman spectroscopy was used to validate the results of the stress and thermal simulations. A continuous wave green laser with a wavelength of 514 nm was used to excite the bridges. A 50x objective lens was used to focus the laser spot onto the central area of the bridge resulting in a spot diameter of around 1.0 μm. The signal was collected using the same objective lens and reflected into a high resolution grating of 3000 lines/mm. The exposure time was set to 10 s and the spectra were averaged 12 times for a total measurement time of 120 s per bridge. The Raman spectra were fitted with Lorentzian functions in order to estimate the peak position.

For measuring the strain, an optical power of 46 μW was used after testing the power dependency and showing negligible heating effects (which cause an error in the strain measurement). Shifts in Raman peak position relative to a bulk Ge sample ($\Delta\omega$) were deduced allowing the strain (ϵ) to be calculated using the equation: $\epsilon = \Delta\omega$ x C. Where

FIGURE 3.9: Bar graph comparing the survival rate of uniaxial and polyaxial bridges with and without tuning.

C is a proportionality factor reported in literature to be 390 cm^{-1} [68] for biaxial strain and 152 cm^{-1} for uniaxial strain [88].

Figure 3.10(a) shows the Raman spectra of the polyaxial and uniaxial bridges with the highest strain. The uniaxial bridge with the highest uniaxial strain value of 2.55% had a bridge height of 0.75 μm and a bridge width of 7.5 μm. This coincides with the results of the simulations in which the VMR was lowest for smaller bridge heights and widths. The polyaxial bridge with the highest biaxial strain value of 0.75% had a bridge diameter of 3.0 μm and 20 arms. This also agrees with the stress analysis of the polyaxial bridges which showed that lower bridge diameters and a higher numbers of arms possessed a lower VMR.

For validating the thermal simulations, two exemplar bridges were compared with the simulation results: one polyaxial and one uniaxial. The uniaxial bridge had a bridge width of 7.5 μm and a bridge height of 10.0 μm. The polyaxial bridge had a bridge diameter of 3.0 μm and 20 arms. The Raman spectra were recorded at 0.1, 0.5 and 1.0 mW of power and the peak positions were extracted with Lorentzian fitting. The peak positions were plotted as a function of power and a linear fit was performed and extrapolated to the y-axis to give the peak position under zero power and remove the effect of strain. The difference of the Raman positions at each power with this zero power
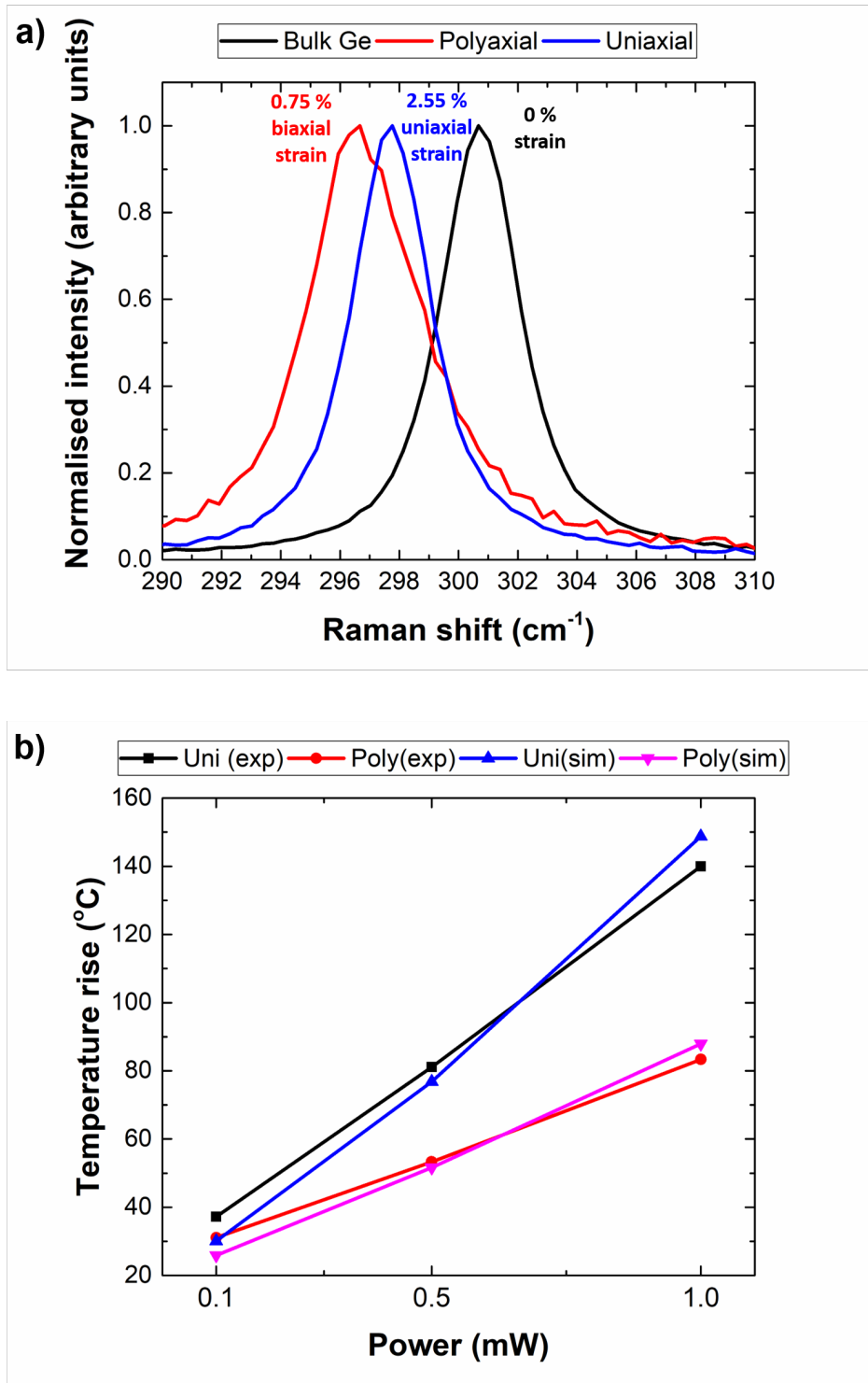
FIGURE 3.10: The results of the Raman spectroscopy. **(a)** Raman spectra of the bulk Ge sample and the bridges with the highest uniaxial and biaxial strain. **(b)** Temperature rise from finite element modelling and Raman thermometry for an exemplar uniaxial and polyaxial bridge to verify simulation results.

position were then calculated and the temperature rise was calculated assuming a linear relationship with the Raman shift and dividing the Raman shift by the constant 0.0160

cm^{-1} K^{-1} [106]. The temperature increase was plotted as a function of power and the results of simulations under identical conditions were also plotted in Figure 3.5(a) and Figure 3.6(a). As shown in Figure 3.10(b) the simulation data is in excellent agreement with the experimental data.

3.5   Discussion

For uniaxial bridges there is a severe trade off between achieving higher strain and minimizing heating. Smaller bridge heights and larger bridge widths favour higher strain. This is supported by literature, with the highest uniaxial strains reported possessing bridge heights in the range of 200.0 nm and bridge widths of 4.5 μm [89, 90, 60]. However smaller bridge heights and larger bridge widths result in higher temperatures meaning the bridge designs that allow for the highest strain are also extremely thermally sensitive.

For polyaxial bridges there is also a trade off between achieving higher strain and minimizing thermal sensitivity. Larger numbers of arms and smaller bridge diameters result in lower shear stresses and thus a higher achievable strain (and also improved strain homogeneity), but this results in higher thermal sensitivity and vice versa. However the dependence of thermal sensitivity on geometric parameters in polyaxial bridges is small when compared to the uniaxial bridges, as shown in the simulation section of this study.

Polyaxial bridges have been less extensively explored compared to uniaxial bridges, mostly due to the lower amount of strain achieved. However the results from this study combined with recent reports in literature suggest that polyaxial bridges are actually more favourable to their uniaxial counterparts. The highest achieved uniaxial strain in uniaxial bridges was 4.9% whereas the highest biaxial strain in polyaxial bridges was 1.9%. But recent theoretical and experimental evidence shows that, the amount of strain required to convert Ge into a direct bandgap material is three times larger for uniaxial strain (6.0%) compared to biaxial strain (2.0%)[47, 46]. Therefore polyaxial bridges not only possess superior thermal management, but they are also closer to achieving the direct bandgap configuration in Ge.

Furthermore to achieve the highest strain in uniaxial bridges, the bridge width must be very small. In literature the highest values of 4.9% were only achieved in extremely thin nanowires with wire heights of 200 nm. However this will result in extreme heating, causing unacceptable optical losses. Furthermore an optical mode is extremely difficult to confine in such a narrow wire [89].

With uniaxial bridges, as the VMR has almost approached unity by careful design, to further increase the strain the material quality must be improved (i.e. dislocations reduced) to prevent fracturing. On the other hand the VMR in polyaxial designs is still larger than unity. This offers an opportunity to introduce higher biaxial strain by

improving the design to reduce corner stress. In other words the maximum strain in uniaxial bridges is inherently limited by material quality whereas polyaxial bridges have the potential to achieve higher strain and therefore optical gain by improved designs.

One major issue preventing the achievement of room temperature operation is absorption due to intra-band transitions. Gupta *et al* showed by modelling the Inter Valence Band Absorption (IVBA) under the influence of strain, that for certain uniaxial strain values, there was a resonance between the gain and loss mechanisms[45]. It was theoretically predicted that net gain was achieved between 4% to 5% uniaxial strain. This has an important implication that strain must be optimised, and not just increased indefinitely, to achieve room temperature lasing. However the cross over from direct bandgap in the study by Gupta *et al* is underestimated at 4.6% (1.4% underestimation) which means the range of strain value at which the optimum gain is achieved is also underestimated. The largest uniaxial strain achieved in literature is 4.9% and therefore is still not optimum. One must also considering the limitations of introducing more uniaxial strain. Therefore polyaxial bridges introducing biaxial strain offer a more effective way to achieve these ideal strain value for minimising absorption losses and maximising optical gain.

Finally it should be noted that the temperature rise for bridge suspended in air is still too large for practical device operation. Stiction to the underlying Si would drastically improve thermal management due to the high thermal conductivity of Si (i.e. in 'not tuned' structures). However if the Ge undergoes stiction to the Si the refractive index contrast is low introducing large optical losses and therefore is avoided. Previous studies in suspended bridges have utilised stiction to SiO_2 to maintain a large refractive index contrast whilst providing transverse thermal conduction paths for the bridges[93, 34, 94]. However SiO_2 still has a relatively low thermal conductivity when compared to Ge or Si (around 2 orders of magnitude lower). Future work can involve combining optimised polyaxial bridges to provide excellent lateral thermal heat dissipation with the transverse thermal heat dissipation into the SiO_2. This will not only drastically improve the thermal management to an acceptable level in the bridges, but by using higher quality GOI will allow for higher biaxial strain values to be achieved.

3.6   Conclusions

We have investigated uniaxial and polyaxial bridges in terms of mechanical stress and thermal sensitivity. FEM showed that the polyaxial bridges suffered from large corner stresses thus inhibiting large strain to be achieved. On the other hand uniaxial bridges can be designed to have negligible corner stresses allowing higher strain to be achieved. However FEM also revealed that uniaxial bridges were much more thermally sensitive under optical pumping which will cause detrimental optical losses in potential laser devices. To provide verification of the simulation results, suspended bridges were

fabricated and underwent Raman spectroscopy which showed excellent agreement with the simulations. With the lower thermal sensitivity and less strain required for a direct band gap configuration, we argue that despite being overlooked compared with uniaxial bridges, polyaxial bridges have great potential for lasing.

Chapter 4

Enhanced light emission from improved homogeneity in biaxially suspended Germanium bridges from curvature optimization

In this chapter, we aimed to address the discrepancy between the theoretical and measured enhancement in light emission in biaxial Ge bridges by improving the homogeneity removing the high point corner strains. Biaxial bridges have suffered from poorer optical and mechanical properties compared to uniaxial. One main reason for this was homogeneity and in particular point stress concentrations, this work aimed to address this to improve homogeneity to make biaxial bridges a more viable option for light sources. We propose a novel geometric approach to explore the role of curvature on the strain distribution in an attempt to improve the strain homogeneity using finite element simulation. Devices were fabricated using a Ge on Si wafer stack. The bridges were then characterized using μ-Raman spectroscopy to measure the central strain value and μ-PL to study the effect on light emission. By comparing the micro-PhotoLuminesence(μ-PL) measurement with micro-Raman (μ-Raman) spectroscopy and Finite Element Modelling (FEM), we confirmed that point strain concentrations were responsible for degrading the μ-PL intensity. Curvature optimization is then required to improve homogeneity, which in turn improved light emission

Published in [1]

4.1   Design and Simulation

4.1.1   Design

A unique geometric approach was employed to enhance the strain in the central area of the bridge whilst minimizing point strain concentrations whilst parametrically exploring the role of curvature. The bridges are comprised of four arms, Figure 4.1 schematically shows how the half arm geometry was developed. The final four-armed geometry can be formed using copying, rotation and translation.
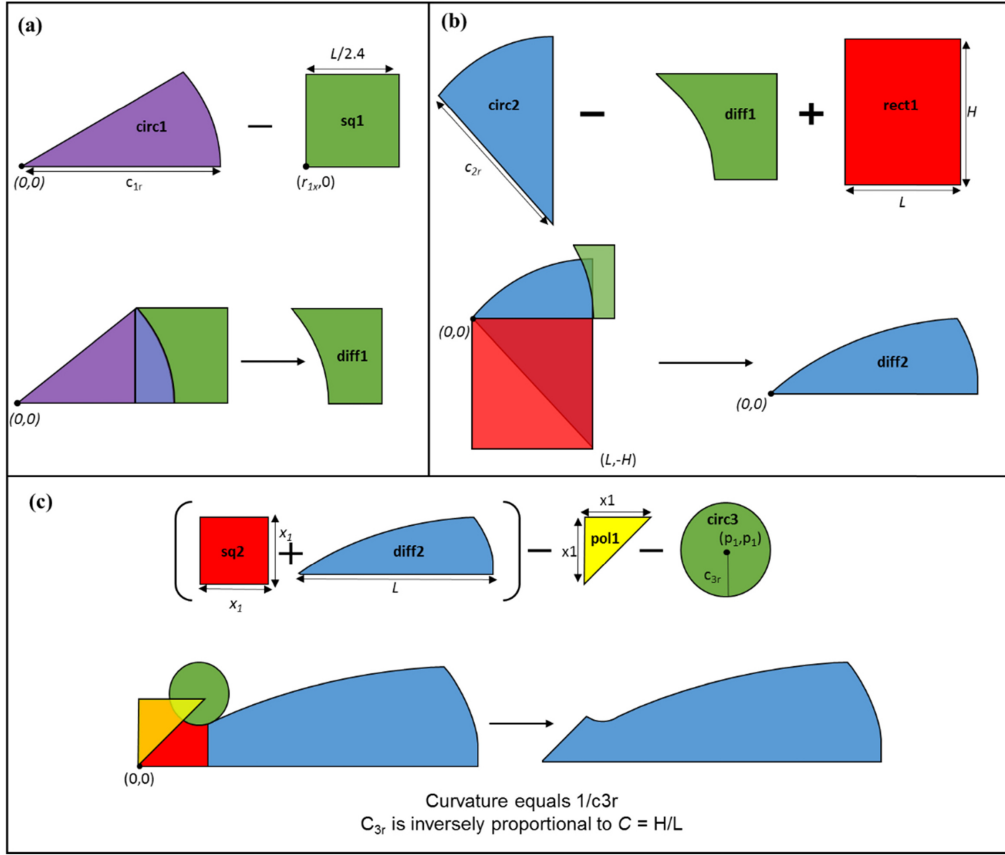
FIGURE 4.1: Overall schematic of geometry design for half an arm with (a) Step 1 (b) Step 2 and (c) Step 3.

The first step involves defining a geometric difference 'diff$_1$' between a circular segment 'circ$_1$' and square 'sq$_1$' as shown in Figure 4.1(a); this difference 'diff$_1$' defines the curve at the extremity of the half arm. The square sq$_1$ has dimensions that equal L/2.4 where L is arm length, its y position is fixed at 0 and the x position (labelled 'r$_1$x') is given is also given in terms L, shown below as:

$$r_1x = L - (0.5(L/2.4)) \quad (1)$$

Circular segment 'c1' has its center at coordinates (0, 0) with a constant sector angle of 30. The properties of 'sq$_1$' define the radius of the circular segment 'c$_1$r' as shown as:

$$c_1 r = r_1 x + (0.5 r_1 w) \quad (2)$$

The second step involves defining the main bulk of the arm geometry. This step uses a circular segment 'circ$_2$' as well as a rectangle (labelled r$_1$). The rectangle 'r$_1$' and the difference 'diff$_1$' (defined in step 1) are subtracted from the circular segment 'circ$_2$' as shown in Figure 4.1(b). The rectangle 'rect$_1$' has a width equal to the arm length L and a height defined as H, furthermore it must be displaced in the y-axis by -H. Curvature ratio C can now be defined as:

$$C = H/L \quad (3)$$

The circular segment 'circ$_2$' is rotated 90 degrees and displaced in the x direction by L and in the y direction by – H. 'circ$_2$' has a sector angle defined as gamma which is defined by an angle θ (note θ is not shown schematically for simplicity but shown mathematically). 'circ$_2$' has to have a radius 'c$_2$r' shown in Figure 4.1(b) and is given by:

$$c_2 r = H/cos(\gamma) \quad (4)$$

The value of C must be greater than unity otherwise the arc will over extend compromising the geometry. This is shown in Equation (5) and Equation (6) below:

$$\gamma = 90^o - \theta^o \quad (5)$$

$$\theta = tan^{-1}(H/L) = tan^{-1}(C) \quad (6)$$

The third step involves defining the curvature of the arm based on C achieved using a circle ('circ$_3$). A square labelled 'sq$_2$' is added with its corner at (0, 0) and dimensions p$_2$x defined by Equation (7) below with another required parameter 'p$_2$y' defined as:

$$p_{2x} = (L - (H/cos(\gamma))(cos(\theta + \beta)) \quad (7)$$

$$p_{2y} = ((H/cos(\gamma))(sin(\theta + \beta) - H) \quad (8)$$

Beta is an input parameter, which defines the central area, which for the purpose of this study is adjusted to give a fixed central circular area with diameter of 5.6 μm m. 'P$_1$' defines the center coordinates of the circle 'circ$_3$'; it can be calculated by:

$$P_1 = \frac{1}{2L} - \frac{(sin(\gamma - \beta))(H + L)}{(sin(135 - (\gamma - \beta)))} \quad (9)$$

To provide the curvature 'circ$_3$' must be subtracted from the rest of the bridge. The circle c$_3$ has central coordinates: ('P$_1$', 'P$_1$') and radius 'c$_3$r', which is given by:

$$c_3r = \sqrt{(p_2x - p_1x)^2 + (p_2y - p_1y)^2} \quad (10)$$

Finally, a polygon ('pol$_1$') is created to cut the bridge at a 45º angle. After this, the half arm can be mirrored horizontally then copied and rotated to form the final four armed bridge. Furthermore, the curvature ratio can be altered resulting in varying geometries (as can be visualized in Figure 4.2.)
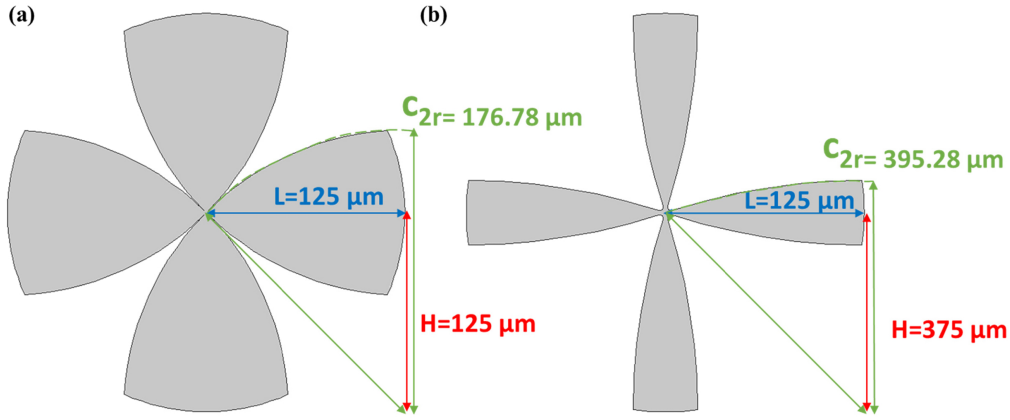
FIGURE 4.2: Schematic of four arm structure with (a) C = 1.0 and (b) C = 3.0. The parameter L is fixed at 125 m (shown in blue) and the corresponding parameters H (shown in red) and c$_2$r (shown in green).

4.1.2 Simulation

FEM using COMSOL Multiphysics v5.2 was used to study the strain homogeneity in the Ge bridges from C = 1.0 to C = 3.0 in increments of 0.2. The 'Transport of dilute species' module was used, assuming an isotropic diffusion to model the under-etchant profile fitted to a maximum etching distance of 25 μm. The 'Structural mechanics' module was then used assuming an initial strain of 0.18% in the bridge. The diffusion profiles were used to define a fixed constraint boundary condition. The central area had a fixed diameter of 5.6 μm. The central strain, maximum strain and the ratio between central and maximum strain were plotted as a function of C as shown in Figure 4.3. Figure 4.3(a) shows the central strain decreases steadily as C increases; this is expected due to reduced pad size. This means the highest central strain values are in low C bridges. However Figure 4.3(b) shows the maximum strain is also largest at low C; the

maximum strain rapidly decreases from C = 1.0 to C = 1.4 and then decreases slowly. The high corner strain concentrations degrade both optical and mechanical properties therefore these low C values are likely not suitable for practical applications.

Figure 4.3(c) shows that the ratio between the central and maximum strain saturates at a value of around C = 1.8, at this point the largest central strain can be achieved whilst minimizing the maximum strain which in turn should increase resistance to plastic deformation and prevent detrimental carrier diffusion away from the central active region.
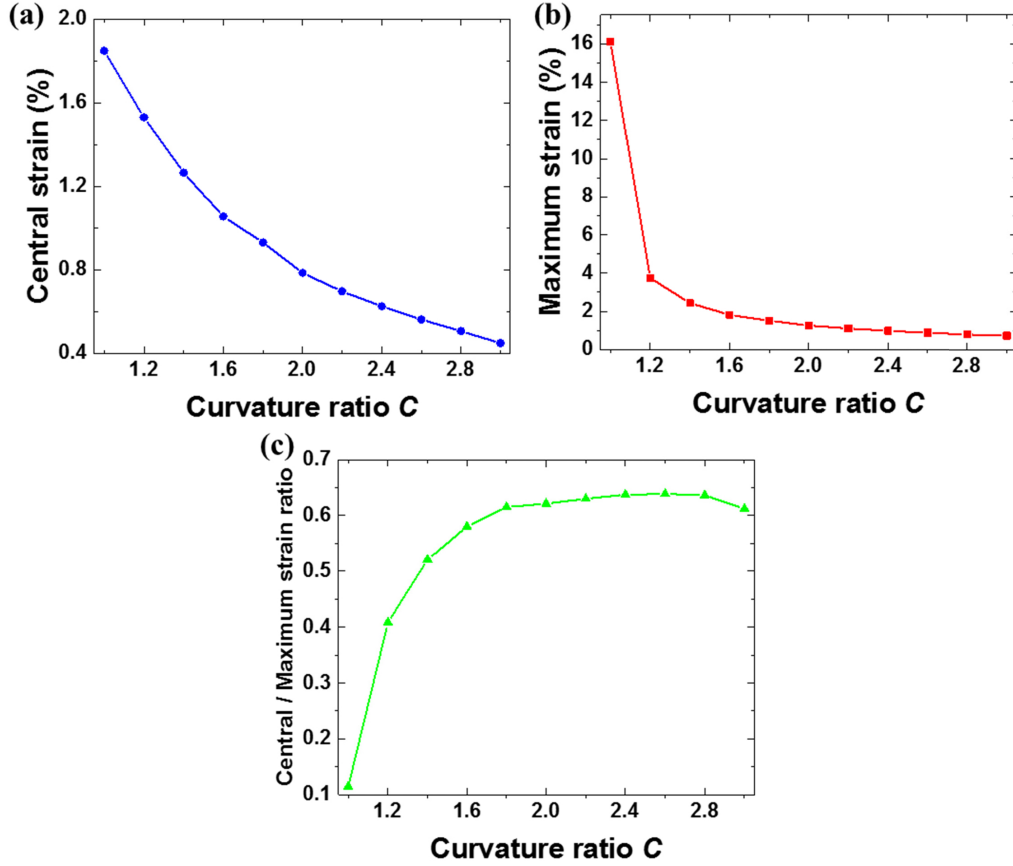
FIGURE 4.3: The effect of C on (a) Central strain. (b) Maximum strain (c) The ratio between central and maximum strain.

Figure 4.4 shows the strain distributions at various C values. 2D simulations are sufficient as the thickness of each bridge is identical. The tensile strain has been enhanced in the central region whilst compressive strain exist in the pads, as the force is constant in the bridge for the tensile enhancement in the central region to occur the pads must compress. The maximum strain regions decrease in magnitude as C increases however they increase in size and shape, furthermore they migrate further from the central region as C increases. Figure 4.4(a) shows the strain distribution at C = 1.0, the maximum strain is concentrated in very small corner regions near the apex of the etchant windows in the central region. These extremely high point biaxial strain concentrations will likely cause mechanical failure, furthermore optical properties may be degraded. Figure 4.4(b)

shows the strain distribution at C = 1.4, the gradient between the maximum and the
central strain is more gentle but these bridges are still likely to have poor optical and
mechanical properties due to the high point strain concentrations.
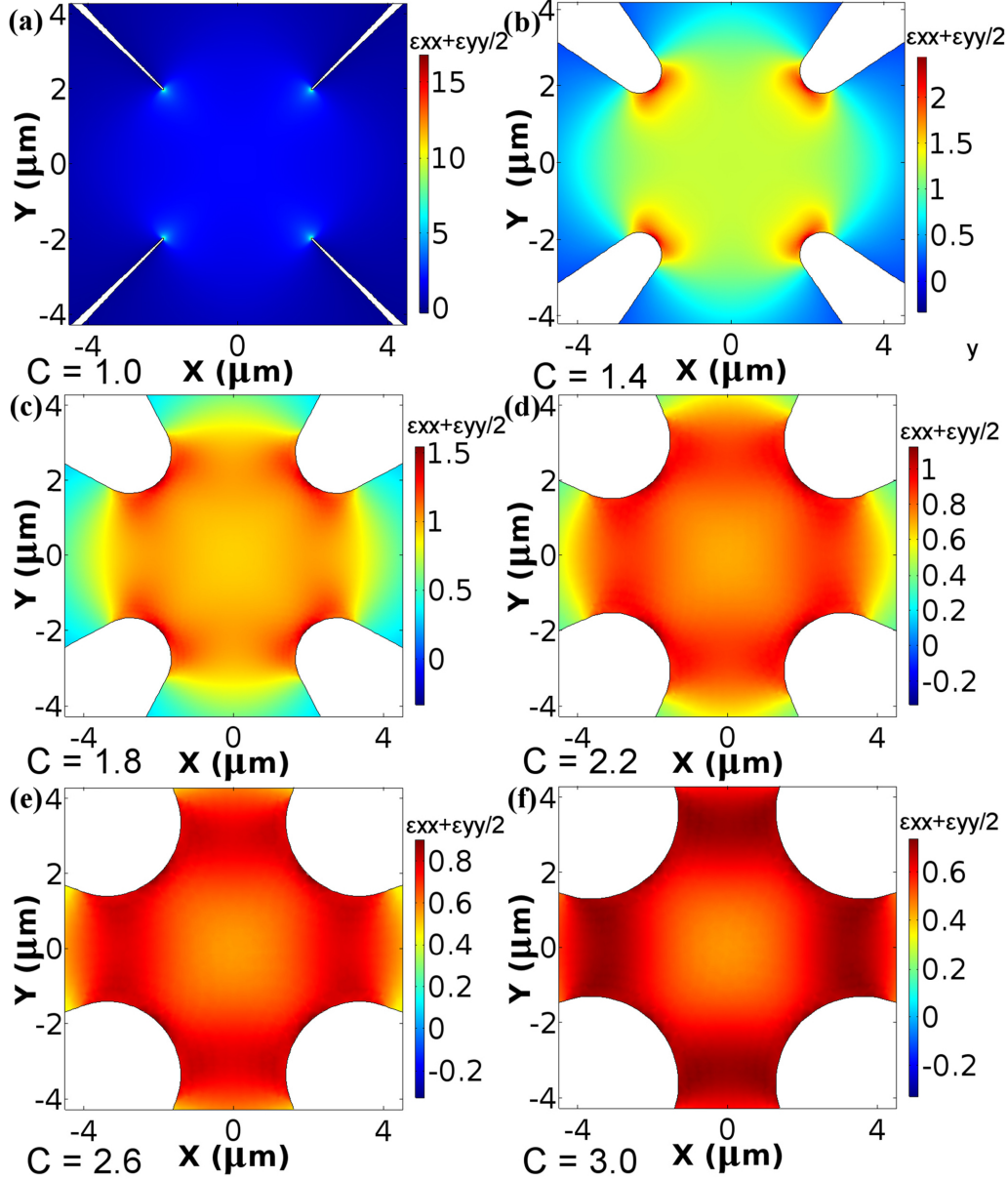
FIGURE 4.4: Strain distributions at C values of (a) 1.0 (b) 1.4 (c) 1.8 (d) 2.2 (e) 2.6
and (f) 3.0.

Figure 4.4(c) shows the strain distribution at C = 1.8 which has a more gentle strain
gradient and improved homogeneity. Figure 4.4(d) shows the strain distribution at C =
2.2, the homogeneity is very good at this point and the corner strain concentrations are
much smaller. Figure 4.4(e) shows an interesting deviation from typical distributions in
biaxial bridges exhibiting corner strains; the maximum strain begins to form into four
rectangular regions just outside the main central region. In fact despite these regions
having a higher value, the strain values are not purely biaxial and are asymmetric in

nature, this reduces unfavorable carrier diffusion and subsequent recombination. Figure 4.4(f) shows the bridge at C = 3.0, the maximum strain forms more distinct and stronger rectangular regions located outside the central regions in the pads. bridges with C > 2.6 show unique strain profiles, which deviate from previous works. These maximum strain regions highly asymmetric with varying contribution from the uniaxial strain components xx and yy. As the central strain is purely biaxial, a smaller strain value is required to reduce the direct band-gap relative to the corresponding uniaxial strain. In turn, the band-gap variation is not as large as the typical strain profiles in these bridges with high corner strains (low C regime). With increasing C eventually the central region will become compressive in nature. Whilst the maximum strain to minimum strain ratio is a good indication of homogeneity it is not a definition, the spatial strain profiles must also be considered in particular the size and location of the maximum strain regions. At higher C, the maximum regions are further away from the central region reducing pseudo-hetero-junction effects. Furthermore they are less concentrated at the dry etched interfaces potentially minimizing surface non-radiative recombination and roughness induced scattering.

4.2 Experimental

4.2.1 Fabrication

A Ge on Si material stack was chosen to fabricate the suspended bridges. The Ge layer was 532 nm thick, etching windows were patterned using Electron Beam Lithography (EBL). This was followed by Reactive Ion Etching (RIE) exposing the handle Si. Finally, a TetraMethylAmmonium Hydroxide (TMAH) wet underetch of the Si layer was performed resulting in an etching distance of 25 μm. Optical microscopy was used to observe the bridges, from inspection it was noted that all of the low C bridges were destroyed during fabrication (1.0 - 1.3), this was expected due to the high point strain concentrations. An optical micro-graph of a surviving bridge is shown in Figure 4.5 corresponding to C = 3.0.

4.2.2 μ-Raman spectroscopy

μ-Raman spectroscopy was performed to deduce the strain value in the central region of the bridges. A green laser (532 nm wavelength) with a 100x objective lens at a power of 100 μW resulting in a spot size with around a 1 μm diameter. Previous work from our group has determined the power dependency on the Raman peak position [86], a 100 μW power was used to make heating effects on the peak position negligible. Bridges with C values of 1.4, 1.6, 1.8, 2.0, 2.5 and 3.0 to study the effect of curvature ratio (and thus curvature) on the strain. Figure 4.6(a) shows the μ-Raman spectra obtained. bridges
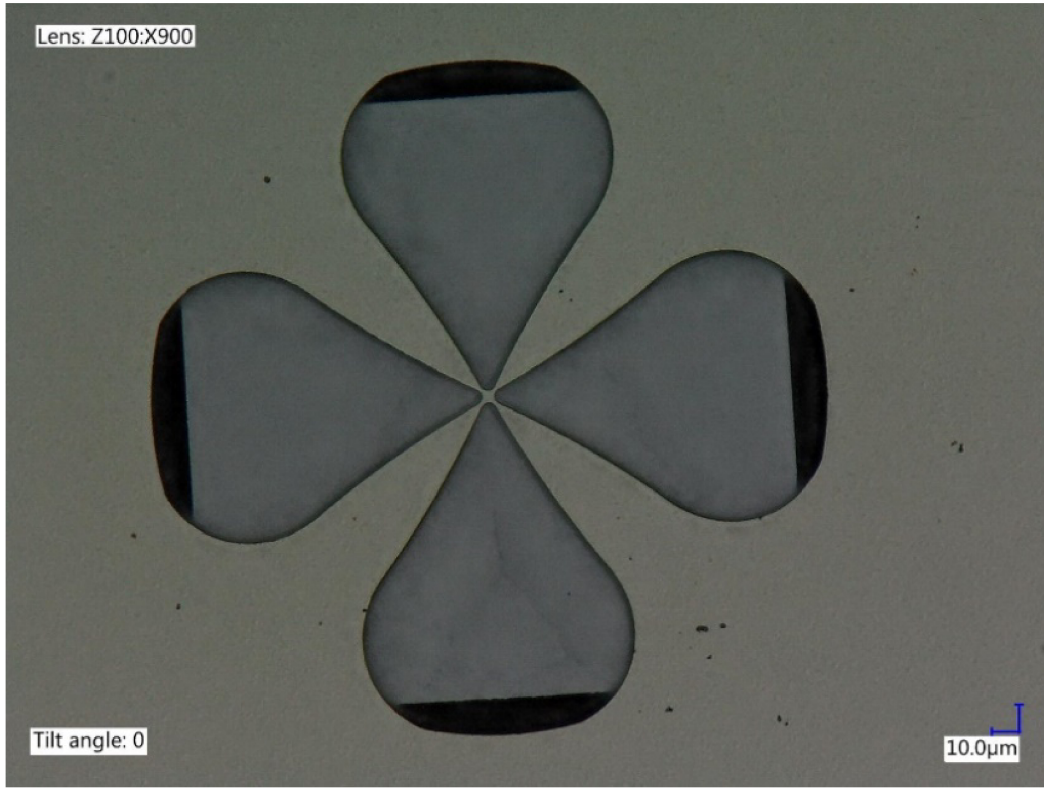
FIGURE 4.5: Optical micro-graph of successfully fabricated bridge corresponding to C = 3.0.

C 1.3 could not be used as none of them survived fabrication due to high point strain concentrations.

The peak shift and peak width were extracted from the μ-Raman curves and plotted in Figure 4.6(b). Raman shift decreases with increasing C that corresponds to decreasing strain as predicted due to lower pad size. The peak width remains relatively unchanged indicating that no substantial degradation of the crystalline quality has occurred. Figure 6(c) shows the measured strain values extracted from the peak shifts [68] using a proportionality factor of 390 cm^1 in addition to the corresponding simulated values, both show a trend of decreasing strain as C increases. The discrepancy between the simulated and measured values are likely due to an two dimensional isotropic etching profile being assumed during simulations whereas the fabricated devices have a more complex three dimensional anisotropic etching profile, however the strain distribution should not be effected by the anisotropic etching profile as the symmetry is the same.

4.2.3   Micro-photoluminescence (μ-PL) measurements

μ-PL measurements were conducted on the same bridges as studied by μ-Raman spectroscopy. A green laser with a 532 nm wavelength was used to excite the central region of the bridges with a power of 1.8 mW in conjunction with a 100-x lens resulting in a spot
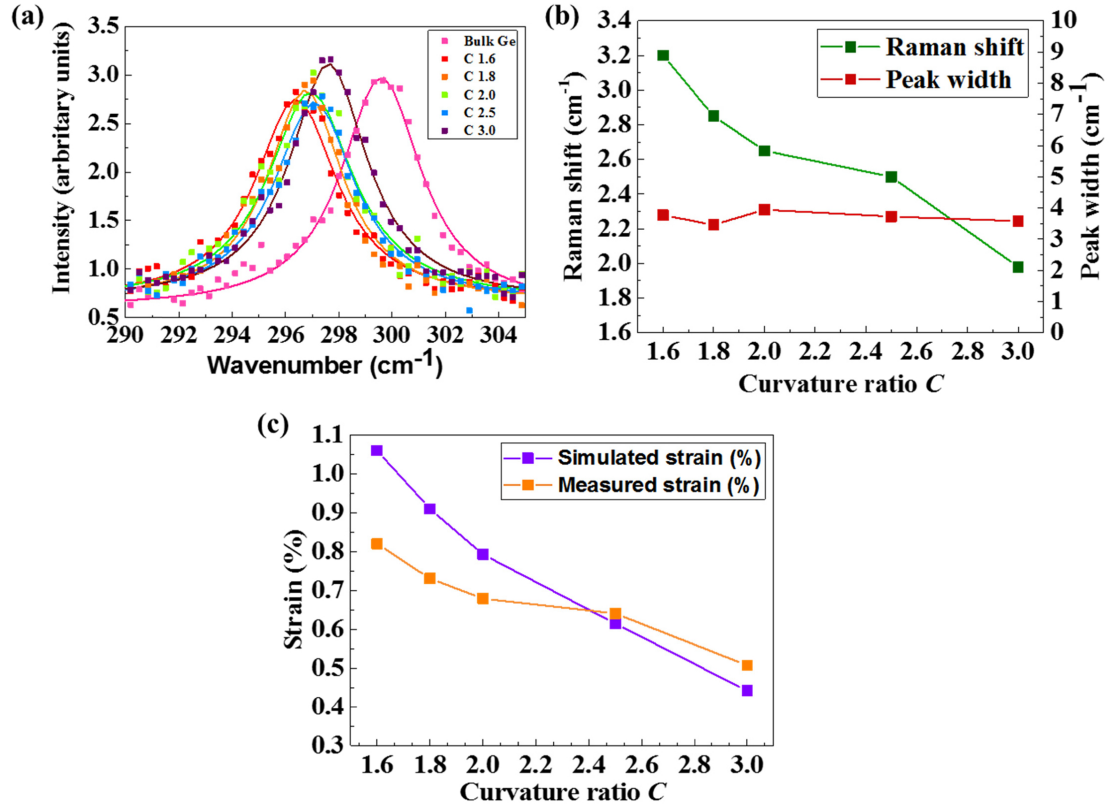
FIGURE 4.6: Optical micro-graph of successful fabricated bridge corresponding to C = 3.0.

size of around 1 μm diameter at room temperature. Figure 4.7 shows the μ-PL spectra of bridges with increasing C as well as bulk Ge as a reference. In general, complex spectra were produced with a broad emission profile; the spectra have been red-shifted from the bulk Ge direct band-gap (corresponding to 1550 nm) due to the strain induced band-gap reduction. The compressive strain fields in the pads cause the direct band-gap to increase in size and is likely the cause of the significant μ-PL intensity below 1550 nm in the spectra. Furthermore, two distinct peaks appear in each spectra can be visualized likely due to Light Hole (LH) and Heavy Hole (HH) valence band splitting. Small Q factor modes can also be seen in some bridges with the sharpest being in C = 3.0 likely originating from the longitudinal thickness of the Ge bridge. It is difficult to ascertain where the μ-PL signal is coming from in the bridge using only a one-dimensional detector array, the spectra becomes complex due to central and maximum strain values as well as the subsequent LH and HH splitting, further work will be required to decouple these phenomena and locate the source of the μ-PL signal.

As C increases the intensity increases across the spectrum despite the strain decreasing. The intensity of the bridge with C = 3.0 corresponding to a central strain of 0.52% has an enhancement of 3x relative to C = 1.6 at 1650nm. Thermal effects are an important issue in suspended bridges, as there is air either side of the bridges thickness, the heat cannot dissipate and the temperature of the bridges rise. The increase in temperature
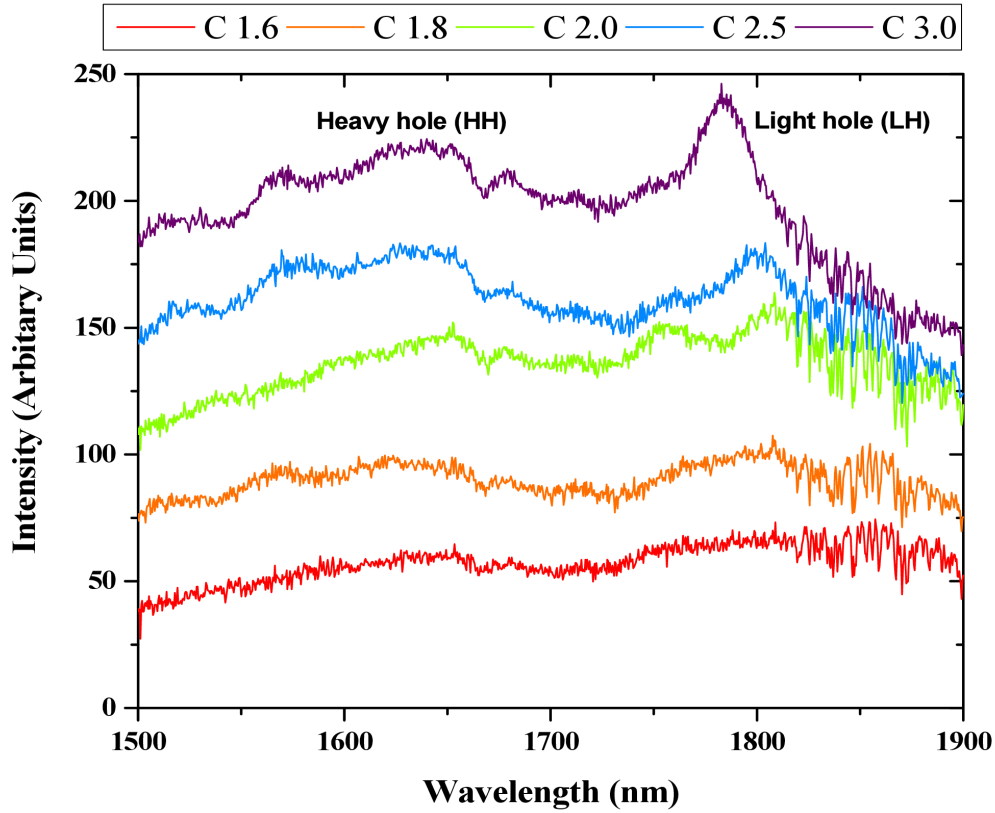
FIGURE 4.7: μ-PL spectra of bridges at increasing C. A cumulative y-offset of 25 was added to enable clear visualization of the spectra without overlap.

results in more indirect transitions and therefore enhanced μ-PL signal as well as red shifting. However the heat dissipation in these bridges should be extremely similar due to similar lateral air gaps and therefore the thermal contribution cannot explain the enhanced μ-PL intensity. One explanation for this enhancement could be due to dislocation formation at the low C bridges due to higher strains; however, this is unlikely, as the peak width in the μ-Raman spectra, Figure 4.6(b) remains relatively constant. Sukdeo et al reported a 2.4x μ-PL enhancement in their biaxial suspended bridges [34] however, they had expected a 20x enhancement compared to bulk Germanium from theoretical calculations. One explanation provided for this discrepancy was pseudo-heterojunction carrier confinement effects occurring in the point strain concentrations in the corner of their bridges (which were similar to low C bridges). If the carriers were to recombine here, the emission could be redshifted past the detector limit and therefore not contribute to μ-PL intensity. Another explanation for improved μ-PL intensity at higher C could be due to a combination of carrier diffusion and surface recombination. In lower C bridges the point stress accumulation occurs at the dry etched interface. If carriers diffuse towards this region with lower band-gap, they could scatter or undergo non-radiative surface recombination both of which act as a potential loss mechanism. In higher C bridges the maximum strain is further away and is not solely concentrated

at the interface reducing these potential losses. Further work is required to deduce the exact carrier behavior responsible for this μ-PL enhancement.

4.2.4   Conclusion

By optimizing curvature and using FEM, bridges with improved homogeneity were identified and improved light emission was confirmed by μ-PL studies. Bridges with a high curvature (low C) exhibited large corner strain values, which were not present in the lower curvature (high C) bridges. The lower curvature bridges therefore had improved homogeneity, which was reflected in an enhanced μ-PL intensity in these bridges despite lower central strain values. This study provides further evidence that high point strain values can be detrimental to both the mechanical and optical properties of biaxially suspended Ge bridges. This further highlights the need to consider the entire strain distribution when attempting to enhance light emission in Ge rather than absolute strain values. This geometric methodology can be applied to other strain platforms in Ge to enhance light emission not just suspended bridges. Further work is required to understand the exact nature of the carrier dynamics responsible for enhanced light emission with improved homogeneity. A 3-x intensity enhancement from C = 1.6 to C = 3.0 was confirmed. With improved homogeneity, biaxially suspended Ge bridges become a more viable option as practical on chip light source.

Chapter 5

Optical cavity integration and reduced corner stresses in Germanium polyaxial suspended bridges by utilising an elliptical design

5.1   Introduction

In chapter 3, Finite Element Modelling (FEM) and micro-Raman (μ-Raman) spectroscopy was utilised to compare the mechanical stress and thermal management in uniaxial and polyaxial bridges. It was shown that uniaxial bridges posses much lower corner stresses and therefore higher practical values can be achieved compared to polyaxial bridges. However it was also shown that polyaxial bridges have superior thermal management compared to their uniaxial counterparts. With the improved thermal management and recent studies showing that 3x more uniaxial strain is required to convert Ge into a direct band gap material, it was argued that polyaxial bridges hold some advantages over their uniaxial counterparts warranting further investigation.

Chapter 4 highlighted the need to minimise the corner stresses to reduce negative psuedo-heterojunction effects and prevent mechanical failure. However the design in chapter 4 was too complex and the strain achieved was still low.

For successful integration of polyaxial bridges two challenges must be addressed:

1. Integration of an optical cavity whilst maintaining good thermal management

54

Chapter 5 Optical cavity integration and reduced corner stresses in Germanium polyaxial suspended bridges by utilising an elliptical design

2. Reduction, or preferably elimination, of corner stresses to enable higher biaxial strain values to be achieved

Despite 1.9% biaxial strain being demonstrated in suspended Ge bridges [100], there has only been once concerted effort to integrate an optical cavity from a polyaxial bridge [34]. Sukhdeo *et al* created a polyaxial bridge, the design of the polyaxial bridges in chapter 3 were based on this design. In their study they showed that the polyaxial bridges strain profile drastically increased in homogeneity as the number of etch windows (or arms) increased, however this effect saturated at around 12 etch windows.

To introduce an optical cavity into these polyaxial bridges, Sukhdeo *et al* [99] deposited a compressively stressed Si_3N_4 layer onto polyaxial bridges which had adhered to the underlying BOX layer followed by partially etching away the pads to form a microdisk resonator. By etching away some of the Ge pads, a lateral refractive index contrast is generated and WGM can be introduced. The Si_3N_4 layer was a preventative measure to prevent strain relaxation at the top of the Ge layer after partially etching the pads. μ-Raman spectroscopy and FEM confirmed that the Si_3N_4 layer had prevented strain relaxation at the top of the Ge layer however some strain relaxation had occurred at the circumference of the microdisk resonator. Optical studies in the form of micro-PhotoLuminesence (μ-PL) and Finite Difference Time Domain (FDTD) simulations confirmed the presence of WGM in the microdisk resonators. The authors state that the resonant peaks were not very sharp likely due to the roughness of the Si_3N_4 and also radiation losses in the small microdisks. It should also be noted that by etching the arms, the lateral thermal dissipation paths are removed making the Ge much more thermally sensitive.

In this chapter we introduce a new polyaxial bridge based on an elliptical design which allows the integration of an optical cavity. Furthermore the new design offers many other advantages including: reduced corner stresses, reduced fabrication complexity, eliminate the need for Si_3N_4 and conservation of the thermal management properties.

5.2   Design

In this section we present the elliptical design used for the polyaxial bridges. The main premise is that by increasing the number of etch windows (or arms) WGM can be introduced without having to partially etch away the arms. This prevents destroying the lateral thermal conduction paths and therefore conserves the thermal management of the polyaxial bridges. Furthermore the process only requires one lithography step and no Si_3N_4 deposition therefore simplifying the fabrication process. By increasing the number of etch windows at a fixed diameter (and therefore fixed circumference) there is a greater amount of air at the circumference than Ge. The design used in chapter 3 and

also by Sukhdeo *et al* [34] utilised classic circular etch window, created by two circles and a rectangle for each etch window. Figure 5.1 shows the classic polyaxial design used in chapter 3, with the pad length, etch window thickness and central diameter.
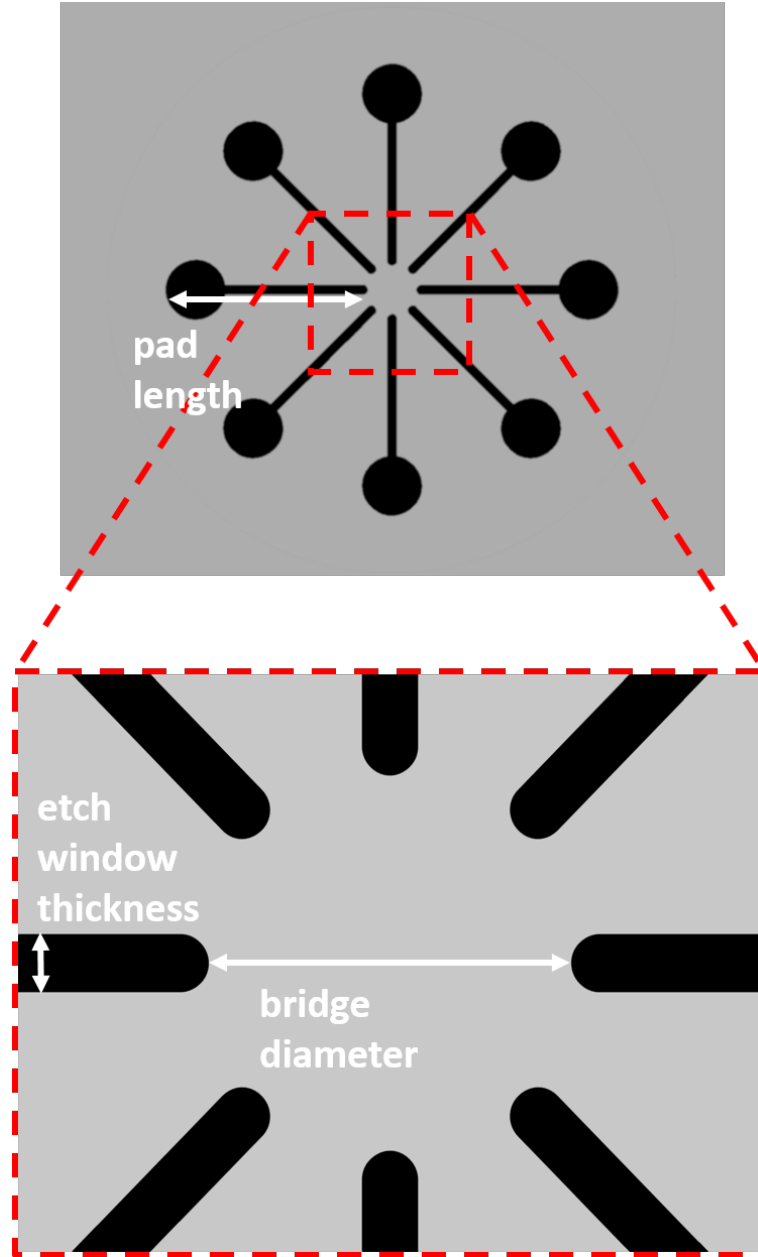
FIGURE 5.1: Design schematic the polyaxial bridge introduce in last chapter with the main design parameters shown: pad length, bridge diameter and etch window thickness.

The concern for using circular etching windows is that for a fixed diameter if you add more etch windows, eventually the maximum stress/strain will accumulate in the narrow regions between the arms. This will cause mechanical failure, in the form of fracturing, of the bridge before the WGM can be introduced. The WGM could be introduced by decreasing the pad length to reduce the stress, however this is not an option as it would drastically reduce the avaliable tensile strain required for band-gap engineering. Point stresses are a common issue in the field of mechanical engineering, one common tactic

utilised to reduce these point stresses is by using elliptical holes over circular holes [107]. Figure 5.2 shows the previous circular design being modified into an elliptical design, an Ellipse Ratio (ER) is defined which is the ratio between the b-axis and a-axis of the ellipse. Three exemplar designs with 24 arms and a central diameter of 3 μm is shown with an ER of 1.0, 1.5 and 2.0 in Figure 5.2.
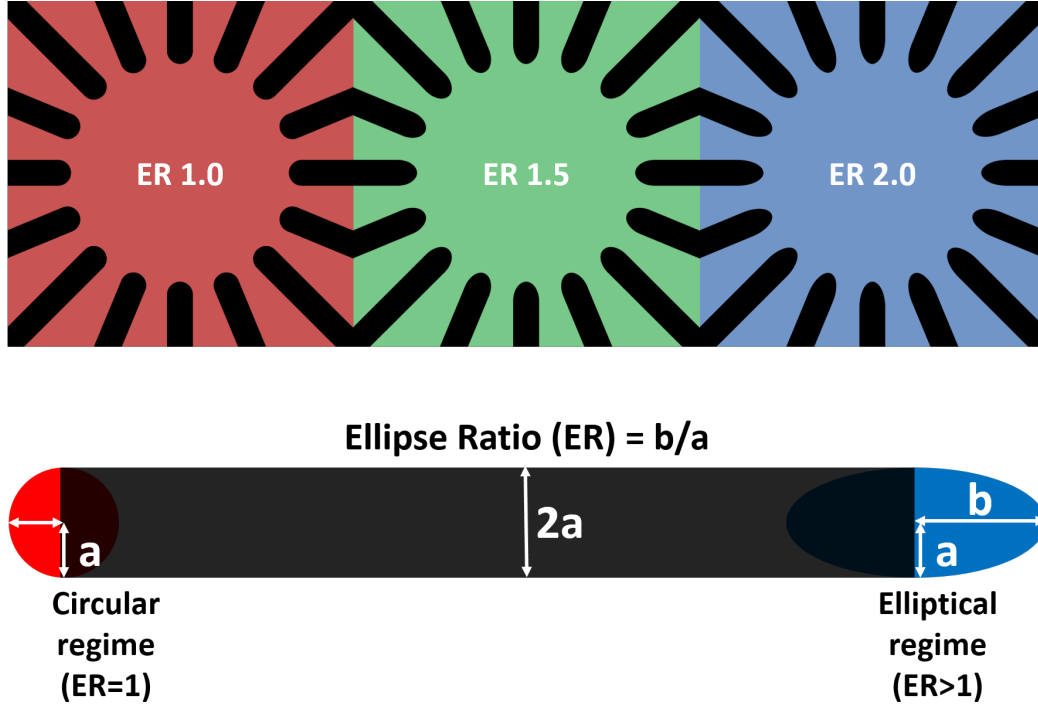
FIGURE 5.2: Schematic showing the elliptical etch window design with increasing ER values of 1.0 in red, 1.5 in green and 2.0 in blue. The ER is also defined in terms of the semi-axes of the ellipses in the etch window with two regimes: circular and elliptical.

5.3 Fabrication

Figure 5.3 shows the main fabrication steps to produce the suspended bridges. A chip with dimensions of 1 cm by 1 cm, originally diced from an 8 inch Ge on Si, wafer was proceed. The advantage of using a thicker Ge layer of 500 nm and the Si handle as the sacrificial layer, is the reduced capillary forces on the bridge during the drying step ensuring suspension and reducing the chance of fracturing. The chips were first cleaned to remove any organic contaminants from the surface using N-Methyl-2-pyrrolidone (NMP) under sonication followed by rinsing with Iso-Propyl Alcohol (IPA). This was followed by the spin-coating of the electronic resist ZEP520A. Patterning by Electron Beam Lithograpgy (EBL) was then used to define the etching windows (and therefore the bridges). After development the chips underwent Inductively Coupled Plasma (ICP) dry etching using CHF_3 and SF_6 chemistry removing 500 nm of Ge and exposing the underlying Si, thus forming the etch windows. The remaining resist was

then removed using elevated temperature NMP followed by IPA. The chip was placed into TMAH to selectivity etch the sacrificial Si layer, the target etch distance was 12.5 μm to fully release and suspend the Ge bridges. After the etching step the chip was rinsed in DeIonised (DI) water and dried using a nitrogen gun.
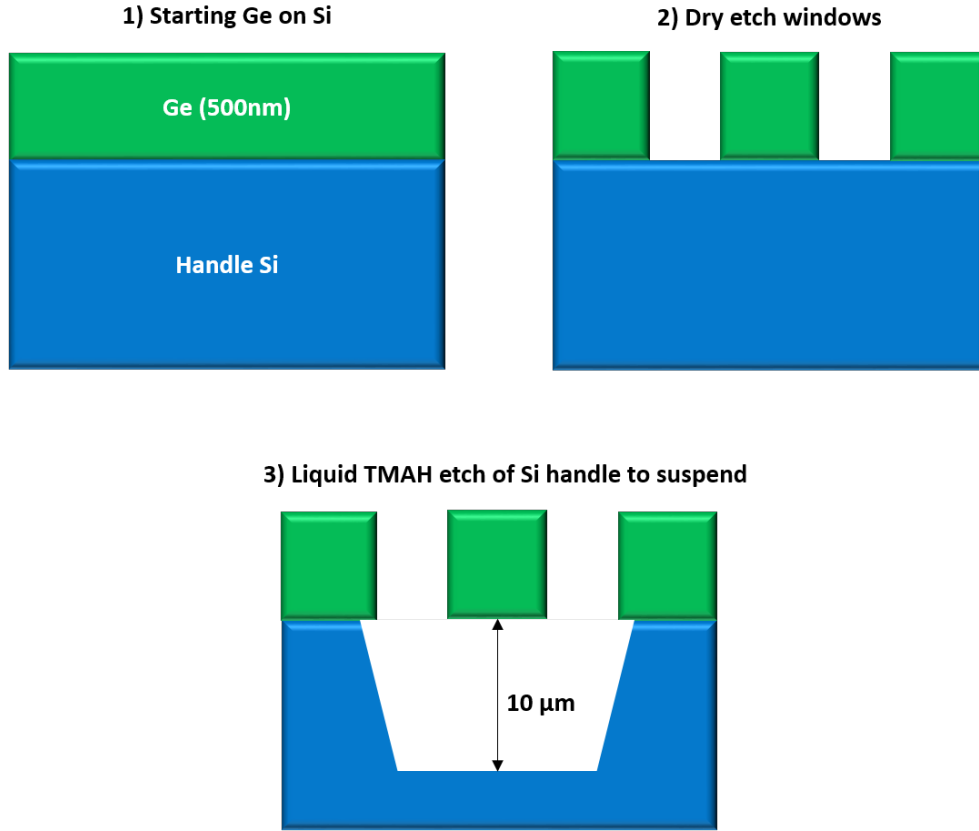
FIGURE 5.3: The main fabrication steps involved in producing the polyaxial bridges.

Figure 5.4(a) shows an SEM image of an exemplar fabricated polyaxial bridge with a 3 μ diameter, 16 arms and ER of 1.5. Figure 5.4(b) shows the same structure, with half the structure milled using a Focused Ion Beam (FIB) to confirm that the structure has been suspended. It can be visibly seen that the gap underneath the bridge is large, which is estimated to be around 10 μm, which is more than sufficient for optical confinement. The anisotropic etching of the Si can be visualised with the $\langle 111 \rangle$ planes visible. Future work should be conducted on a larger number of samples to see the influence of variations between devices with identical designs to ensure good reproducibility."

5.4 Stress and strain analysis

As mentioned in the introduction, the aim of the design is to increase the number of arms to introduce an optical cavity. However as the number of arms increases for a fixed diameter, the distance between the arms reduces and the maximum stress will eventually occur in these narrow regions causing fracturing.
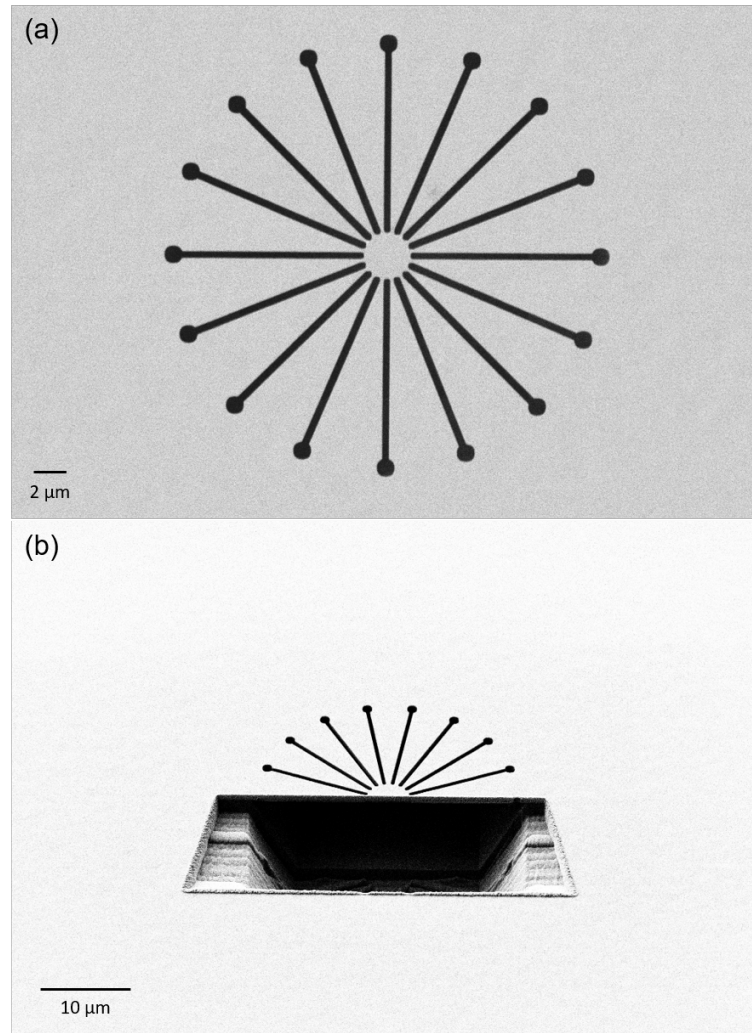
FIGURE 5.4: FIB/SEM images of sucesfully fabricated bridges.(a) A top-down perspective SEM image (b) A trench milled using a FIB into the Ge to show the successful suspension of the bridge.

This fracturing can be visualized in Figure 5.5, which shows the SEM images of three bridges with almost identical geometrical parameters. The pad length for each bridge is 50 μm and the central diameter is 3 μm, however each bridge has a different ER. This is important to note as each bridge should have the same amount of stress in the central region. Figure 5.5(a) has an ER of 1.0, a clear fracture can be seen (marked with a red circle) between the narrow region between two adjacent etch windows. Figure 5.5(b) and Figure 5.5(c) have an ER of 1.5 and 2.0, both of the bridges with an ER greater than unity have survived. This provides visual evidence that using an elliptical design prevents fracturing.

To gain a deeper understanding, FEM was used to study the influence of the ER on the stress and strain in the bridges. COMSOL Multiphysics 5.3a was used with the 'Structural Mechanics' module to study the stress and strain in in the polyaxial bridges. A 2D model was created with the bridge geometries. A fixed boundary was applied along
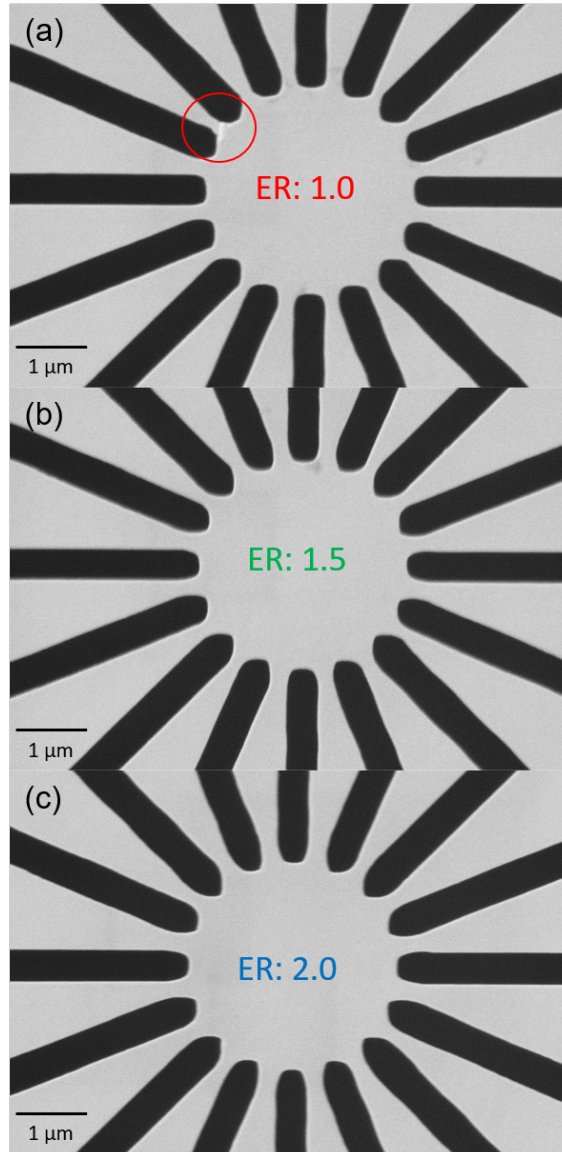
FIGURE 5.5: Top-down SEM images showing near identical bridges with ERs of (a) 1.0, (b) 1.5 and (c) 2.0.

the undercut boundary (i.e. where the suspension ends) assuming a 10 μm maximum under etch distance.

Figure 5.6 shows the strain profiles of each of the bridges shown in Figure 5.5 and also shows the relationship between the ER and both the central and maximum strain in the bridges.It should be noted the scales on the sub-figures differ to help visualise maximum strain. Figure 5.6(a) shows the strain profile of the bridge in Figure 5.5(a) which has an ER of 1.0, the maximum strain of 1.66% is located in-between the etch windows. Figure 5.6(b) shows the strain profile of the bridge in Figure 5.5(b) which has an ER of 1.5, the maximum strain is now mostly located at the tip of the etch window. The maximum strain has decreased from 1.66% to 1.39%, this is a 19.4% decrease in the maximum strain. Figure 5.6(c) shows the strain profile of the bridge in Figure 5.5(c) which has an

ER of 2.0, the maximum strain is now completely located at the tip of the etch window. The maximum strain at ER 2.0 has increased slightly to 1.4% but is still lower than the original circular design. Figure 5.6(d) shows the influence of the ER from 1.0 to 3.0 in 0.1 increments on the central and maximum strain. The ER has a negligible influence on the central strain value, however it has a big impact on the maximum strain value. As the ER increases from unity the maximum strain drops to a minimum of 0.77% at an ER of 1.8. As the ER increases further the maximum strain increases again, this is due to sharper corners. However the maximum strain still remains smaller than the original circular structure with an ER of 1.0. Therefore the elliptical design reduces the maximum strain and changes the location of the maximum strain from in-between the etch windows into the central region of the bridge. It should be noted that the maximum strain values at the corners are not purely biaxial due to asymmetric strain components, this can result in larger stresses due to shearing and therefore it is prudent to run stress analysis as well.

Figure 5.7 shows the Von Mises stress profiles for the bridges shown in Figure 5.5, it should be noted the scales on the sub-figures differ to help visualise maximum stress. Figure 5.7(a) shows the Von Mises stress profile of the bridge in Figure 5.5(a) which has an ER of 1.0, the stress is mostly located again between the etch windows. Figure 5.7(b) shows the strain profile of the bridge in Figure 5.5(b) which has an ER of 1.0, the stress is located between the arms, however the magnitude of the stress has dropped. Figure 5.7(c) shows the stress profile of the bridge in Figure 5.5(c) which has an ER of 2.0, the stress is now moving towards the central region of the bridge. Figure 5.6(d) shows the influence of the ER on the Von Mises Ratio (VMR)(defined in the chapter 3). Similar to the results of Figure 5.6 the VMR is lowest at an ER of 1.6. The VMR is 20% lower than the best circular designs presented in chapter 3. This means that by employing an elliptical design, the largest achievable strain can be increased by up to 20% and even further potentially with optimization.

Raman spectroscopy was used to determine the highest strain experimentally. A continuous wave green laser with a wavelength of 514 nm was used to excite the bridges. A 50x objective lens was used to focus the laser spot onto the central area of the bridge resulting in a spot diameter of around 1.0 μm. The signal was collected using the same objective lens and reflected into a high resolution grating of 3000 lines/mm. The exposure time was set to 10 s and the spectra were averaged 12 times for a total measurement time of 120 s per bridge. The Raman spectra were fitted with Lorentzian functions in order to estimate the peak position.

For measuring the strain, an optical power of 46 μW was used after testing the power dependency and showing negligible heating effects (which cause an error in the strain measurement). Shifts in Raman peak position relative to a bulk Ge sample ($\Delta\omega$) were deduced allowing the strain (ϵ) to be calculated using the equation: $\epsilon = \Delta\omega$ x C. Where C is a proportionality factor reported in literature to be 390 cm^{-1} [68] for biaxial strain.
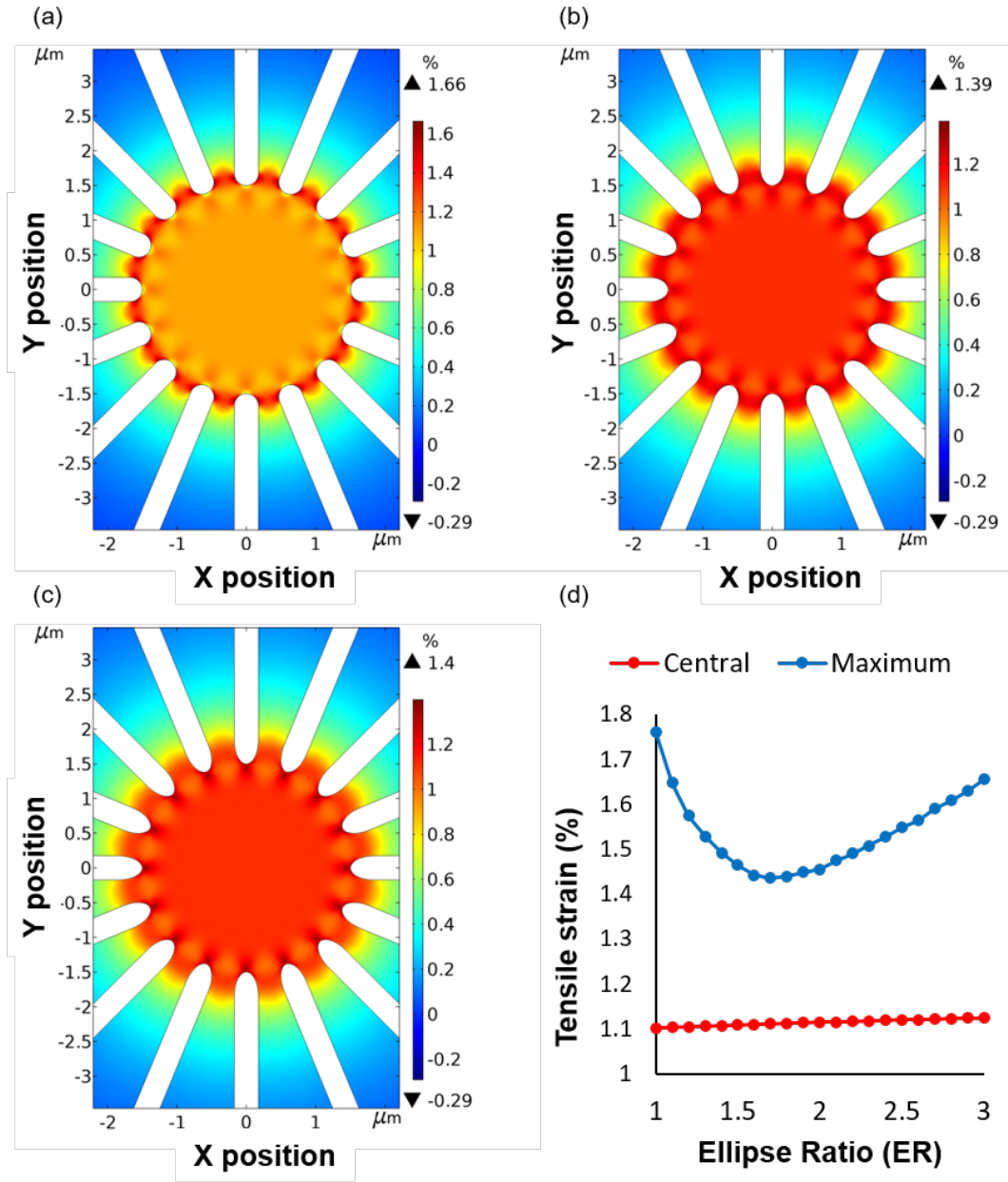
FIGURE 5.6: Tensile strain distribution at (a) ER 1.0 (b) ER 1.5 and (c) ER 2.0. The infleunces of ER on the central and maximum tensile strain.

Figure 5.8 shows the Raman spectra of bulk Ge, the epitaxial Ge on Si and the bridge with the highest strain. The bridge with the highest strain has a central diameter of 3 μm, 16 arms and an ER of 1.5, however there were many other samples with similar strain values. The amount of strain was 1.11% which is nearly 50% larger than demonstrated in chapter 3.
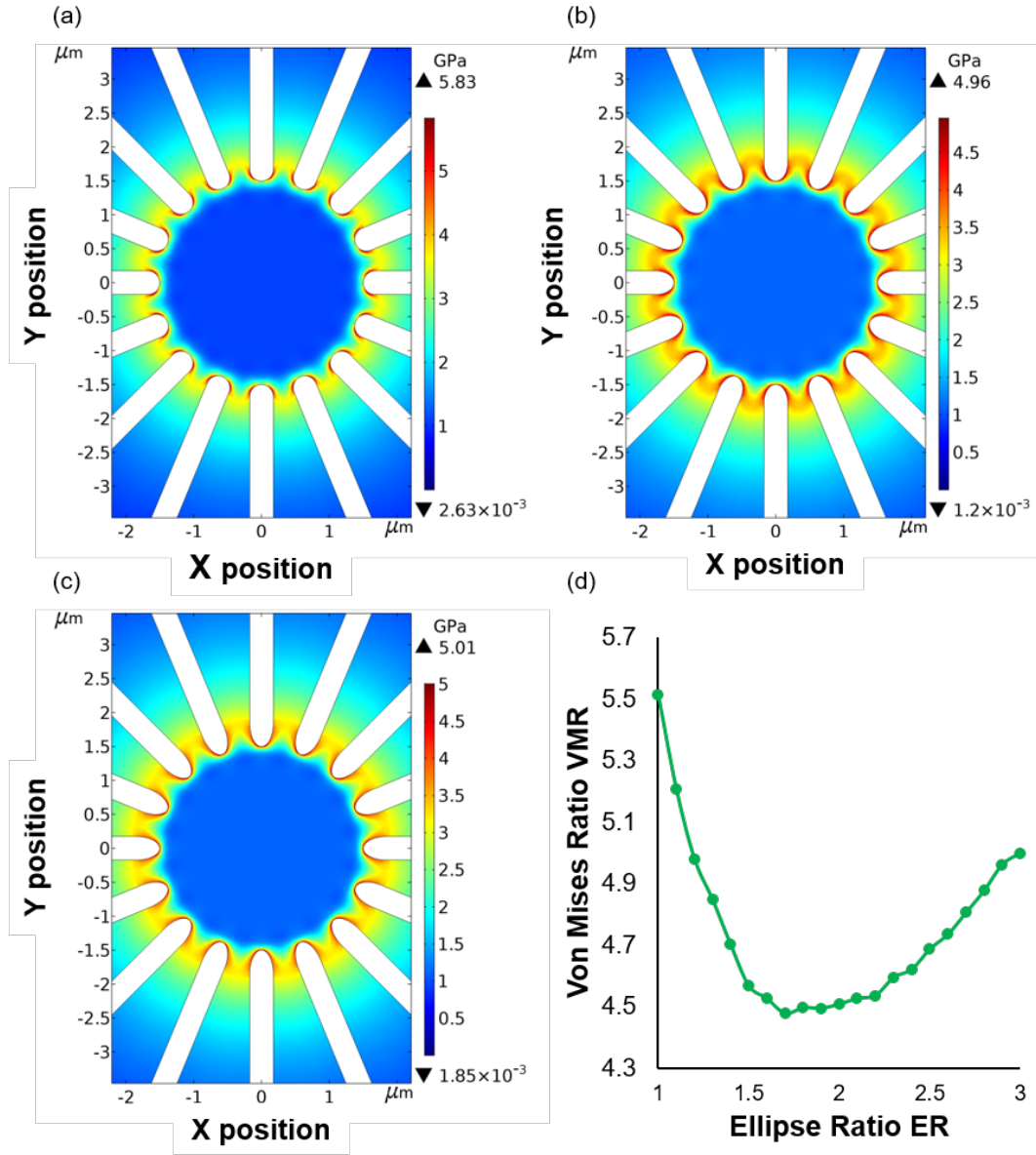
FIGURE 5.7: Von Mises stress distribution at (a) ER 1.0 (b) ER 1.5 and (c) ER 2.0. The infleunces of ER on the Von Mises Ratio (VMR).

5.5   micro-PhotoLuminesence (μ-PL)

5.5.1   Experimental details

To study whether an optical cavity was introduced μ-PL measurements were conducted at low temperature (4K). A laser diode under pulsed operation was utilised. pump wavelength of 1064 nm was used in conjunction with. A 20x objective lens to focus the laser spot to roughly 20 μm, this spot size was larger than the central bridge reason with the implication that the pads (i.e. relaxed) Ge was also excited. For each measurement the pulse width was 20 ns and the frequency was 10 MHz, pulsed operation was utilised to minimise heating effects. The excited light was collected through the same objective
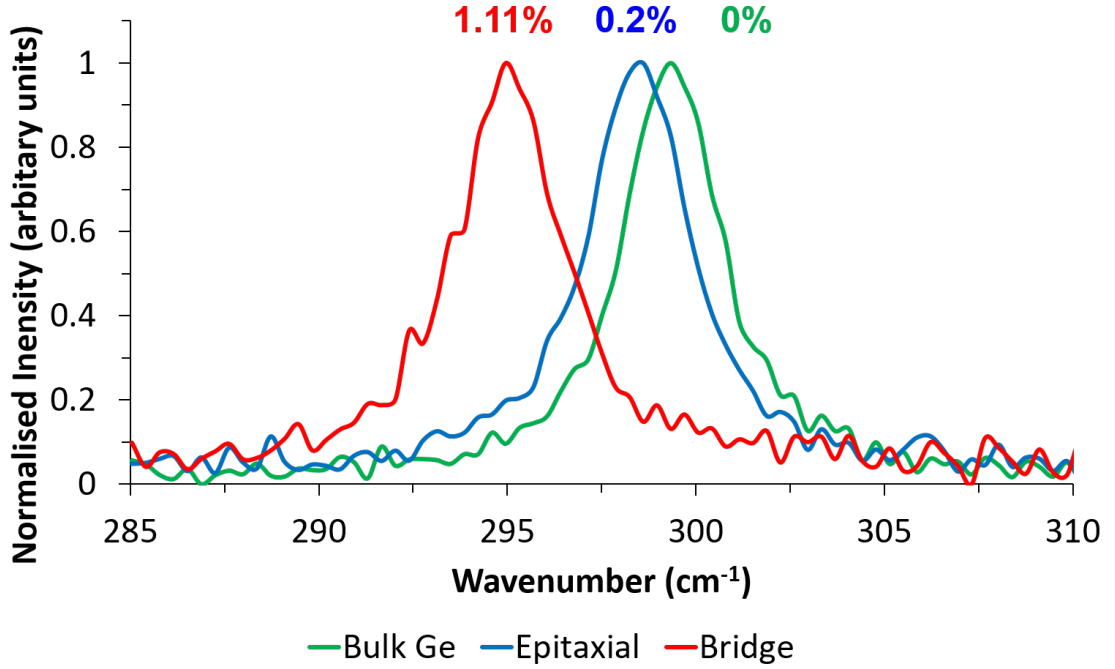
FIGURE 5.8: Raman spectra of the highest strained bridge with bulk Ge and epitaxial Ge on Si for reference.

lens used for excitation and coupled into an InGaAs detector with a cut off at around 1650 nm. For each spectra the exposure time was set to 0.5 s and 30 exposures were averaged to provide the final spectrum. Due to the cut off limitation of the detector, highly strained samples were not possible to measure with this experimental set up. However bridges with minimal strain are sufficient to demonstrate optical modes.

5.5.2 Power dependency

Figure 5.9 shows the μ-PL spectra of a bridge with a 4.5 μm central diameter, 16 arms, 12.5 μm pad length, and an ER of 1.5. The strain in the central part of the bridge is comparable to the epitaxial value of 0.25% at room temperature according to FEM. As the bridge is suspended and cooled the strain can be enhanced [33], although this effect is likely negligible due such small pad length to with pump powers of 1.0, 2.0, 3.0 and 4.0 mW. For all pump powers there is a broad peak centred at a wavelength of around 1485 nm which is which is likely due to the Γ to HH transitions. There is a smaller less broad peak at around 1575 nm and also a broad peak between 1600 nm and 1650 nm. It is hard to determine the exact cause of these peaks but they are likely due to contributions from the indirect transitions and the Γ to LH transitions. As the power increases the intensity of the peaks increase as a result of enhanced spontaneous emission. There is no red-shifting of the peaks with higher pump powers indicating that no significant heating effects are occurring.
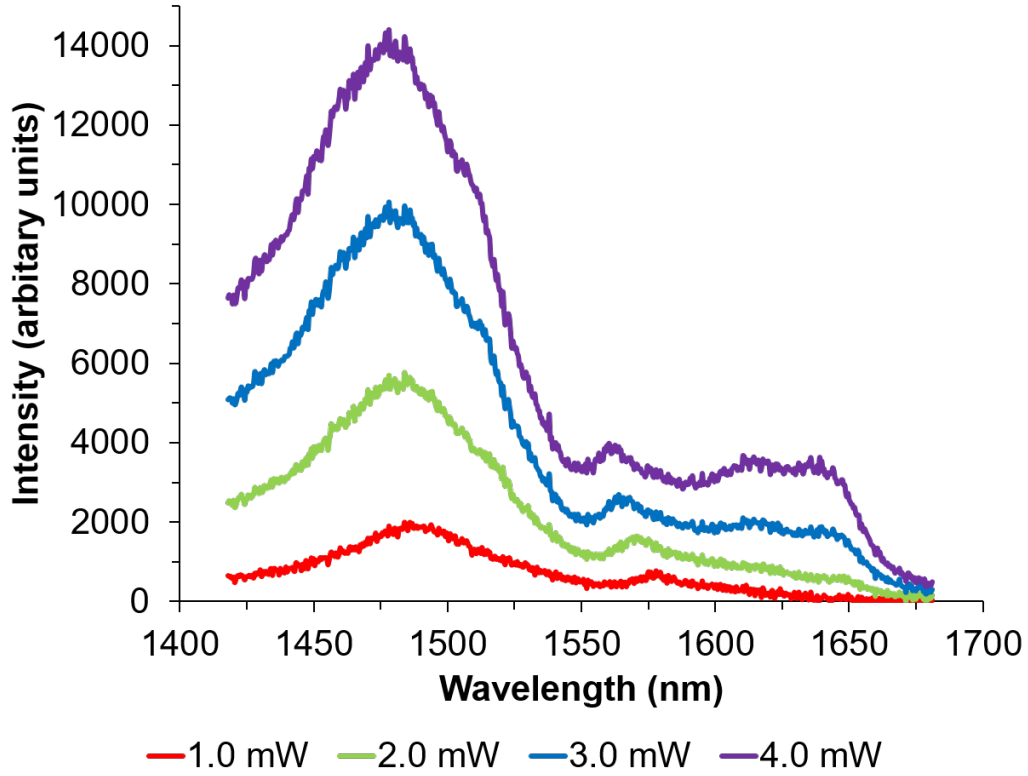
FIGURE 5.9: Power dependency μ-PL measurements

5.5.3   Optical modes

Figure 5.10(a) shows the μ-PL spectra for the bridge that underwent the power dependency in the previous sub section and also an near identical bridge which has 24 arms instead of 16 arms under 4.0 mW pump power. Therefore the strain in these bridges is near identical as confirmed with FEM. The bridge with 16 arm has no clear resonances present in the spectrum, however the bridge with 24 arms has multiple resonances indicating the presence of multiple optical modes. Transverse optical modes can be ruled out as both bridges have the same Ge thickness. Figure 5.10(b) and Figure 5.10(c) shows FDTD simulations for the bridges with 16 and 24 arms respectively at 1550 nm. The simulations reveal WGM are present in the 24 arm bridge which are not present in the 16 arm bridge thus confirming that the larger number of arms allows for the introduction of WGM. The WGM are not extremely well defined which is likely indicative of a leaky mode. The measured Q-factor of the sharpest mode which was centered at 1547.77 nm is 310. There are other peaks located at 1516 nm and 1531 nm which are likely due to different order WGM, future studies will fully study and optimize these modes.

(a)

(b)

(c)
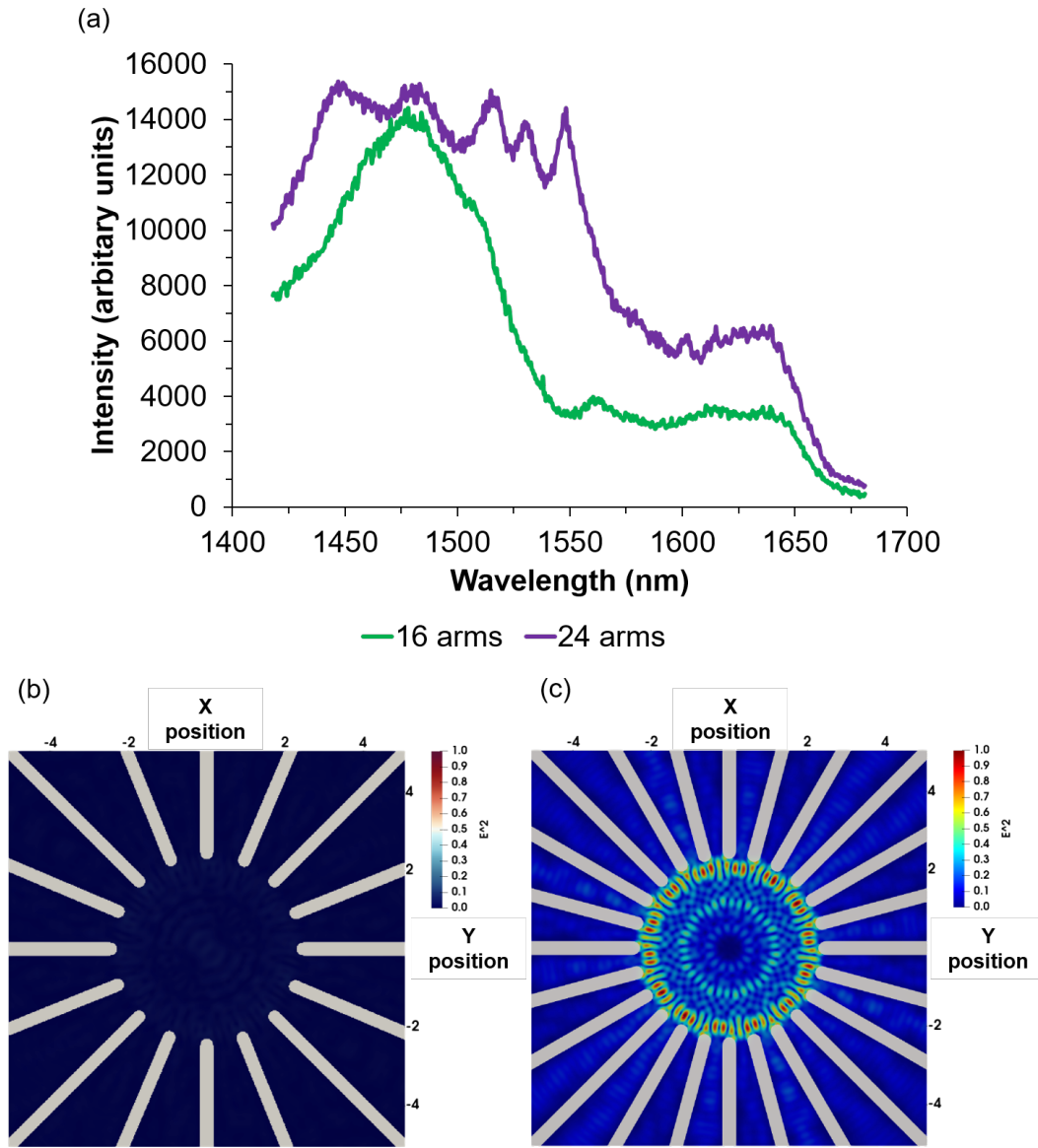
FIGURE 5.10: (a)μ-PL spectra of bridges with 16 and 24 arms. (b)Normalised optical field profile from FDTD at 16 arms at 1550 nm wavelength. (c)Normalised Optical field profile from FDTD at 24 arms at 1550 nm wavelength.

5.6   Discussion

The Ge used in this study was thicker than in the previous study, this means that a larger number of dislocations should be present in the bridge and mechanical failure should occur more easily. However the introduction of the ER enabled higher strain to be achieved in the polyaxial bridges. There was a remarkable 50% increase compared to the biaxial strain reported in chapter 3 and chapter 4. FEM modelling only accounts for around 20% of this strain increase due to a reduction in the VMR, the reason for such an improved strain value is unclear at this time. However it is clear that the elliptical designs can achieve higher strain values then their circular counterparts by reducing corner stresses. Despite this improvement, the VMR is still much higher than uniaxial

bridges. Perhaps this offers a unique opportunity to further improve the design to reduce the VMR for polyaxial bridges and further enhance the biaxial strain. As mentioned extensively the previous chapters, 3 times less biaxial strain is required to convert Ge into a direct band-gap material. Therefore if the VMR could be further improved by new designs then an optimal band-gap configuration can be achieved for lasing.

By using a larger number of arms, WGM can be introduced into these polyaxial bridges. This is achieved without destroying the precious lateral thermal conduction paths and therefore maintaining the thermal management, this is evidenced by the power dependencies which show no red shifting at 4K. As the temperature increases however the thermal conductivity of Ge can drop substantially and at higher pump powers heating will still likely occur. Furthermore no deposition of Si_3N_4 is required [99] and no strain relaxation at the edges occurs. Strains of up to 1.11% were obtained which is comparable to the microdisks presented in Sukhdeo *et al*, these microdisks had higher quality GOI and thinner layers. Therefore if the elliptical designs are combined with higher quality GOI and thinner Ge layers, then even high strain can be achieved.

Compared to the biaxial bridges in chapter 4, which had a maximum tensile strain of 0.8% strain, the polyaxial bridges presented in this chapter exhibited a 26.1% percentage increase in tensile strain. Both the starting material and the fabrication process were identical for the biaxial and polyaxial bridges. Therefore the strain improvement is a merit of improved design. Furthermore, WGMs were present in the μ-PL spectra of Figure 5.9; however, no distinct cavity modes were observed for the biaxial bridges, showing the distinct advantage of the polyaxial bridges for optical cavity integration. It should be noted that in addition to these advantages, the design presented in this chapter was greatly simplified, making practical realization much easier.

Due to limitations of the experimental set up, the optical properties of only low strain structures were measured at low temperature. However many structures with larger numbers of arms and high strain were fabricated, future work can address measuring the longer wavelength emission from these structures.

The strain and optical confinement can also be optimised somewhat independently. The resonant wavelength for the WGM can be controlled by the central diameter and the strain (and therefore emission wavelength) can be tuned by adjusting the pad length. The ER and number of arms can then be optimised to maximise the Q factor whilst minimising the corner stress. The Q factors reported so far were quite low, future work can also address increasing the Q factor by optimising the diameter and the number of arms. To achieve room temperature Ge, higher strain must be achieved (around 2%) and also better thermal management. By combining the dual insulator GOI platform with elliptical designs potentially both of these can be achieved.

5.7   Conclusions

In this chapter we presented a novel elliptical polyaxial suspended Ge bridge design. The design was successfully fabricated on a Ge on Si platform. SEM, FEM and μ-Raman were utilised to confirm the reduced corner stress in this design allowing for higher strain values to be achieved of 1.11% compared to previous designs. An optical cavity was confirmed with WGM identified using FDTD and μ-PL. This elliptical design improved two major issues with polyaxial bridges: high corner stress and optical cavity integration with good thermal management.

Chapter 6

Conclusions and future work

Finally the thesis is concluded with a summary and conclusion of the research followed by future work and outlooks.

6.1 Summary

To summarise, this thesis identified advantages in terms of thermal management for polyaxial bridges over uniaxial bridges. Furthermore novel designs were explored which improved the current state of the art biaxial and polyaxial bridges.

A summary with the contributions of this thesis can be summarised as follows:

1. In chapter 3, a study was conducted to compare uniaxial and polyaxial bridges in terms of thermal sensitivity and mechanical stress. This was achieved using Finite Element Modelling (FEM) and micro-Raman (μ-Raman) spectroscopy. It was shown that the corner stresses in polyaxial bridges were extremely large with values up to 5x larger than their uniaxial counterparts, which is the reason large amounts of mechanical failure occurred, this was supported by yield analysis. The implication of this is that uniaxial bridges are limited by material quality whereas polyaxial bridges are limited by design. Furthermore it was shown that polyaxial bridges were much less sensitive to heating under optical pumping therefore may be more suitable for higher temperature operation and more efficient lasing. It was postulated, in conjunction with recent theoretical and experimental evidence, that polyaxial bridges could be advantageous over uniaxial bridges.

2. In chapter 4, the role of curvature in biaxial suspended bridges was explored using FEM, μ-Raman and micro PL(μ-PL). It was shown that despite decreasing strain the PL intensity increased with decreasing curvature. Although it may be due to some heating effects this suggests the decrease in PL intensity is due to large

corner stresses causing un-favourable psuedo-heterojunction effects. Despite improvements these designs were not practical for a few reasons such as low achievable strain, no optical cavity and complex design.

3. In chapter 5, a novel elliptical etching window design was introduced to improve on the design outlined in chapter 4. This bridge design simultaneously allowed the integration of an optical cavity and reduced corner stresses. The elliptical design reduced corner stresses by around 20% allowing a high biaxial strain value of 1.11% despite the high number of dislocations in the Ge on Si stack. Furthermore using Finite Difference Time Domain (FDTD) and μ-PL it was shown that the by increasing the number of arms, WGM could be introduced.

The main take-way from this thesis is that despite being overlooked, polyaxial bridges offer many advantages over their uniaxial counterparts for a Ge laser. It has been show that corner stresses can be reduced by design and thermal management is superior in polyaxial bridges. Uniaxial bridges are currently limited by the material quality of the Ge. However for polyaxial bridges, if the corner stresses could be further reduced by design, then enough strain to enable efficient lasing (> 2%) could be achieved with efficient thermal management. Furthermore it must also be reminded that 3x less biaxial strain is required to convert Ge into a direct band-gap material further increasing the prospects of polyaxial bridges.

6.2   Future work

6.2.1   Improving the elliptical design

The immediate future work should focus on further studying and optimising the elliptical polyaxial bridges. More in-depth studies must be conducted to increase the Q-factor of the optical modes and decrease the corner stresses. This can be done by sweeping the Ellipse Ratio (ER) and central diameter more carefully. By increasing the diameter and tuning the number of arms the Q-factor of the WGM should be able to be increased.

6.2.2   Towards room temperature lasing

To move towards room temperature optically pumped lasing with the polyaxial bridges and the elliptical design, some requirements must be fulfilled. The material quality of the polyaxial bridges must be improved to obtain enough biaxial strain to not only convert Ge into a direct band-gap material, but to ensure a large enough gap between the Γ and L valley to allow for efficient lasing. Secondly better thermal management must be achieved, as the temperatures were reaching above 50 °C even at modest pumping.

Both of these issues can be addressed if the elliptical designs are fabricated on the GODI platform. The GODI platform uses wafer bonding and subsequent CMP to remove many of the misfit dislocations which accumulate at the interface between Ge and Si. Therefore as the misfit dislocation density is reduced, higher strain can be achieved. The maximum biaxial strain achieved on a GOI platform was 1.9% [100], the elliptical design may be able to push this high value past the point of direct band-gap and allow efficient lasing. Secondly as the polyaxial bridge comes into contact with the underlying SiO_2 combining efficient transverse and lateral thermal management, this makes them more suitable for high power detectors.

One last issue that must be addressed is characterisation, μ-PL measurements were limited in this study to low strain values due to red-shifting of the emission past the detection limit. Future work must use Fourier Transform Infrared detectors to push the detection limit into the MIR and measure the high strain samples, as conducted in [33].

6.2.3 Novel directions

Finally we end the discussion on future work with some suggestions of novel applications for polyaxial bridges.

The first potential application is in photodetectors, the polyaxial bridges can be arrayed into pixels. The wavelength of the light to be detected can be tuned by using strain, allowing for a wide range of detection efficiency on the same chip. Furthermore these bridges will posses better thermal management than any uniaxial counterparts allowing for reduced dark current during operation.

The second application is to apply these polyaxial bridges to GeSn. As mentioned in chapter 2, GeSn bridges suffer from large threshold, however they have more reproducible and higher temperature operation than Ge lasers. Recent theoretical studies suggested that combining Sn alloying and tensile strain together could be an efficient way to unlock efficient room temperature lasing [108]. This inspired a recent demonstration of lasing up to 273K [109] in strained GeSn using uniaxial bridges. The elliptical polyaxial bridge design could be applied to such a fabrication process allowing for a larger effects on the band-gap to be achieved, not only allowing more efficient operation but also red shifting into new MIR applications.

Appendix A

A.1 Optical pumping

Optical pumping is most often used to test for lasing in Germanium (Ge), this is due to more rapid fabrication and prototyping due to a lack of metal contact integration. As mentioned the local heating of devices under optical pumping can cause drastic temperature increases and therefore losses. Free Carrier Absorption (FCA) and Inter-Valence Band Absorption (IVBA) are the predominant loss mechanisms and both are proportional to temperature. To move toward room temperature lasing in Ge the effect of the various optical pumping parameters such as pump wavelength and optical power must be explored as well as the structural parameters of the platform. Furthermore, the models currently used must be improved to better understand the heating by considering how the incident pump power is dissipated and distributed in the Ge. This will allow the temperature increase to be put in terms of number of photons absorbed in the active region and also allow a better definition of the injection power. The goal of this study is to employ FEM to explore the effect of design and optical pumping parameters on the temperature distribution within the Ge in both un-patterned wafer stacks.

Pump wavelength can have a large impact on how the optical power distributes within the Ge and therefore influences the injection power and heating. The first consideration is that the pump wavelength must correspond to a higher energy than the band gap to allow excitation, for this purpose we will only consider pump wavelengths below 1550 nm although the Ge band-gap redshifts under tensile strain meaning higher pump wavelengths could be utilized.

A.2 Simulation details

A 2D axis-symmetric model was utilized in COMSOL Multiphysics v5.3, which was used to study the optical power distribution and subsequent temperature profiles. Two wafer stacks were studied: Ge on Si and and GOI ($Ge/SiO_2/Si$). Dispersion for the extinction coefficient and refractive index were inbuilt as look up functions[110]. The

input parameters were pump wavelength, incident pump power and layer thicknesses. Often in literature the calculated power density is simply the measured incident power divided by the area of the spot size neglecting non-uniformities. First we use the Fresnel equations to calculate the reflectance and transmission of the incident light into the Ge layer, then our simulation accounts for non-uniformities to provide a more accurate picture of the heating. The lateral non-uniformity was considered by implementing the 2D Gaussian profile of the beam at the surface. The transverse non-uniformity was considered by implementing the Beer-Lambert law. The optical power distribution was then used as a heat source in the 'Heat Transfer in Solids module'. The bottom of the wafer was fixed at T = 20ºC as a fixed boundary condition. Figure A.1 shows a schematic of how the optical power distribution is calculated and used as a heat source, under the assumption all power is converted to heat.
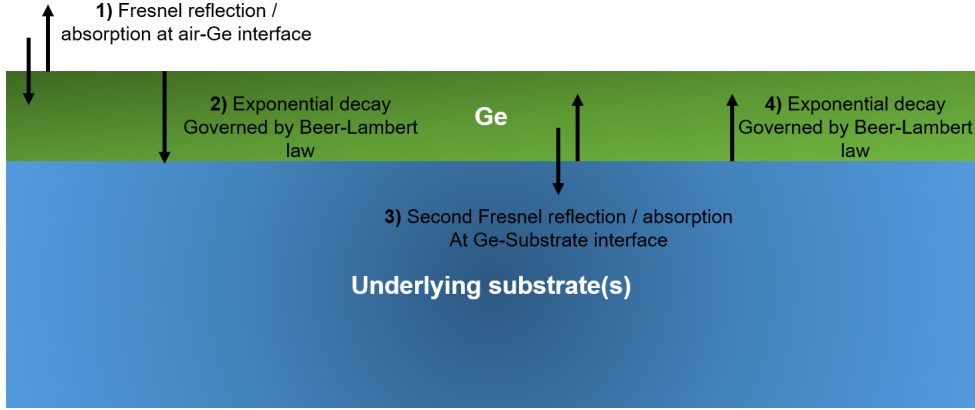
FIGURE A.1: Schematic diagram showing how the incident optical power is dissipated from the Fresnel equations and the Beer Lambert law at multiple interfaces allowing the absorbed optical power and thus heat to be calculated as a function of wavelength, thickness and wafer stack.

Optical confinement and injection densities must also be considered when selecting wafer stacks and layer thicknesses, but the thermal dissipation becomes retarded as the Ge layer thickness is reduced, this has drastic implications for nano-structures especially considering the thermal conductivity is drastically reduced in these structures further worsening the heating issues. If nano-structures are employed to reduce the threshold current they must be accompanied by strict thermal management methods.

A.3 Absorbance and number of photons absorbed

Firstly, pump wavelength influences the relative magnitude of absorption and reflection determined by the refractive index and governed by the Fresnel equations. Depending on the wavelength of the incident radiation up to 60% of the optical power can be reflected at the top interface and thus cannot be used for optical pumping. Secondly, the pump wavelength defines the extinction coefficient that determines the exponential decay of the

optical power governed by the Beer-Lambert law. Depending on the penetration depth (the distance at which the optical power drops to 1/e) and the Ge layer thickness, the optical power can be fully absorbed. However if the layer is sufficiently thin and/or the penetration depth larger than this thickness, a second Fresnel reflection/transmission must be considered at the bottom interface.
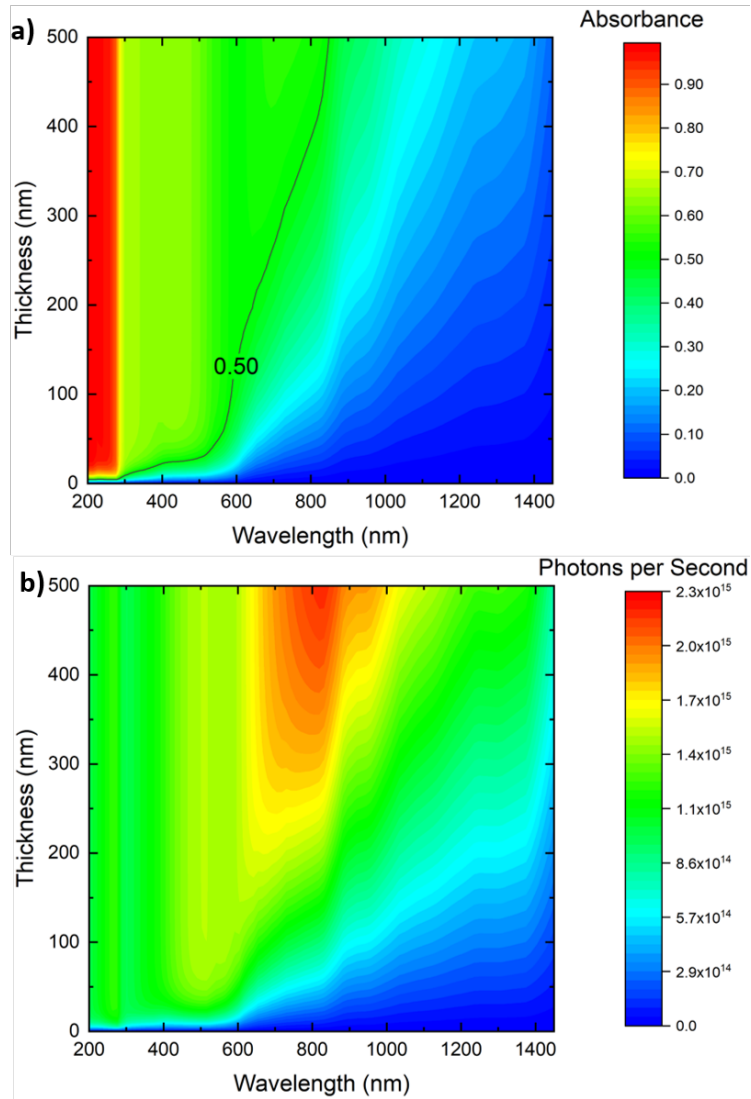
FIGURE A.2: (a) Colour map relating the ratio of absorbed optical power to the incident optical power as a function of Ge layer thickness and pump wavelength (b) Colour map relating the number of photons absorbed per second at 1 mW pump power as a function of Ge layer thickness and pump wavelength.

Figure A.2(a) illustrates this fact by plotting the ratio of the incident optical power and the actual optical power absorbed by the Ge layer. As the wavelength increases from the Ultra-Violet (UV) to Near Infra-Red (NIR) the amount of optical power reduces. Conversely, as the Ge layer thickness is decreased the amount amount of optical power absorbed relative to the incident power is reduced. Figure A.2(b) shows how many photons are absorbed at a constant pump power of 1 mW as a function of pump wavelength

and Ge layer thickness, this depends on the interplay between the reflectance/transmissions, the exponential decay and the thickness of the Ge. At a fixed power a larger number of photons per second is interacting with the sample at higher wavelengths as the individual photon energy is lower thus more are needed to achieve same power,however at higher wavelengths the penetration depth is also increased and more photons are lost. There is an optimum number of photons absorbed per second at around 600 nm - 900 nm pump wavelength and above 300 nm in Ge layer thickness. At longer wavelengths and for thinner Ge layers, most of the optical power will be reflected and/or pass straight through and thus cannot be used for optical pumping, higher incident powers will be required to achieve the same optical power within the Ge layer as found at lower wavelengths.

A.4   Thermal sensitivity of each stack

A 500 nm and 200 nm Ge layer thicknesses, were studied using Finite Element Modelling (FEM) at different pump wavelengths. The excitation laser beam diameter was fixed at 5 μm , the power was swept from 1 mW to 20 mW in 1 mW increments and the maximum temperature (at the origin). The gradient of these plots were calculated and given the term Thermal Sensitivity (TS), these values were plotted as a function of wavelength as shown in Figure A.3(a) for the Ge on Si stack and Figure A.3(b) for the GOI stack. The thermal sensitivity for all wavelengths is an order of magnitude higher for GOI stacks compared to the Ge on Si stacks, this is due to SiO_2 posessing an order of magnitude lower thermal conductivity than Si. Furthermore the thermal sensitivity is roughly half the value for 200 nm layer thickness compared to the 500 nm layer thickness for the GOI stack. However in the Ge on Si stack the TS is only 25% smaller. As the wavelength increases for both stacks and thicknesses, the TS drops.
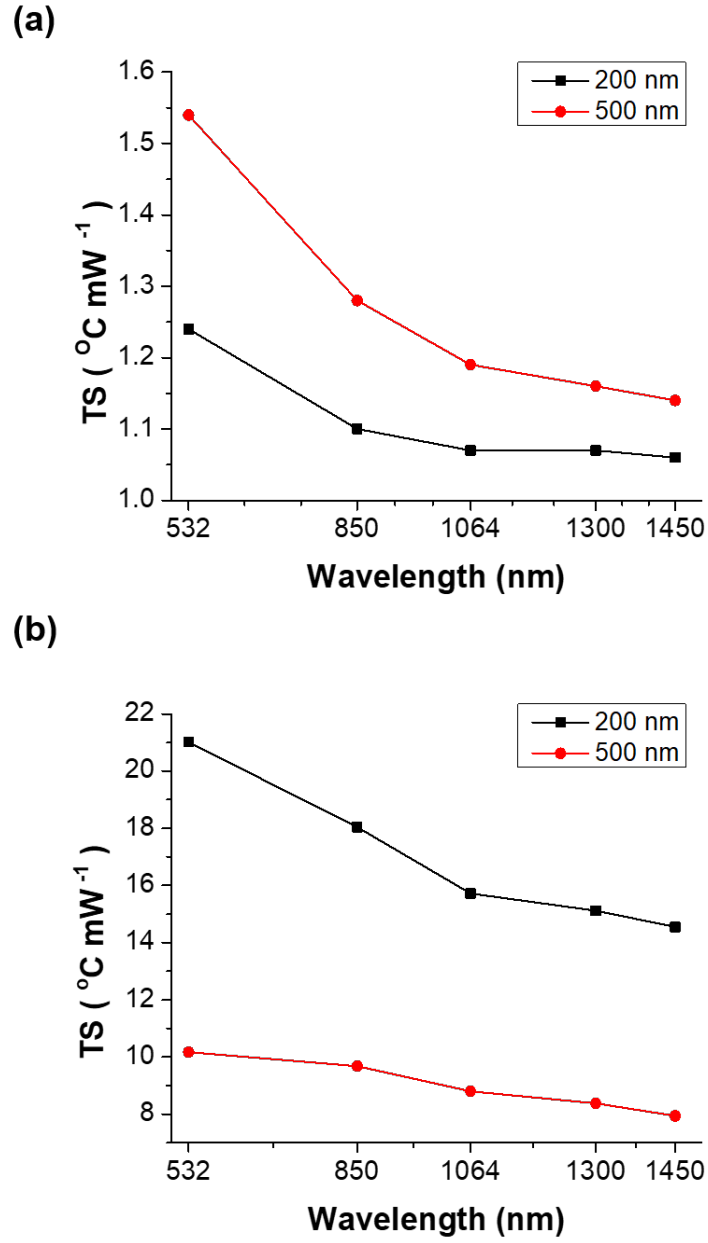
FIGURE A.3: Thermal sensitivity (TS) against pump wavelength (nm) at 200 nm and 500 nm layer thickness for (a) Ge on Si and (b) GOI.

Appendix B

Suspension and stiction in Ge on SOI

B.1   Critical length for suspension

In chapter 3, uniaxial and polyaxial bridges were fabricated on a Germanium (Ge) on Silicon-on-Insulator (SOI) platform. There is a critical length of the bridge, after which it will undergo stiction and not suspension. The critical length for suspension was calculated for uniaxial and polyaxial bridges as a function of the gap underneath the bridge using the method outlined in [105] and plotted in Figure A2. As the gap underneath increases the critical length increases. Furthermore the polyaxial bridges have smaller critical length values compared with the uniaxial bridges at equivalent gap underneath values.

B.2   Raman thermometry

Figure A2 shows the Raman thermometery for the same bridges in chapter 3 (In Figure 3.10) under identical experimental conditions. However the structures that underwent Hydro-Fluoric (HF) etching only and therefore adhered to the underlying Si are included. Figure B.2(a) shows the Raman shift as a function of power. Figure B.2(b) shows the temperature increase as a function of incident optical power. The structures that underwent HF etching and were adhered to the Si exhibit around 10x less heating compared to the bridges that underwent the TetraMethylAmmonium Hydroxide (TMAH) tuning and were suspended. Furthermore the different in temperature between uniaxial and polyaxial bridges is neglible for the HF etched bridges.
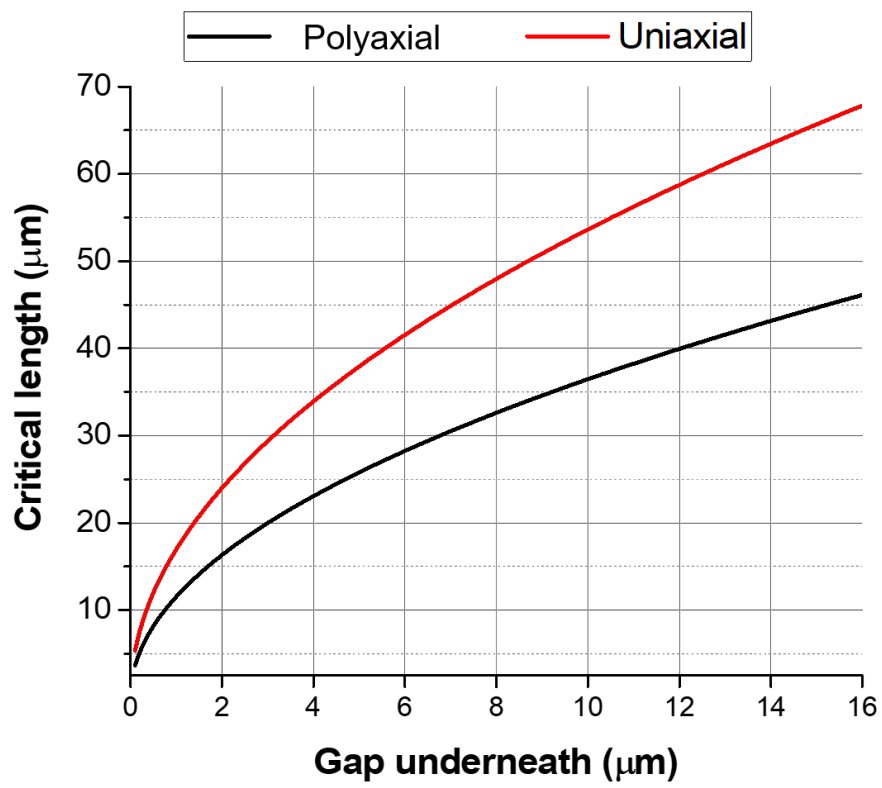
FIGURE B.1: Graph showing the influence of the gap underneath for the critical length
of suspension for polyaxial and uniaxial bridges.

(a)
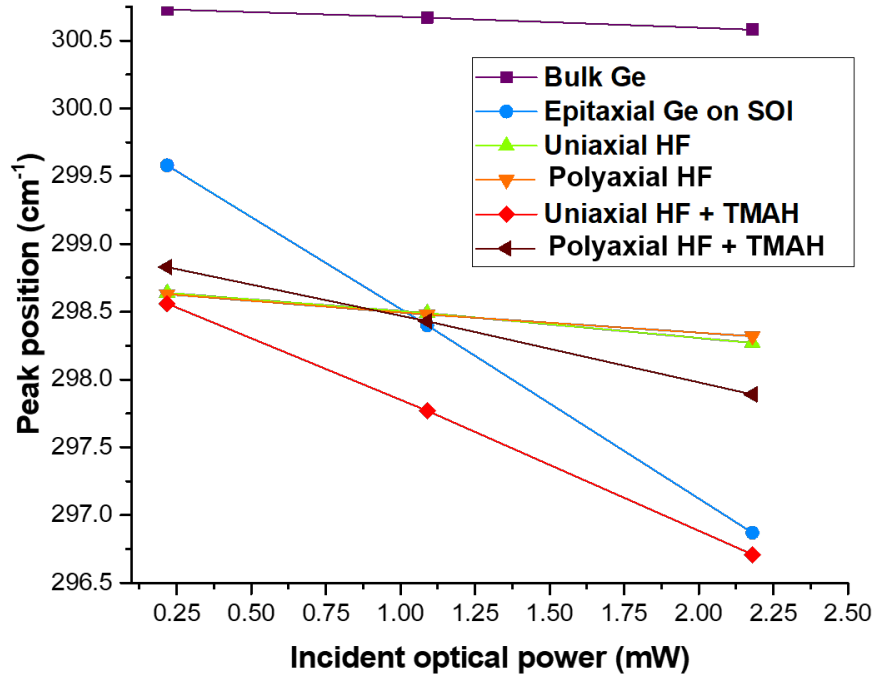
(b)
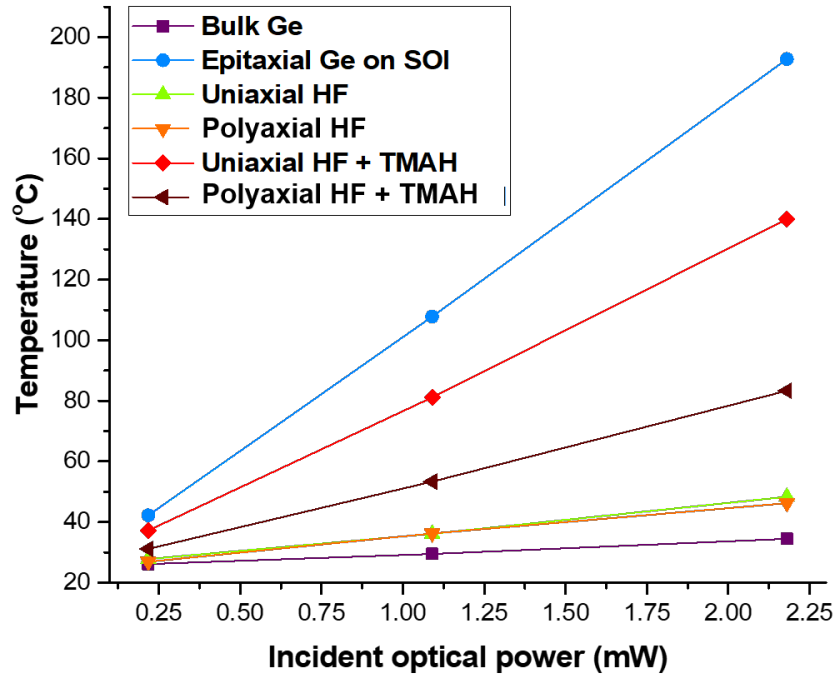
FIGURE B.2: (a) The relationship between incident pump power and the Raman shift for bulk Ge, epitaxial Ge on SOI and selected bridges.(b) The relationship between incident pump power and the temperature rise for bulk Ge, epitaxial Ge on SOI and selected bridges.

Appendix C

List of publications

1. **D. Burt**, A. Al-Attili, Z. Li, F. Y. Gardes, M. Sotto, N. Higashitarumizu,Y. Ishikawa, K. Oda, O. M. Querin, S. Saito, and R. W. Kelsall. Enhanced light emission from improved homogeneity in biaxially suspended germanium membranes from curvature optimization. Opt. Express, 25(19):22911–22922, Sep 2017. [1]

2. **D. Burt**, J. Gonzales, A. Al-Attili, H. Rutt, A. Z. Khokar, K. Oda, F. Gardes, and S. Saito. Comparison of uniaxial and polyaxial suspended germanium bridges in terms of mechanical stress and thermal management towards a CMOS compatible light source.Opt. Express, 27(26):37846–37858, Dec 2019. [2]

3. A. Z. Al-Attili, **D. Burt**, Z. Li, N. Higashitarumizu, F. Y. Gardes, K. Oda,Y. Ishikawa, and S. Saito. Germanium vertically light-emitting micro-gears generating orbital angular momentum.Opt. Express, 26(26):34675–34688, Dec 2018. [80]

Bibliography

[1] D. Burt, A. Al-Attili, Z. Li, F. Y. Gardès, M. Sotto, N. Higashitarumizu, Y. Ishikawa, K. Oda, O. M. Querin, S. Saito, and R. W. Kelsall. Enhanced light emission from improved homogeneity in biaxially suspended germanium membranes from curvature optimization. *Opt. Express*, 25(19):22911–22922, Sep 2017.

[2] D. Burt, J. Gonzales, A. Al-Attili, H. Rutt, A. Z. Khokar, K. Oda, F. Gardes, and S. Saito. Comparison of uniaxial and polyaxial suspended germanium bridges in terms of mechanical stress and thermal management towards a cmos compatible light source. *Opt. Express*, 27(26):37846–37858, Dec 2019.

[3] A. B. Garrett. The discovery of the transistor: W. Shockley, J. Bardeen, and W. Brattain. *Journal of Chemical Education*, 40(6):302, 1963.

[4] G. E. Moore. Cramming more components onto integrated circuits. *Electronics*, 38(8), April 1965.

[5] Intel 14 nm technology, howpublished = https://www.intel.co.uk/content/www/uk/en/silicon-innovations/intel-14nm-technology.html, Accessed: 2018-12-29.

[6] IBM 7nm. https://www.anandtech.com/show/13392/the-iphone-xs-xs-max-review-unveiling-the-silicon-secrets/2. Accessed: 2018-12-29.

[7] G. Q. Zhang and A. Roosmalen. *More Than Moore: Creating High Value Micro/-Nanoelectronics Systems*. Springer Publishing Company, Incorporated, 1st edition, 2009.

[8] F. Kreupl, A. P. Graham, G. S. Duesberg, W. Steinhögl, M. Liebau, E. Unger, and W. Hönlein. Carbon nanotubes in interconnect applications. *Microelectronic Engineering*, 64(1):399 – 408, 2002.

[9] D. A. B. Miller. Device requirements for optical interconnects to Silicon chips. *Proceedings of the IEEE*, 97(7):1166–1185, July 2009.

[10] Y. Chai. *Applied Photonics*. Elsevier, 1994.

[11] R. N. Hall, G. E. Fenner, J. D. Kingsley, T. J. Soltys, and R. O. Carlson. Coherent light emission from GaAs junctions. *Phys. Rev. Lett.*, 9:366–368, Nov 1962.

[12] R. J. Mears, L. Reekie, I. M. Jauncey, and D. N. Payne. High-gain rare-earth-doped fiber amplifier at 1.54 μm. In *Optical Fiber Communication*, page WI2. Optical Society of America, 1987.

[13] G. Roelkens, L. Liu, D. Liang, R. Jones, A. Fang, B. Koch, and J. Bowers. III-V/silicon photonics for on-chip and intra-chip optical interconnects. *Laser & Photonics Reviews*, 4(6):751–779, 2010.

[14] G. T. Reed. *Silicon Photonics: The State of the Art.* Wiley-Interscience, New York, NY, USA, 2008.

[15] R. Soref. The past, present, and future of silicon photonics. *IEEE Journal of Selected Topics in Quantum Electronics*, 12(6):1678–1687, Nov 2006.

[16] R. Soref. Silicon photonics: A review of recent literature. *Silicon*, 2(1):1–6, Jan 2010.

[17] S. Koehl, V. Krutu, and M. Paniccia. Continuous Silicon Laser. Technical report, Intel, 01 2005.

[18] Rockley photonics. https://https://www.rockleyphotonics.com/. Accessed: 2018-01-10.

[19] Intel. https://www.intel.co.uk/content/www/uk/en/architecture-and-technology/silicon-photonics/silicon-photonics-overview.html. Accessed: 2018-01-10.

[20] E. O. Kane. Energy band structure in p-type germanium and silicon. *Journal of Physics and Chemistry of Solids*, 1(1):82 – 99, 1956.

[21] L. Pavesi, S. Gaponenko, and L. D. Negro. *Towards the First Silicon Laser.* Springer Netherlands, 2003.

[22] Y. Suwa and S. Saito. Intrinsic optical gain of ultrathin silicon quantum wells from first-principles calculations. *Phys. Rev. B*, 79:233308, Jun 2009.

[23] S. Saito, Y. Suwa, H. Arimoto, N. Sakuma, D. Hisamoto, H. Uchiyama, J. Yamamoto, T. Sakamizu, T. Mine, S. Kimura, T. Sugawara, and M. Aoki. Stimulated emission of near-infrared radiation by current injection into silicon (100) quantum well. *Applied Physics Letters*, 95(24):241101, 2009.

[24] S. Saito, D. Hisamoto, H. Shimizu, H. Hamamura, R. Tsuchiya, Y. Matsui, T. Mine, T. Arai, N. Sugii, K. Torii, S. Kimura, and T. Onai. Silicon light-emitting transistor for on-chip optical interconnection. *Applied Physics Letters*, 89(16):163504, 2006.

[25] D. C. Wang, C. Zhang, P. Zeng, W. J. Zhou, L. Ma, H. T. Wang, Z. Q. Zhou, F. Hu, S. Y. Zhang, M. Lu, and X. Wu. An all-silicon laser based on silicon nanocrystals with high optical gains. *Science Bulletin*, 63(2):75 – 77, 2018.

[26] J. Liu, X. Sun, D. Pan, X. Wang, L. C. Kimerling, T. L. Koch, and J. Michel. Tensile-strained, n-type Ge as a gain medium for monolithic laser integration on Si. *Opt. Express*, 15(18):11272–11277, Sep 2007.

[27] J. Liu, X. Sun, L. C. Kimerling, and J. Michel. Direct-gap optical gain of Ge on Si at room temperature. *Opt. Lett.*, 34(11):1738–1740, Jun 2009.

[28] J. Liu, X. Sun, R. Camacho-Aguilera, L. C. Kimerling, and J. Michel. Ge-on-Si laser operating at room temperature. *Opt. Lett.*, 35(5):679–681, Mar 2010.

[29] R. E. Camacho-Aguilera, Y. Cai, N. Patel, J. T. Bessette, M. Romagnoli, C. Kimerling L, and J. Michel. An electrically pumped germanium laser. *Opt. Express*, 20(10):11316–11320, May 2012.

[30] S. Saito, F. Y. Gardes, A. Z. Al-Attili, K. Tani, K. Oda, Y. Suwa, T. Ido, Y. Ishikawa, S. Kako, S. Iwamoto, and Y. Arakawa. Group IV light sources to enable the convergence of photonics and electronics. *Frontiers in Materials*, 1:15, 2014.

[31] S. Saito, A. Z. Al-Attili, K. Oda, and Y. Ishikawa. Towards monolithic integration of germanium light sources on silicon chips. *Semiconductor Science and Technology*, 31(4):043002, March 2016.

[32] S. Bao, D. Kim, C. Onwukaeme, S. Gupta, K. C. Saraswat, K. H Lee, Y. Kim, D. Min, Y. Jung, H. Qiu, H. Wang, E. A. Fitzgerald, C. S. Tan, and D. Nam. Low-threshold optically pumped lasing in highly strained germanium nanowires. *Nature Communications*, 8(1):1845, 2017.

[33] F. T. Armand Pilon, A. Lyasota, Y.-M. Niquet, V. Reboud, V. Calvo, N. Pauc, J. Widiez, C. Bonzon, J. M. Hartmann, A. Chelnokov, J. Faist, and H. Sigg. Lasing in strained germanium microbridges. *Nature Communications*, 10(1):2724, 2019.

[34] D. S. Sukhdeo, D. Nam, J. Kang, M. L. Brongersma, and K. C. Saraswat. Bandgap-customizable germanium using lithographically determined biaxial tensile strain for silicon-compatible optoelectronics. *Opt. Express*, 23(13):16740–16749, Jun 2015.

[35] C. G. Van de Walle. Band lineups and deformation potentials in the model-solid theory. *Phys. Rev. B*, 39:1871–1883, Jan 1989.

[36] K. H. Lee, S. Bao, B. Wang, C. Wang, S. F. Yoon, J. Michel, E. A. Fitzgerald, and C. S. Tan. Reduction of threading dislocation density in Ge/Si using a heavily As-doped Ge seed layer. *AIP Advances*, 6(2):025028, 2016.

[37] Y. Ishikawa, K. Wada, D. Cannon, Jifeng Liu, H. C Luan, and L. C. Kimerling. Strain-induced band gap shrinkage in Ge grown on Si substrate. *Applied Physics Letters*, 82(13):2044–2046, 2003.

[38] X. Sun, J. Liu, L. C. Kimerling, and J. Michel. Direct gap photoluminescence of n-type tensile-strained Ge-on-Si. *Applied Physics Letters*, 95(1):011911, 2009.

[39] X. Sun, J. Liu, L. C. Kimerling, and J. Michel. Room-temperature direct bandgap electroluminesence from Ge-on-Si light-emitting diodes. *Opt. Lett.*, 34(8):1198–1200, Apr 2009.

[40] S. Chen, W. Li, J. Wu, Q. Jiang, M. Tang, S. Shutts, S. N. Elliott, A. Sobiesierski, A. J. Seeds, I. Ross, P.. Smowton, and H. Liu. Electrically pumped continuous-wave iii–v quantum dot lasers on silicon. *Nature Photonics*, 10(5):307–311, May 2016.

[41] R. Koerner, M. Oehme, M. Gollhofer, M. Schmid, K. Kostecki, S. Bechler, D. Widmann, E. Kasper, and J. Schulze. Electrically pumped lasing from Ge Fabry-Perot resonators on Si. *Opt. Express*, 23(11):14815–14822, Jun 2015.

[42] M. El Kurdi, G. Fishman, S. Sauvage, and P. Boucaud. Band structure and optical gain of tensile-strained germanium based on a 30 band kp formalism. *Journal of Applied Physics*, 107(1):013710, 2010.

[43] K. Sakata, B. Magyari-Köpe, S. Gupta, Y. Nishi, A. Blom, and P. Deák. The effects of uniaxial and biaxial strain on the electronic structure of germanium. *Computational Materials Science*, 112:263 – 268, 2016.

[44] D. S. Sukhdeo, S. Gupta, K. C. Saraswat, B. R. Dutt, and D. Nam. Ultimate limits of biaxial tensile strain and n-type doping for realizing an efficient low-threshold Ge laser. *Japanese Journal of Applied Physics*, 55(2):024301, 2016.

[45] S. Gupta, D. Nam, J. Vuckovic, and K. Saraswat. Room temperature lasing unraveled by a strong resonance between gain and parasitic absorption in uniaxially strained germanium. *Phys. Rev. B*, 97:155127, Apr 2018.

[46] K. Guilloy, N. Pauc, A. Gassenq, Y. M. Niquet, J. Escalante, I. Duchemin, S. Tardif, G. Osvaldo Dias, D. Rouchon, J. Widiez, J. M. Hartmann, R. Geiger, T. Zabel, H. Sigg, J. Faist, A. Chelnokov, V. Reboud, and V. Calvo. Germanium under high tensile stress: Nonlinear dependence of direct band gap vs strain. *ACS Photonics*, 3(10):1907–1911, 2016.

[47] J. M. Escalante. Non-linear behavior of germanium electronic band structure under high strain. *Computational Materials Science*, 152:223 – 227, 2018.

[48] S. Wirths, R. Geiger, N. von den Driesch, T. Mussler, G.and Stoica, S. Mantl, Z. Ikonic, M. Luysberg, S. Chiussi, J. M. Hartmann, H. Sigg, J. Faist, D. Buca,

and D. Grützmacher. Lasing in direct-bandgap GeSn alloy grown on Si. *Nature Photonics*, 9:88, Jan 2015.

[49] D. Stange, S. Wirths, R. Geiger, C. Schulte-Braucks, B. Marzban, N. Von den Driesch, G. Mussler, T. Zabel, T. Stoica, J. Hartmann, S. Mantl, Z. Ikonic, D. Grutzmacher, H. Sigg, J. Witzens, and D. Buca. Optically pumped GeSn microdisk lasers on Si. *ACS Photonics*, 3(7):1279–1285, 2016.

[50] V. Reboud, A. Gassenq, N. Pauc, J. Aubin, L. Milord, Q. M. Thai, M. Bertrand, K. Guilloy, D. Rouchon, J. Rothman, T. Zabel, F. Armand Pilon, H. Sigg, A. Chelnokov, J. M. Hartmann, and V. Calvo. Optically pumped GeSn micro-disks with 16% Sn lasing at 3.1 μm up to 180k. *Applied Physics Letters*, 111(9):092101, 2017.

[51] W. Dou, Y. Zhou, J. Margetis, S. A. Ghetmiri, S. Al-Kabi, W. Du, J. Liu, G. Sun, R. A. Soref, J. T., Baohua Li, M. Mortazavi, and S. Yu. Optically pumped lasing at 3 μm from compositionally graded GeSn with tin up to 22.3%. *Opt. Lett.*, 43(19):4558–4561, Oct 2018.

[52] Q. M. Thai, N. Pauc, J. Aubin, M. Bertrand, J. Chrétien, V. Delaye, A. Chelnokov, J. M. Hartmann, V. Reboud, and V. Calvo. GeSn heterostructure micro-disk laser operating at 230 k. *Opt. Express*, 26(25):32500–32508, Dec 2018.

[53] D. Sukhdeo, Y. Kim, S. Gupta, K. Saraswat, B. Dutt, and D. Nam. Theoretical modeling for the interaction of tin alloying with n-type doping and tensile strain for gesn lasers. *IEEE Electron Device Letters*, 37(10):1307–1310, 2016.

[54] A. Elbaz, D. Buca, N. von den Driesch, K. Pantzas, G. Patriarche, N. Zerounian, E. Herth, X. Checoury, S. Sauvage, I. Sagnes, A. Foti, R. Ossikovski, J.M. Hartmann, F. Boeuf, Z. Ikonic, P. Boucaud, D. Grützmacher, and M. El Kurdi. Ultra-low-threshold continuous-wave and pulsed lasing in tensile-strained gesn alloys. *Nature Photonics*, Mar 2020.

[55] J. Vanhellemont, E. Simoen, I. Romandic, and A. Theuwis. Chapter 2 - grown-in defects in germanium. In C. Claeys and E. Simoen, editors, *Germanium-Based Technologies*, pages 41 – 66. Elsevier, Oxford, 2007.

[56] D. Nam, J. Kang, M. L. Brongersma, and K. C. Saraswat. Observation of improved minority carrier lifetimes in high-quality Ge-on-insulator using time-resolved photoluminescence. *Opt. Lett.*, 39(21):6205–6208, Nov 2014.

[57] G. K. White and S. B. Woods. Thermal conductivity of Germanium and Silicon at low temperatures. *Phys. Rev.*, 103:569–571, Aug 1956.

[58] C. Lange, N. S. Köster, S. Chatterjee, H. Sigg, D. Chrastina, G. Isella, H. Von Känel, M. Schäfer, M. Kira, and S. W. Koch. Ultrafast nonlinear optical response of photoexcited Ge/SiGe quantum wells: Evidence for a femtosecond transient population inversion. *Physical Review B-Condensed Matter*, 79(20), 5 2009.

[59] R. E. Camacho-Aguilera, Y. Cai, J. T. Bessette, L. C. Kimerling, and J. Michel. High active carrier concentration in n-type, thin film Ge using delta-doping. *Opt. Mater. Express*, 2(11):1462–1469, Nov 2012.

[60] V. Reboud, J. Widiez, J. M. Hartmann, G. Osvaldo Dias, D. Fowler, A. Chelnokov, A. Gassenq, K. Guilloy, N. Pauc, V. Calvo, R. Geiger, T. Zabel, J. Faist, and H. Sigg. Structural and optical properties of 200 mm germanium-on-insulator (GeOI) substrates for silicon photonics applications. volume 9367, pages 231 – 236, 2015.

[61] M. Nishimura, Y. Tsusaka, J. Matsui, and Y. Ishikawa. Enhanced tensile strain in Ge epitaxial layers grown on Si-on-quartz wafers. *2018 IEEE 15th International Conference on Group IV Photonics (GFP)*, pages 1–2, 2018.

[62] C. Ortolland, Y. Okuno, P. Verheyen, C. Kerner, C. Stapelmann, M. Aoulaiche, N. Horiguchi, and T. Hoffmann. Stress memorization technique—fundamental understanding and low-cost integration for advanced CMOS technology using a nonselective process. *IEEE Transactions on Electron Devices*, 56(8):1690–1697, Aug 2009.

[63] F. Ootsuka, S. Wakahara, K. Ichinose, A. Honzawa, S. Wada, H. Sato, T. Ando, H. Ohta, K. Watanabe, and T. Onai. A highly dense, high-performance 130 nm node CMOS technology for large scale system-on-a-chip applications. In *International Electron Devices Meeting 2000. Technical Digest. IEDM (Cat. No.00CH37138)*, pages 575–578, Dec 2000.

[64] E. Parton and P. Verheyen. Strained silicon — the key to sub-45 nm CMOS. *III-Vs Review*, 19(3):28 – 31, 2006.

[65] A. Ghrib, M. de Kersauson, M. El Kurdi, R. Jakomin, G. Beaudoin, S. Sauvage, G. Fishman, G. Ndong, M. Chaigneau, R. Ossikovski, I. Sagnes, and P. Boucaud. Control of tensile strain in germanium waveguides through silicon nitride layers. *Applied Physics Letters*, 100(20):201104, 2012.

[66] A. Ghrib, M. El Kurdi, M. de Kersauson, M. Prost, S. Sauvage, X. Checoury, G. Beaudoin, I. Sagnes, and P. Boucaud. Tensile-strained germanium microdisks. *Applied Physics Letters*, 102(22):221112, 2013.

[67] A. Ghrib, M. El Kurdi, M. Prost, M. de Kersauson, L. Largeau, O. Mauguin, G. Beaudoin, S. Sauvage, X. Checoury, G. Ndong, M. Chaigneau, R. Ossikovski, S. David, I. Sagnes, and P. Boucaud. Strain engineering in germanium microdisks. volume 8990, 2014.

[68] G. Capellini, G. Kozlowski, Y. Yamamoto, M. Lisker, C. Wenger, G. Niu, P. Zaumseil, B. Tillack, A. Ghrib, M. de Kersauson, M. El Kurdi, P. Boucaud,

and T. Schroeder. Strain analysis in sin/ge microstructures obtained via si-complementary metal oxide semiconductor compatible approach. *Journal of Applied Physics*, 113(1):013513, 2013.

[69] G. Capellini, C. Reich, S. Guha, Y. Yamamoto, M. Lisker, M. Virgilio, A. Ghrib, M. El Kurdi, P. Boucaud, B. Tillack, and T. Schroeder. Tensile Ge microstructures for lasing fabricated by means of a silicon complementary metal-oxide-semiconductor process. *Opt. Express*, 22(1):399–410, Jan 2014.

[70] M. El Kurdi, A. Ghrib, M. de Kersauson, M. Prost, S. Sauvage, X. Checoury, G. Beaudoin, I. Sagnes, G. Ndong, M. Chaigneau, R. Ossikovski, and P. Boucaud. Tensile-strained germanium microdisks using si3n4 stressors. In *10th International Conference on Group IV Photonics*, pages 95–96, Aug 2013.

[71] K. Tani, K. Oda, J. Kasai, T. Okumura, T. Mine, S. Saito, and T. Ido. Germanium waveguides on lateral silicon-on-insulator diodes for monolithic light emitters and photo detectors. In *10th International Conference on Group IV Photonics*, pages 134–135, Aug 2013.

[72] K. Tani, K. Oda, T. Okumura, T. Takezaki, J. Kasai, T. Mine, and T. Ido. Enhanced electroluminescence from Germanium waveguides by local tensile strain with Silicon Nitride stressors. 2013.

[73] M. El Kurdi, M. Prost, A. Ghrib, S. Sauvage, X. Checoury, G. Beaudoin, I. Sagnes, G. Picardi, R. Ossikovski, and P. Boucaud. Direct band gap Germanium microdisks obtained with Silicon Nitride stressor layers. *ACS Photonics*, 3(3):443–448, 2016.

[74] P. Velha, K. Gallacher, D. Dumas, D. J. Paul, M. Myronov, and D. R. Leadley. Tuning the electroluminescence of n-Ge LEDs using process induced strain. In *The 9th International Conference on Group IV Photonics (GFP)*, pages 337–339, Aug 2012.

[75] P. Velha, D. C. Dumas, K. Gallacher, R. Millar, M. Myronov, D. R. Leadley, and D. J. Paul. Strained germanium nanostructures on silicon emitting at > 2.2 μm wavelength. In *10th International Conference on Group IV Photonics*, pages 142–143, Aug 2013.

[76] R.W. Millar, K. Gallacher, A. Samarelli, J. Frigerio, D. Chrastina, G. Isella, T. Dieing, and D.J. Paul. Extending the emission wavelength of Ge nanopillars to 2.25 μm using silicon nitride stressors. *Opt. Express*, 23(14):18193–18202, Jul 2015.

[77] R.W. Millar, K. Gallacher, J. Frigerio, A. Ballabio, A. Bashir, I. MacLaren, G. Isella, and D. J. Paul. Analysis of Ge micro-cavities with in-plane tensile strains above 2 %. *Opt. Express*, 24(5):4365–4374, Mar 2016.

[78] A. Ghrib, M. El Kurdi, M. Prost, S. Sauvage, X. Checoury, G. Beaudoin, M. Chaigneau, R. Ossikovski, I. Sagnes, and P. Boucaud. All-around SiN stressor for high and homogeneous tensile strain in Germanium microdisk cavities. *Advanced Optical Materials*, 3(3):353–358, 2015.

[79] A. Elbaz, M. El Kurdi, A. Aassime, S. Sauvage, X. Checoury, I. Sagnes, F. Bœuf, and P. Boucaud. Solving thermal issues in tensile-strained Ge microdisks. *Opt. Express*, 26(22):28376–28384, Oct 2018.

[80] A. Z. Al-Attili, D. Burt, Z. Li, N. Higashitarumizu, F. Y. Gardes, K. Oda, Y. Ishikawa, and S. Saito. Germanium vertically light-emitting micro-gears generating orbital angular momentum. *Opt. Express*, 26(26):34675–34688, Dec 2018.

[81] P. Lim, S. Park, Y. Ishikawa, and K. Wada. Enhanced direct bandgap emission in germanium by micromechanical strain engineering. *Opt. Express*, 17(18):16358–16365, Aug 2009.

[82] C. Boztug, J. R. Sánchez-Pérez, F. F. Sudradjat, RB Jacobson, D. M. Paskiewicz, M. G. Lagally, and R. Paiella. Tensilely strained Germanium nanomembranes as infrared optical gain media. *Small*, 9(4):622–630, 2013.

[83] A. Ayan, D. Turkay, B. Unlu, P. Naghinazhadahmadi, S/ N. B. Oliaei, C. Boztug, and S. Yerci. Strain engineering of Germanium nanobeams by electrostatic actuation. *Scientific Reports*, 9(1):4963, 2019.

[84] J. R. Jain, A. Hryciw, T. M. Baer, D. A. B. Miller, M. L. Brongersma, and R. T. Howe. A micromachining-based technology for enhancing germanium light emission via tensile strain. *Nature Photonics*, 6(6):398–405, 2012.

[85] A. Z. Al-Attili, S. Kako, M. K. Husain, F. Y. Gardes, S. Iwamoto, Y. Arakawa, and S. Saito. Tensile strain engineering of germanium micro-disks on free-standing SiO$_2$ beams. *Japanese Journal of Applied Physics*, 55(4S):04EH02, mar 2016.

[86] A. Z. Al-Attili, S. Kako, M. K. Husain, F. Y. Gardes, N. Higashitarumizu, S. Iwamoto, Y. Arakawa, Y. Ishikawa, H. Arimoto, K. Oda, T. Ido, and S. Saito. Whispering gallery mode resonances from Ge micro-disks on suspended beams. *Frontiers in Materials*, 2:43, 2015.

[87] R. A. Minamisawa, M. J. Süess, R. Spolenak, J. Faist, C. David, J. Gobrecht, K. K. Bourdelle, and H. Sigg. Top-down fabricated silicon nanowires under tensile elastic strain up to 4.5%. *Nature Communications*, 3(1):1096, 2012.

[88] M. J. Süess, R. Geiger, R. A. Minamisawa, G. Schiefler, J. Frigerio, D. Chrastina, G. Isella, R. Spolenak, J. Faist, and H. Sigg. Analysis of enhanced light emission from highly strained germanium microbridges. *Nature Photonics*, 7:466 EP, Apr 2013.

[89] D. S. Sukhdeo, D. Nam, J. Kang, M. L. Brongersma, and K. C. Saraswat. Direct bandgap germanium-on-silicon inferred from 5.7% uniaxial tensile strain. *Photon. Res.*, 2(3):A8–A13, Jun 2014.

[90] V. Reboud, A. Gassenq, K. Guilloy, G. Osvaldo Dias, J. M. Escalante, S. Tardif, N. Pauc, J. M. Hartmann, J. Widiez, E. Gomez, E. Bellet Amalric, D. Fowler, D. Rouchon, I. Duchemin, Y. M. Niquet, F. Rieutord, J. Faist, R. Geiger, T. Zabel, E. Marin, H. Sigg, A. Chelnokov, and V. Calvo. Ultra-high amplified strain on 200 mm optical Germanium-On-Insulator (GeOI) substrates: towards CMOS compatible Ge lasers. volume 9752, 2017.

[91] A. Gassenq, S. Tardif, K. Guilloy, I. Duchemin, N. Pauc, J. M. Hartmann, D. Rouchon, J. Widiez, Y. M. Niquet, L. Milord, T. Zabel, H. Sigg, J. Faist, A. Chelnokov, F. Rieutord, V. Reboud, and V. Calvo. Raman-strain relations in highly strained Ge: Uniaxial 100, 110 and biaxial 001 stress. *Journal of Applied Physics*, 121(5):055702, 2017.

[92] A. Gassenq, S. Tardif, K. Guilloy, G. Osvaldo Dias, N. Pauc, I. Duchemin, D. Rouchon, J.-M. Hartmann, J. Widiez, J. Escalante, Y.-M. Niquet, R. Geiger, T. Zabel, H. Sigg, J. Faist, A. Chelnokov, F. Rieutord, V. Reboud, and V. Calvo. Accurate strain measurements in highly strained Ge microbridges. *Applied Physics Letters*, 108(24):241902, 2016.

[93] D. Nam, D. S. Sukhdeo, J. Kang, J. Petykiewicz, J. H. Lee, W. S. Jung, J Vučković, M. L. Brongersma, and K. C. Saraswat. Strain-induced pseudoheterostructure nanowires confining carriers at room temperature with nanoscale-tunable band profiles. *Nano Letters*, 13(7):3118–3123, 2013. PMID: 23758608.

[94] J. Petykiewicz, D. Nam, D. S. Sukhdeo, S. Gupta, S. Buckley, A. Y. Piggott, J. Vučković, and K. C. Saraswat. Direct bandgap light emission from strained germanium nanowires coupled with high-Q nanophotonic cavities. *Nano Letters*, 16(4):2168–2173, 2016. PMID: 26907359.

[95] T. Zabel, R. Geiger, E. Marin, E. Müller, A. Diaz, C. Bonzon, M. J. Süess, R. Spolenak, J. Faist, and H. Sigg. Top-down method to introduce ultra-high elastic strain. 32(4):726–736, 2017.

[96] J. Jiang, M. Xue, C. Lu, C. S. Fenrich, M. Morea, K. Zang, J. Gao, M. Cheng, Y. Zhang, T. I. Kamins, J. S. Harris, and J. Sun. Strain-induced enhancement of electroluminescence from highly strained Germanium light-emitting diodes. *ACS Photonics*, 6(4):915–923, 2019.

[97] Y. Kim, Jan. Petykiewicz, S. Gupta, J. Vuckovic, K. C. Saraswat, and Nam D. Strained Ge light emitter with Ge on dual insulators for improved thermal conduction and optical insulation. *IEIE Transactions on Smart Processing and Computing*, 4(5):318–323, 10 2015.

[98] M. Süess. *Highly strained Si and Ge micro and nano bridges for micro- and optoelectronic applications*. PhD thesis, EHT Zurich, 2014.

[99] D. S. Sukhdeo, J. Petykiewicz, S. Gupta, D. Kim, S. Woo, Y. Kim, J. Vučković, K. C. Saraswat, and D. Nam. Ge microdisk with lithographically-tunable strain using CMOS-compatible process. *Opt. Express*, 23(26):33249–33254, Dec 2015.

[100] A. Gassenq, K. Guilloy, G. Osvaldo Dias, N. Pauc, D. Rouchon, J.-M. Hartmann, J. Widiez, S. Tardif, F. Rieutord, J. Escalante, I. Duchemin, Y.-M. Niquet, R. Geiger, T. Zabel, H. Sigg, J. Faist, A. Chelnokov, V. Reboud, and V. Calvo. 1.9% bi-axial tensile strain in thick germanium suspended membranes fabricated in optical germanium-on-insulator substrates for laser applications. *Applied Physics Letters*, 107(19):191904, 2015.

[101] S. Ishida, S. Kako, K. Oda, T. Ido, S. Iwamoto, and Y. Arakawa. Suspended germanium cross-shaped microstructures for enhancing biaxial tensile strain. *Japanese Journal of Applied Physics*, 55(4S):04EH14, mar 2016.

[102] A. Elbaz, M. El Kurdi, A. Aassime, S. Sauvage, X. Checoury, I. Sagnes, C. Baudot, F. Boeuf, and P. Boucaud. Germanium microlasers on metallic pedestals. *APL Photonics*, 3(10):106102, 2018.

[103] Von mises stress. https://www.continuummechanics.org/vonmisesstress.html/. Accessed: 2020-05-18.

[104] A. Gassenq, K. Guilloy, N. Pauc, J.-M. Hartmann, G. Osvaldo Dias, D. Rouchon, S. Tardif, J. Escalante, I. Duchemin, Y.-M. Niquet, A. Chelnokov, V. Reboud, and Vincent Calvo. Study of the light emission in Ge layers and strained membranes on Si substrates. *Thin Solid Films*, 613:64 – 67, 2016. Spring EMRS symposium: Transport and photonics in group IV-based nano-devices.

[105] N. Tas, T. Sonnenberg, H.Jansen, R. Legtenberg, and M. Elwenspoek. Stiction in surface micromachining. *Journal of micromechanics and microengineering*, 6(4):385–397, 12 1996.

[106] J. Jaramillo-Fernandez, E. Chavez-Angel, and C. M. Sotomayor-Torres. Raman thermometry analysis: Modelling assumptions revisited. *Applied Thermal Engineering*, 130:1175 – 1181, 2018.

[107] W.D Pilkley and D.F Pilkley. *Stress Concentration Analysis and Design*, chapter 6, pages 457–512. John Wiley Sons, Ltd, 2008.

[108] D. Rainko, Z. Ikonic, A. Elbaz, Nils. Von Den D., D. Stange, E. Herth, P. Boucaud, M. El Kurdi, D. Grützmacher, and D. Buca. Impact of tensile strain on low Sn content GeSn lasing. *Scientific Reports*, 9(1):1–9, January 2019.

[109] J. Chrétien, N. Pauc, F. Armand Pilon, M. Bertrand, Q. Thai, L. Casiez, N. Bernier, H. Dansas, P. Gergaud, E. Delamadeleine, R. Khazaka, H. Sigg, J. Faist, A. Chelnokov, V. Reboud, J. Hartmann, and Vincent Calvo. GeSn lasers covering a wide wavelength range thanks to uniaxial tensile strain. *ACS Photonics*, 6(10):2462–2469, Oct 2019.

[110] M. A. Green. Self-consistent optical parameters of intrinsic silicon at 300k including temperature coefficients. *Solar Energy Materials and Solar Cells*, 92(11):1305 – 1310, 2008.